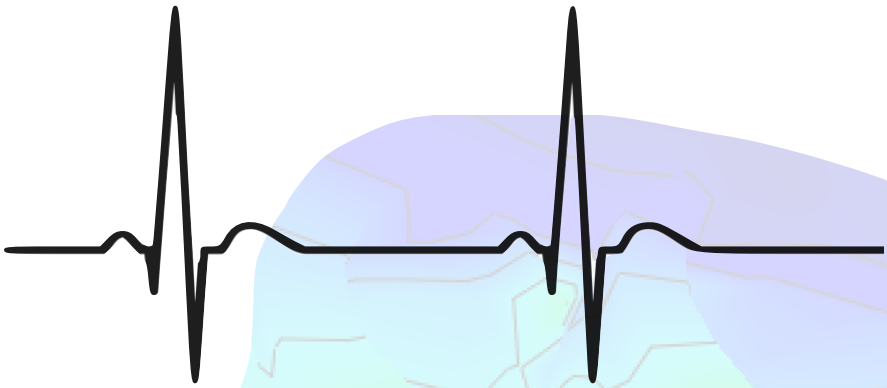

BIOELECTRICAL SIGNAL PROCESSING IN CARDIOLOGY

INVERSE SOLUTION MAPPING ON EPICARDIAL AND ENDOCARDIAL POTENTIALS

Àngels Ratés i Borràs

BACHELOR THESIS

Degree in *Audio-visual Systems* ENGINEERING

Escola Tècnica d'Enginyeria de Telecomunicació de Barcelona

Universitat Politècnica de Catalunya

And

Northeastern University

Advisor: Dr. Dana Brooks

Co-Advisor: Mr. Jaume Coll Font

Boston, July 2015

Abstract

Inverse electrocardiography is aimed at reconstructing the heart electrical activity and its corresponding spread throughout the heart from non-invasive body surface measurements obtained through the Electrocardiogram (ECG) technique. This field has showed increasing promise during the last decades due to its main application: predict possible cardiac diseases such that medical interventions are avoided and costs which were meant to these clinical operations are also reduced. Still, properly detection of these cardiac diseases is directly correlated with the performance of the inverse-solving regularization methods.

This Final Project counts with the collaboration of the Department of Medicine and the Department of Mathematics and Statistics of the Dalhousie University, Canada, which provided us with subject-specific BSPM measurements and data extracted from CT-scans of catheter interventions. Hence, our principals goals would be the analysis, review, comparison and cross-validation of the computed results on the multiple variants of the automated inverse-solving algorithms. Accordingly, a final conclusion of the influence which every regularization method has on the inverse solutions would be conducted by means of specialized simulation programs and numerical error measures.

Resum

La Electrocardiografía Inversa consisteix en la reconstrucció de l'activitat elèctrica del cor i la seva corresponent propagació al llarg del cor a partir de mesuraments no invasius presos en la superfície del cos i obtinguts a través de la tècnica anomenada l'Electrocardiograma (ECG). Aquest camp ha mostrat una creixent promesa durant les últimes dècades gràcies a la seva aplicació principal: predir possibles malalties cardíaques i així evitar intervencions cirúrgiques i reduïr els costos que estaven destinats a aquestes. No obstant això, la correcta detecció d'aquestes malalties cardíaques està directament relacionada amb el funcionament dels mètodes de regularització que solucionen el problema invers.

Aquest Projecte Final compta amb la col·laboració del Departament de Medicina i el Departament de Matemàtiques i Estadística de la Universitat de Dalhousie, Canadà, la qual ens ha proporcionat mesuraments de BSPM d'un subjecte específic i dades extretes de escàners CT de intervencions amb catèter. Així doncs, els nostres objectius fonamentals seran l'anàlisi, la revisió, la comparació i la validació creuada dels resultats en base a les múltiples variants dels algoritmes automatitzats per resoldre el problema invers. Conseqüentment, es durà a terme una conclusió final de la influència que cada un dels mètodes de regularització té sobre les solucions inverses per mitjà de programes especialitzats en simulació i mesures d'error numèriques.

Resumen

La Electrocardiografía Inversa consiste en la reconstrucción de la actividad eléctrica del corazón y su correspondiente propagación en el corazón a partir de medidas no invasivas tomadas en la superficie corporal y obtenidas a través de la técnica llamada el Electrocardiograma (ECG). Este campo ha mostrado una creciente promesa durante las últimas décadas debido a su aplicación principal: predecir posibles enfermedades cardíacas y así evitar intervenciones quirúrgicas y reducir los costes que estaban destinados a éstas. Sin embargo, la correcta detección de estas enfermedades cardíacas está directamente relacionada con el funcionamiento de los métodos de regularización que solucionan el problema inverso.

Este Proyecto Final cuenta con la colaboración del Departamento de Medicina y el Departamento de Matemáticas y Estadística de la Universidad de Dalhousie, Canadá, que nos ha proporcionado medidas de BSPM de un sujeto específico y datos extraídos de escáneres CT de intervenciones con catéter. Por lo tanto, nuestros objetivos fundamentales serán el análisis, la revisión, la comparación y la validación cruzada de los resultados en base a las múltiples variantes de los algoritmos automatizados para resolver el problema inverso. Consecuentemente, se llevará a cabo una conclusión final de la influencia que cada uno de los métodos de regularización tiene sobre las soluciones inversas mediante programas especializados en simulación y medidas de error numéricas.

Al meu tiet Jordi,
per fer crèixer en mi una petita investigadora
i no deixar de recolzar-me mai.

Acknowledgements

First of all, I would like to thank my advisor Dana for his incredible support throughout this intense adventure and his confidence towards me no mattering what I knew when I first arrived.

Secondly, thank my co-advisor Jaume Coll, for teaching me with an infinite patience and enlightening me with so many concepts which I could never have understood on my own. Also, thank my box-neighbor Biel Roig for joining our discussions and debates even though not having to.

It is worth mentioning the great opportunity that I had to conduct this project in collaboration with the Dalhousie University, and how enriching has been to be part of the SimEst meetings, each of which has helped me growing professionally.

I would also like to express my gratitude to everyone with who I have been lucky to share this experience but specially thank my old friends from el Baix Camp, who kept by my side despite the distance.

Last and most important, I would really like to thank my family for their inconditional support and for making my dreams come true through their effort and work.

Revision history and approval record

Revision	Date	Purpose
0	16/06/2015	Document creation
1	16/07/2015	Document revision

DOCUMENT DISTRIBUTION LIST

Name	e-mail
Àngels Ratés i Borràs	angelsrates@gmail.com
Jaume Coll Font	jcollfont@gmail.com
Dana Brooks	brooks@ece.neu.edu
Lluís Torres	luis.torres@upc.edu

Written by:		Reviewed and approved by:	
Date	16/07/2015	Date	16/07/2015
Name	Àngels Ratés i Borràs	Name	Dana Brooks
Position	Project Author	Position	Project Supervisor

Table of Contents

List of Figures

List of Tables:

1. Introduction

Bioelectrical signal processing applied to cardiology consists on reconstructing the heart electrical activity from non-invasive body surface measurements. Its related methods have applicability on medicine although ill-conditioned physiology represents a technical challenge and limitation on their performance.

The main application of reconstructing this heart electrical activity is anticipating possible heart abnormalities or heart diseases such as arrhythmia or ischemia before they could be dramatically developed. Its profits are either health-caring and financial considering that clinical interventions are avoided and costs which were meant to these clinical operations are also reduced.

To be capable of conducting a proper bioelectrical signal processing of the heart, the heart's physiology and its normal behavior will be introduced.

1.1. The heart's anatomy and its electrical activity

The heart is a muscular organ about the size of a closed fist that functions as the body's circulatory pump. It takes in deoxygenated blood through the veins and delivers it to the lungs for oxygenation before pumping it into the various arteries - which provide oxygen and nutrients to body tissues by transporting the blood throughout the body [1].

Its anatomy is divided into two mirrored sides, left and right, each of which consists on two chambers: the atrium where the blood enters and the ventricle where the blood is forced into further circulation to the upper body.

Both of these sides are separated by a muscular wall called septum. Blood flow's direction is monitored by four valves placed between the atria and the ventricles - atrioventricular valves - and between the ventricles and the arteries - pulmonary and aortic valves.

The heart wall is made of 3 layers: epicardium, endocardium and myocardium.

- The **epicardium** is the outermost layer of the heart wall and helps to lubricate and protect the outside of the heart.
- The **endocardium** is the simple squamous endothelium layer that lines the inside of the heart. The endocardium is very smooth and is responsible for keeping blood from sticking to the inside of the heart and forming potentially deadly blood clots.
- The **myocardium** is the muscular middle layer of the heart wall that contains the cardiac muscle tissue which produce mechanical force during contraction of the heart. It also incorporates muscle cells, also called pacemaker cells concentrated primarily in the sinoatrial node and the atrioventricular node, which are connected to conduction fibers that allows an electrical impulse to spread rapidly throughout the heart.

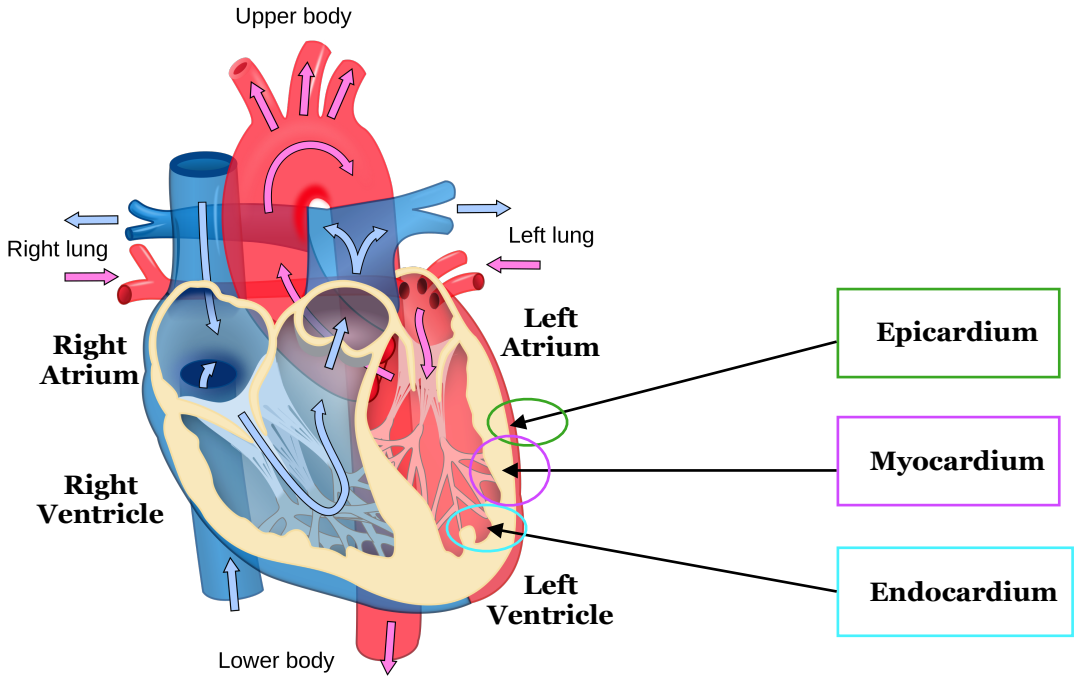

Figure 1.1.1. Basic anatomy of the heart and the pathway that follows the blood oxygenation flow [2].

This electrical impulse is due to a special group of cells that has the property of excitability, which arise as a ionic process of electrochemical activity. These cells are bounded with a plasma membrane which possesses permeability properties that allow certain substances to pass from the inside of a cell to the outside through different channels. If these substances are fluids, they become electrically conductive since they contain several types of ions - such as potassium, sodium and calcium.

In resting conditions, a cell is negatively charged due to its concentration of negatively charged ions within and its membrane's permeability, which leads to a negative transmembrane potential, assuming the cell's outside to be null.

This transmembrane potential arise when the membrane's channels open and a ion diffusion takes place, leading to a positive electrical charge outside the cell. As the transmembrane potential increases, the movement of ions across the membrane does also so, provoking a concentration force. This ions movement terminates when the concentration force balances the electrical force, and so then the corresponding transmembrane potential is called the equilibrium potential.

On the process of the transmembrane potential increase, a signal called **action potential** is generated if the potential exceeds a certain threshold, which would result as the excitation of the cell. This action potential is identical per every cell and behaves non-linearly - independently from the actual cell current - the all-or-nothing principle.

The action potential goes through three different phases: **rapid depolarization**, when the transmembrane potential passes a certain threshold potential, the cell becomes excited and consequently an action potential appears, **depolarization**, when the transmembrane potential decreases from positive electrical charge and consequently the charge inside the cell becomes progressively less negative, and **repolarization**, when the transmembrane potential recovers to its resting potential and as a result the charge within the cell turns out to very negative.

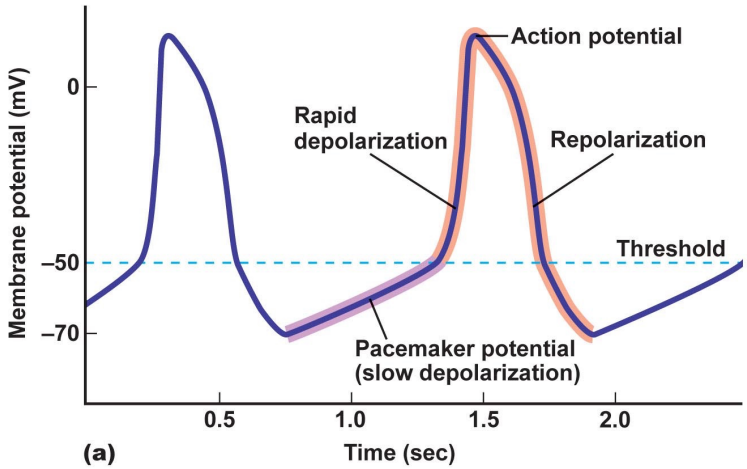

Figure 1.1.2. The phases of the transmembrane electrical potential in a cardiac cycle [3].

The action potential is initiated in the SA node and travels by way of conduction fibers to the atrial muscle where it spreads throughout the cells of the atria and ends up in the AV node. Then, there is a momentary delay due to slower conduction within these cells more than in other cells of the conduction system [3].

Once the impulse leaves the AV node, its direction is the atrioventricular bundle (bundle of His) in the interventricular septum. It only takes a short distance to travel through the atrioventricular bundles - to the apex of the heart.

There, it splits rapidly into the right and left bundle branches, spreading at the same moment upward through the ventricular muscle and finally getting into the myocardial cells by means of the extensive conduction fibers called Purkinje fibers.

This final step is the trigger for the ventricular muscle contraction and consequently provoke a mechanical response and the heart to beat the blood towards the upper body.

The process of this electrical impulse spreading throughout the heart is called a **cardiac cycle**.

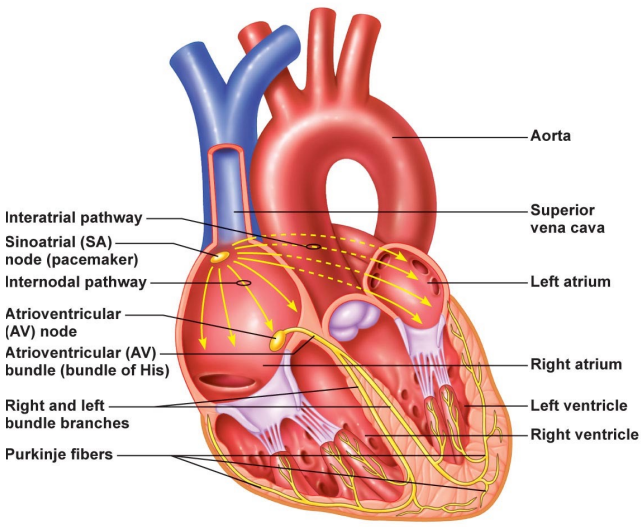

Figure 1.1.3. Initiation and conduction of an electrical impulse during a heartbeat [3].

1.2. The Electrocardiogram

The electrical activity of the heart can be characterized by measurements acquired from the cellular level as well as from the body surface. The electrocardiogram describe the different electrical of a cardiac cycle and represents a summation in time and space of the generated action potentials by millions of muscle cells from measurements on the body surface by attaching a set of electrodes to the skin.

These electrodes are positioned so that the spatiotemporal variations during the cardiac electrical cycle could be well-reflected.

During an ECG recording, the voltage difference between two electrodes is called a lead, which can be unipolar - it reflects the voltage variation of a single electrode and it is measured in function of a reference electrode, positioned so that the voltage remains almost constant during the entire cardiac cycle - or bipolar - it reflects the voltage difference between two electrodes placed on different positions.

The most common standardized electrode positions are: standard 12-lead ECG, orthogonal leads and synthesized leads.

The electrode wires are connected to a differential amplifier with high gain and large dynamic range because the ECG magnitude varies from a few microvolts to about 1V and also although that the electrical waves have a maximum value of few millivolts, the electrode-skin variations in impedance may reach 1V.

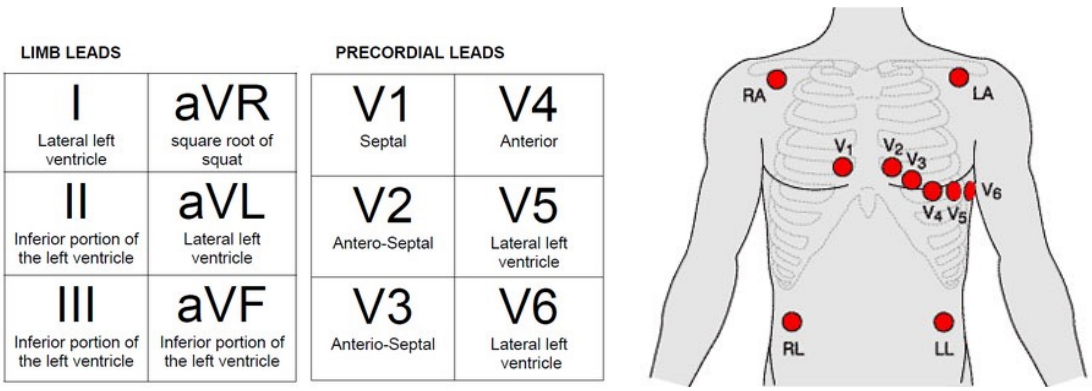

Figure 1.2. Standard 12-Lead ECG placement [4].

1.2.1. Depolarization and repolarization

Both depolarization and repolarization phases can be identified on an ECG signal. In the following item the ECG would be broken down into any meaningful variation related to the corresponding heart electrical activation change.

In overall, atrial depolarization is reflected by the P wave - for instance, a poor or absent P wave would mean that the heart rhythm origins in the ventricles - ventricular depolarization is reflected by the QRS complex, whereas the T wave reflects the ventricular repolarization. The ST segment corresponds to the time interval during which the ventricles remain activated, depolarized. RR interval represents an entire ventricular cardiac cycle and it corresponds to the time interval between two consecutive R waves [5].

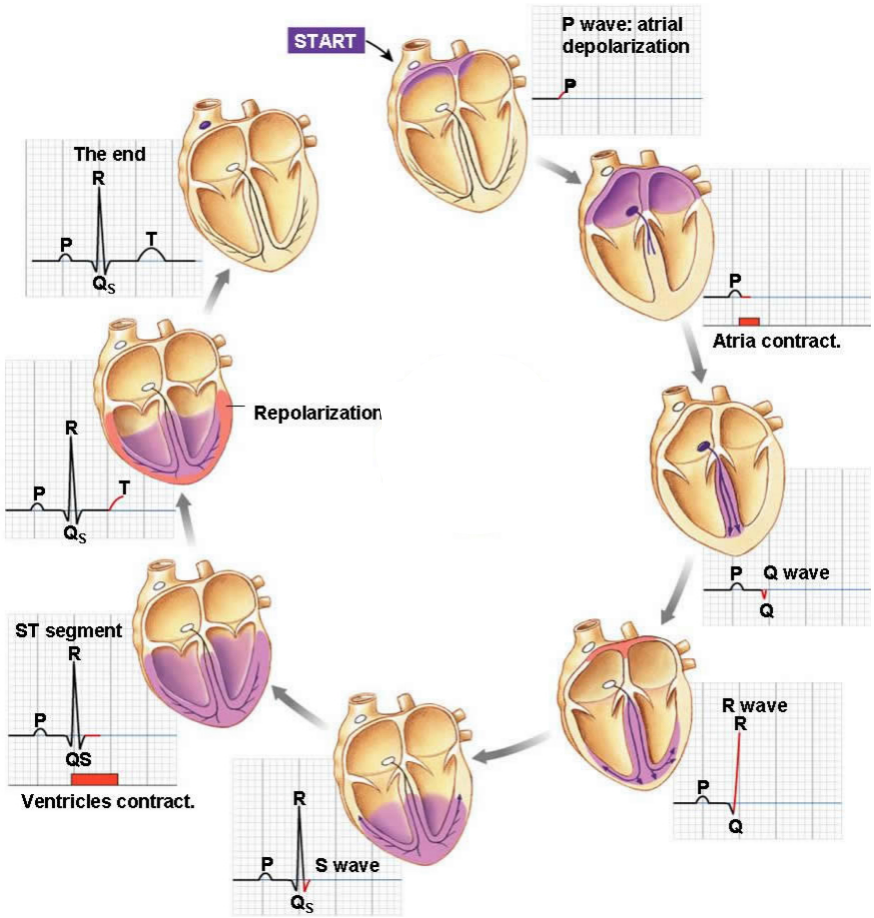

Figure 1.2.1. Electrical events of the cardiac cycle in relation to the ECG waves [6].

1.2.2. Heart rhythms and abnormal heart morphologies

A normal heart rhythm depends extremely of the electrical impulses originated in the SA node and produces heart rates between 50 and 100 beats per minute during resting state. Any deviation from or variation of this normal heart rhythm is called arrhythmia, which can be caused when depolarization initiates by other pacemaker cells than the ones in the SA nodes or when the conduction of the electrical impulses has been altered. These problems of conduction are connected to an area of the heart where the conduction of the cells is partially or totally blocked, which can lead to a delay on the propagation of the electrical impulse or a conduction failure and consequently a decrease in heart rate.

Ectopics beats or premature beats are these beats which start in any part of the heart other than the SA node interrupting or not a normal heart rhythm by occurring before the excepted time or once the electrical depolarization has already started.

When a premature beat occurs on the ventricles - ventricular premature beat, VPB - it interrupts the next sinus beat. Despite the fact that SA node depolarizes and repolarizes on time, the ventricular tissue cannot be depolarized cause it is already on the refractory period. The pause between a premature beat and the following sinus beat is called the compensatory pause. Also, the electrical impulse generated from a ventricular ectopic beat does not follow the normal conduction pathway, which produces an abnormally prolonged QRS complex and its morphology differs from the one produced by a normal sinus beat.

It is considered healthy to encounter isolated premature beats once in a while, but repetitive premature beats could be a manifestation of relevant cardiac diseases.

The most significant cardiac diseases that would be considered in the conduction of this project are described as follows:

- **Atrial arrhythmia**:

Atrial arrhythmia is the consequence of the occurrence of one or multiple ectopic beats in the atria. When these ectopic beats appear far away from the SA node, for instance closer to the AV node, the electrical impulse then propagates in the opposite direction from the normal one, which leads to an abnormal - negative - P wave representation on the ECG. Besides, when the ectopic beats occur near the ventricles, ventricular depolarization commences at the same time as does atrial depolarization, which in consequence conducts the P wave to coincide with the QRS complex and it cannot be detected on the ECG.

- **Ventricular arrhythmia**

Ventricular tachycardia, ventricular flutter and ventricular fibrillation are the most relevant diseases triggered for ventricular arrhythmia. The first one is due to an increased automaticity in the pacemaking cells of one or multiple focus on the ventricles; on the other hand, the second and third one result from the ventricles to be unsynchronized with the atria and beat at a rate which is much faster than the one on the atria.

Each one of these diseases follow different and hardly-detectable patterns on the ECG, although for instance ventricular tachycardia would probably show increased QRS width and amplitude and occlusion of P waves, whereas ventricular flutter would result into a large amplitude of any discernible QRS complexes or T waves.

- **Myocardial Ischemia**

Myocardial ischemia is considered an abnormal structural condition where the blood flow to the cardiac cells is restricted, causing a lack of oxygenated blood. Myocardial ischemia emerges when one or multiple coronary arteries has become narrowed and the demand for oxygenated blood to the heart increases. On an ECG, it can be detected by observing a morphologist change of the ST segment and the T wave.

- **Myocardial Infarction**

It provokes death of some cardiac cells by reason of sudden and abundant loss of blood supply, caused by a complete blockage of the coronary arteries resulting from arteriosclerosis - a build-up plaque that causes rupture on an artery so that a blood clot is formed and the artery is blocked.

The corresponding infarcted area is not electrically reactive so that the normal propagation pathway of the electrical impulse is altered. Consequently, the ECG representation differs greatly from the normal ECG.

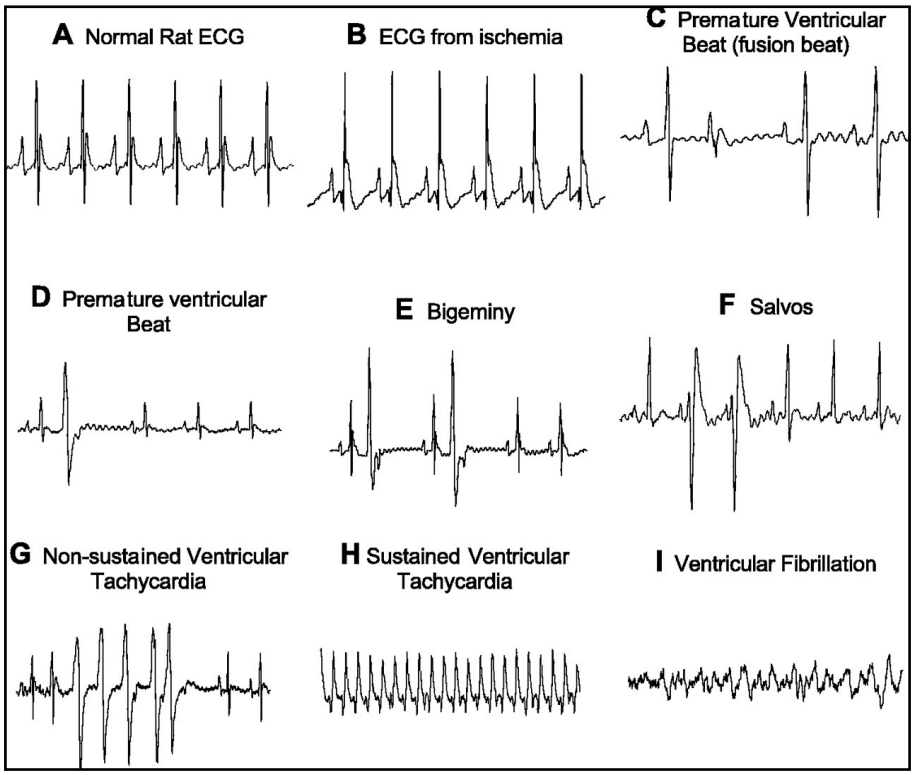

Figure 1.2.2. Examples of the Electrocardiograms per classified arrhythmias according to the Lambeth Conventions. A: normal ECG. B: ECG from ischemia. C: premature ventricular beat (PVB). D: PVB. E: bigeminy. F: salvos. G: non-sustained ventricular tachycardia (VT). H: sustained VT. I: ventricular fibrillation (VF). [7].

1.3. The Forward and Inverse Problem

1.3.1. Problem statement

Although it is medically possible to extract hypothetical diagnosis from an ECG signal, still the information about the current cardiac electrical activity that can be extracted from these non invasive measurements on the body surface is a non-specific non-accurate indicator for cardiac diseases.

To maximize such information, in addition with other numerical techniques applied directly to the body surface measurements, it is needed a biophysical source model to represent the heart electrical activity and its corresponding propagation pattern linked with the actual wavefronts observed in the ECG. Even so, since 1853 it is known that it is impossible to derive a unique specification of internal bioelectric sources taking just into observation the potentials on the body surface: multiples different sources may produce an identical data outside the actual source region.

The potential differences recorded between pre-defined sites on the body surface are a result of the heart electrical activity, which has been previously through passive tissues surrounding the actual source - the heart. Therefore, an electric volume conductor model may be defined to represent the spread of such electric currents within the tissues.

The problem of computing external potentials from an assumed internal source model is called **the Forward Problem**, whereas the determination of internal source potentials on the basis of the observed body surface potential differences is classed as **the Inverse Problem**. Considering the nature of the current flow within the tissues, the inverse problem has not a unique solution and can only be solved when assuming a given Forward model, involving also a **Source model** as well as a **Volume conductor model**.

1.3.2. Volume conductor models

Volume conductor models are aimed to describe a **approximate distribution** throughout the 3D space of the electrical conductivity on different mediums within a certain volumetric space.

First approaches were defined in a semi-infinite space, where the influence of the surface bounding these electric currents was encountered in image methods. Later on, other homogeneous approaches such as spheres, cylinders or spheroids were developed.

Currently, more realistic models of shaped tanks containing the source heart model are used, which allow conductivity to be inhomogeneous and/or anisotropic throughout several organs and the tissue within the body. To build up these models, numerical methods such as the Boundary Element Method (BEM), the Finite Difference Method (FDM) or the Finite Element Method (FEM) are implemented.

In regards to this project, the used volume conductor model has been composed from the Boundary Element Method. Briefly, this inhomogeneous method assumes a given conduction in the 3D space, taking the torso as the volume, by means of defining a system of integral equations, where each integral is taken over any 2D surface bounding a region of different conductivity. Thus, the volume would be extracted from the potential distributions along the **heart surface** and the **torso surface**, considering them as the **only two major boundaries** where the conductivity is dropped to zero.

Nowadays, very realistic geometries has been derived from anatomy textbooks through these methods. Besides, actual subject-specific geometries can be possibly extracted using Magnetic Resonance Imaging (MRI).

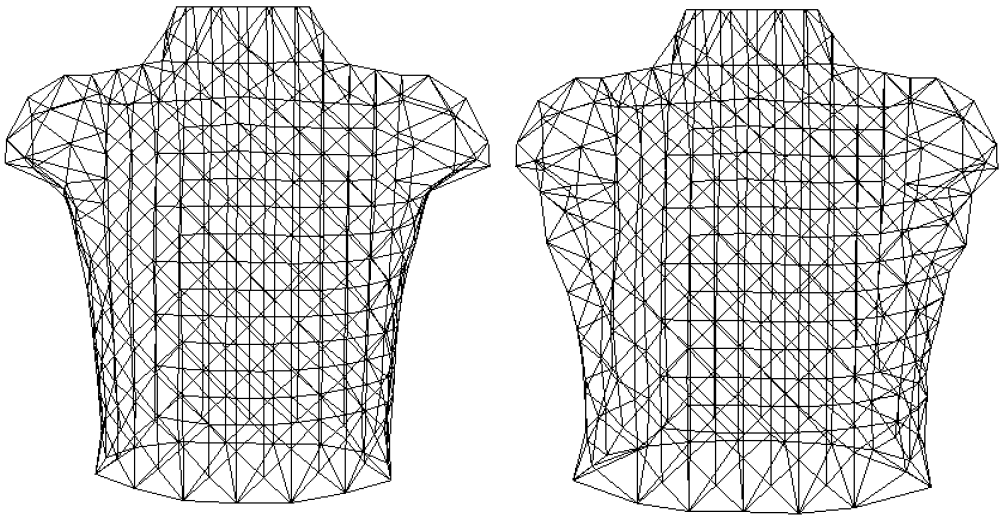

Figure 1.3.2. Standard torso geometry and Subject-specific torso geometry, respectively.

1.3.3. Source models

Source models are aimed to describe an **approximation of the electric potentials - the cardiac potential distribution** - along the enclosed surface of the heart. They may be composed of primary sources - which are the result of the electrical activation processes at the cellular membrane - and/or secondary sources - which are considered also as *virtual sources* and arise when the volume conductor model drops its conductivity to zero, which implies them to be placed in a medium of infinite extent - in this case the body surface, the skin [8].

From the starting point of view, elementary sources are point sources of a certain scalar magnitude. Therefore, to compute a potential produced by several sources, all of them are summed following the Coulomb's law for charge densities - the superposition theorem.

By the nature of the biochemical sources, the produced electric current is pumped around from the cellular membrane such that a current source volume density is generated. This density is represented by means of a distribution of current dipoles, which corresponds to the addition of all the contributions of these internal dipolar sources following the Poisson's equation.

Source models are classified on the basis of their dimension. Thus, point sources which their respective position is expressed through a single vector are source models of dimension zero - they encounter in the 1D space. On the other hand, potentials generated by the propagation of the action potential along the fibers may be defined as a linear source density distribution, and so this distribution is modeled by a function of a local variable - for instance, the fiber propagation pathways along the x-axis. These other sources are classed as source models of dimension one, as they are distributed on a 2D plane. Finally, the sources which can be represented as a distribution throughout the 3D space are called source models of dimensionality two, and will be the ones employed in this thesis. In fact, the source modeling the heart's electrical behavior would be represented as a **monolayer**, where each element of its surface would be considered to carry an elementary source along with its current surface density.

In particular, the source model that would be used in this project **approaches the cardiac potential distribution throughout a geometrical surface**, being the result from assuming possible enclosed current sources on the model.

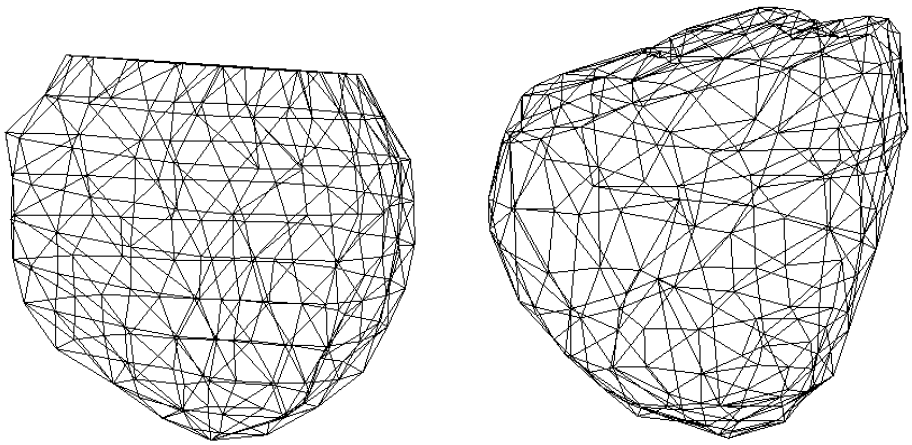

Figure 1.3.3. Standard heart geometry and Subject-specific heart geometry, respectively.

1.4. Objectives

Catheter ablation is a medical noninvasive procedure that uses radio-frequency energy to remove or terminate a damaged small area of heart tissue which is causing rapid and irregular heartbeats and thus treats developing cardiac arrhythmias such as atrial fibrillation, atrial flutter, supra-ventricular tachycardias (SVT) and Wolff-Parkinson-White syndrome. Still, catheter ablation is one of the most challenging procedures in cardiac electrophysiology because it is limited by non-sustained, poor and unmappable arrhythmias.

Computing inverse solutions to reconstruct the heart electrical activation and its corresponding spread throughout the heart has manifested increasing promise during the last two decades. Even so, properly detection of these cardiac diseases is directly correlated with the performance of the inverse-solving algorithm and the respective models in usage. In order to train such algorithm, it has to be tested with assorted data obtained from several subjects and provided by multiple research centers. When an algorithm's performance is accurate enough and capable of concretely simulating the heart electrical activation along diverse subjects then it is said to be reproducible.

To test such algorithms though has become a non-straightforward issue due to the lack of cooperation along research centers that have to deal with the problematic topic of sharing medical private data extracted from specific subjects.

This project is intended to be collaborative between multiple centers in order to validate the reproducibility of the inverse algorithms developed on the Electrical and Computer Engineering department in Northeastern University by means of electrocardiographic data provided by another research center.

This medical data has been extracted from Computer Tomography registered scans of catheter interventions and it is supplied from the Department of Medicine and the Department of Mathematics and Statistics from Dalhousie University, Canada.

Furthermore, automaticity would be another principal goal which this project would be focused on by the design of a complex pipeline involving the detection of the appropriate regularizing parameter on the inverse-solving algorithm and the computation of reconstructed heart potentials throughout two different geometries - the first one just composed of epicardial nodes and the second one also including endocardial nodes - per numerous heartbeat measurements of several subject-specific cases.

The other main aims which this project is about are the analysis, review, comparison and cross-validation of the obtained results on these multiple variants as well as the conclusion of the role in which every part plays through specialized simulation programs from the field and the euclidean distance as a numerical error measurement.

The simulation program to appropriately visualize the results would be MAP 3D which enables the user to plot a specific geometry - for instance, the heart or the torso - and map the computed reconstructed potential values at each node of that geometry during a given time sequence. Another program that would act as a helpful tool would be SCIRun which provides the possibility of combining appropriate modules to simulate and construct inverse solutions and visualize mathematical functions such as the gradient estimation of those reconstructed solutions.

Finally and if applicable, the inverse algorithms of the pipeline would be improved in order to ensure their automaticity as well as reproducibility on the maxim possible contexts.

1.5. Previous Work

Inverse electrocardiography is based on the characterization of the heart electrical activity at its cells from previously recorded remote body surface electrocardiograms (ECGs). Nowadays, as an everyday practice, clinicians use the ECG to determine cardiac diseases on patients by means of a current dipole model of the electrical activity in the heart. This practice, in addition with the fact that it provides qualitative results rather than quantitative ones, is also performed in almost real time, enabling the medics to validate the results by adding more constraints and confirming the obtained diagnosis.

Apart from this actual technique, electrocardiography has other quantitative formulations based on multichannel ECG measurements - or also called body surface potential maps - which along with a mathematical model of the bioelectric source they represent the cardiac electrical activity by estimating the potential values throughout the modeled source.

In 1988-89, several reviews written by Rudy and Messinger-Rapport and Gulrajani reported the situation in which the field of inverse electrocardiography at that time was found [9][10][11][12][13][14]. Those papers though, just described the basic methods to solve the inverse problem and their respective results were clinically unconvincing and unreliable.

Research conducted during the following years was focused on increasing the reliability of the obtained results by introducing more a priori information - constraints - to the geometrical models and by adding more robustness to the inverse-solving methods, reducing thus uncertainties and being able to justify computed results. Recent progress on the field has been developed by authors such as Horácek and Greensite [15][16].

As mentioned previously, this bachelor project would be intended to solve, compare and analyze multiple variant quantitative formulations of these inverse electrocardiography problems.

2. Background Theory:

2.1. The Forward model

In the reconstruction of the electrical activity throughout the heart, the first step is based on computing the required geometrical elements, which are the bioelectrical source model represented by a mesh of all the connected heart nodes and a volume conductor model which consists of the torso tank mesh along with the electrical conductivity within the enclosed volume.

As said previously, the construction of this volume conductor geometrical model requires anatomical information extracted from MRI scans. Once the images are obtained, they are segmented and the electrode locations employed when recording the body surface electrocardiograms (ECGs) are mapped into the resulting nodes of the torso mesh. Any other anatomical structure segmented from the images is also represented as a set of nodes in space linked to the mesh in question. However, despite the fact that these other structures, which correspond to internal organs, have different conductivities within the volume of the torso, they are assumed to be an homogeneous conductivity throughout the volume model. Besides, this volumetric geometry is only computed once per all the time instants - it is treated static in time - and thus possible changes on the torso of the patient while recording the ECGs are omitted.

The Forward model consists of obtaining these geometries by defining specific solutions either including volume integral equations from quasi-static versions of **Maxwell's equations** or applying **the Green's Theorem** to surface integral equations. These formulated equations are then solved over the nodes of the geometry mesh by means of numerical techniques such as FEM for volume equations or BEM for surface equations.

Unlike BEM, FEM requires the entire volume, including the surrounding regions, to generate a system of linear equations and thus calculate the potential values at the nodes which are lying on the faces of each volumetric element [17]. The resulting equations are extracted from minimizing over an energy function based on the fundamental laws of potential theory. Apart from the fact of dealing with very large linear systems of equations and consequently the difficulty of modeling the required volumetric geometry, FEM allow the condition of anisotropic conductivity within the volumetric mesh and its resulting matrices are sparse.

On the other hand, BEM is also based on the fundamental laws of potential theory but it expresses them as differential equations of Poisson or Laplace in the spatial domain, and thus the resulting integrals are over the boundaries of the surface elements. This reduction of dimensionality, in terms of the degree of freedom of the equations, allows the use of fewer nodes for describing the volumetric mesh and reduces the computational cost since the number of linear systems to be solved is lower. Even so, BEM has a limitation of the ability to handle anisotropy conductivity and the resulting matrices are not sparse.

Boundaries are defined according to the Neumann boundary condition, i.e. when the medium outside a given surface S is considered to be non-conducting. Therefore, the potential at an arbitrary point within a bounded medium is the sum of the infinite space potential at that point and a weighted sum (an integral) of the potentials at the boundary. In fact, taking into consideration that every given surface S is represented as a set of triangles, there exist two different numerical formulations to calculate the potential value at a given node. The first and original one consists of computing the center of gravity of all the triangles connected to the node at which the potential value is computed. By contrast, the other formulation is based on the potential computation at the vertices of the triangulated surface, which provides a direct link of observation of the potential map along the volumetric mesh.

To conduct this project, the volume conductor geometry has been extracted by using BEM and its corresponding potential values has been computed at the vertices of the triangular mesh.

The Forward matrix or Transfer matrix is based on establishing a linear relation between every body surface potential mapped into the torso geometrical mesh and all the nodes composing the heart geometrical mesh. And as the Forward model does, the Forward matrix is static in time as well.

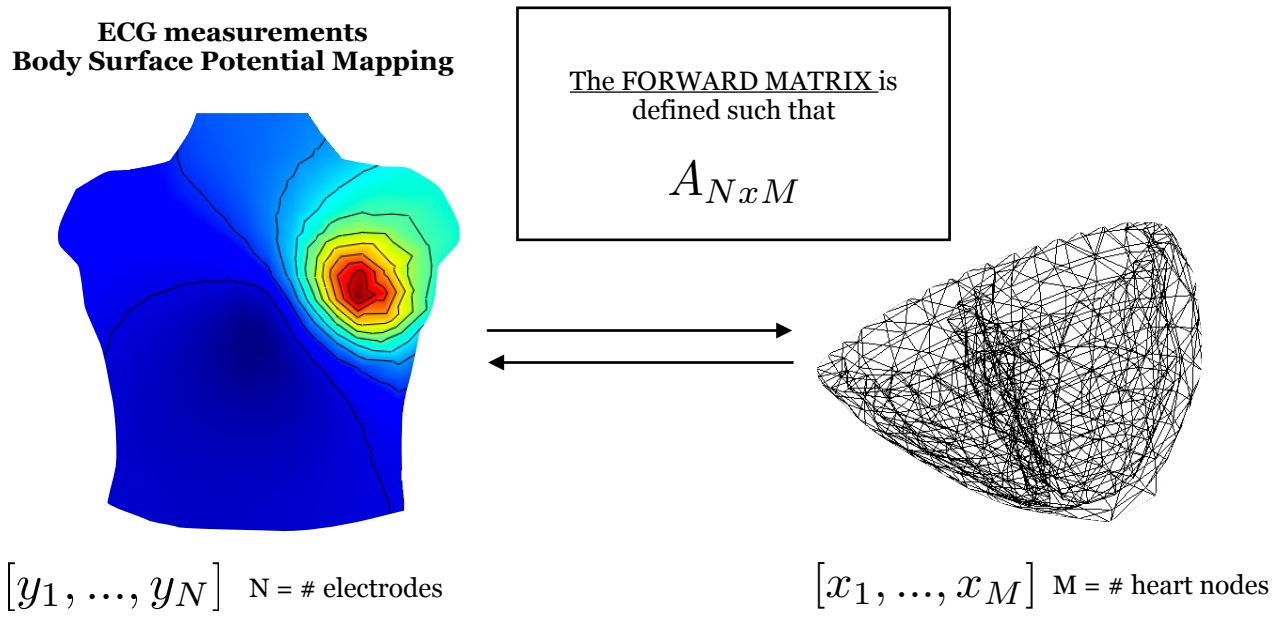

Figure 2.1.1. Linear relationship between every node in the torso mesh and all the nodes in the heart mesh established by means of the Forward Matrix.

At a given time instant, the respective potential values per every node of the heart mesh would be stored in a vector, and would also do so the body surface potential values per every node on the geometry of the torso. Therefore, the resulting solution relating both vectors would be a matrix, where every row can be treated as a set of weights that indicate how sensitive each node on the heart is per every node on the body surface. As a result, the complete Forward matrix describes the sensitivity map with which the modeled heart comes, per every node allocated in the torso mesh.

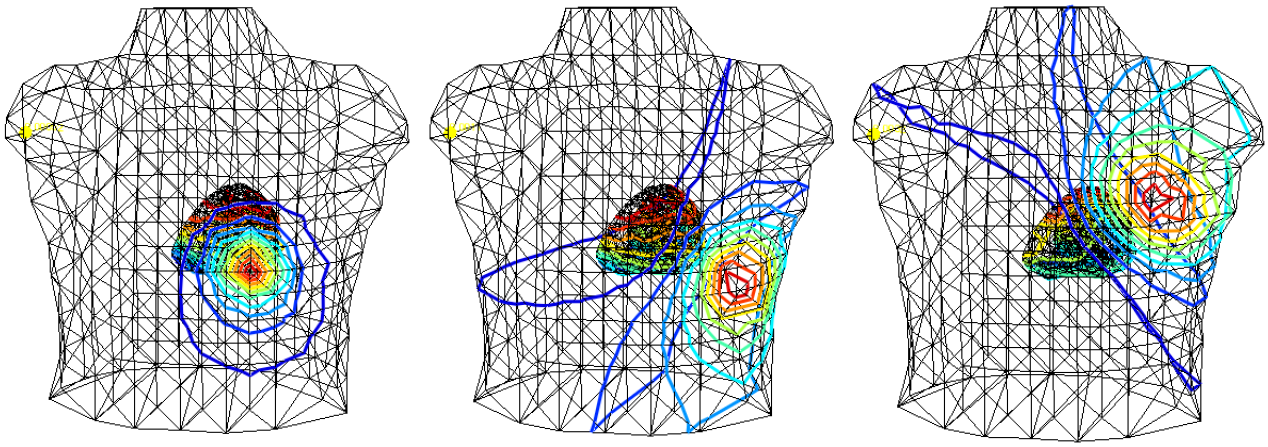

Figure 2.1.2. Sensitivity maps per three differently allocated nodes in the torso mesh.

Lastly, the Forward matrix is composed by values lower than one since the electrical activation would be always attenuated: it propagates from the cells of the heart to the body surface through the blood, different tissues and several internal organs.

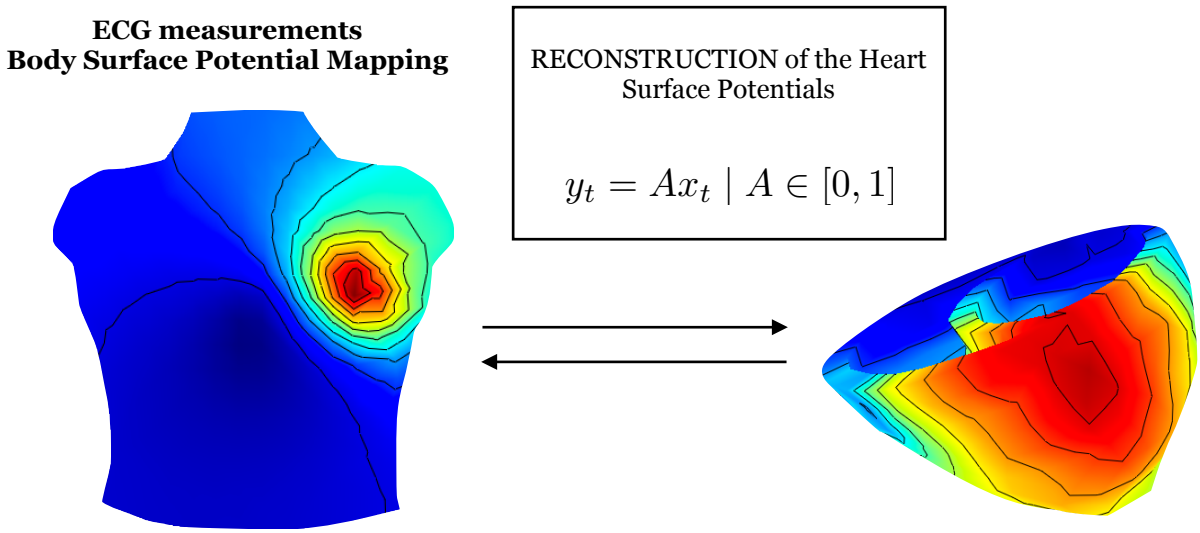

Figure 2.1.3. Once the Forward Matrix is extracted, it is possible reconstruct the Heart Surface Potentials.

2.2. The Inverse and Forward problems

2.2.1. Problem statement

As seen in the section 1.3.1, the inverse problem is based on the estimation of the heart electrical source from the body surface potential differences previously measured. Consequently, the forward problem consists of computing the external potentials in the body surface given a volumetric model of the torso and assuming a bioelectric source. Unlike the inverse problem, the forward problem provides a unique solution for the body surface potentials as it follows the linear equation presented above. By contrast, solving the inverse problem is not straightforward due to the non-unique relationship between the cardiac source and the remote measurements - given a heart model, there exist infinite possible source configurations that could create the same set of body surface potentials [18].

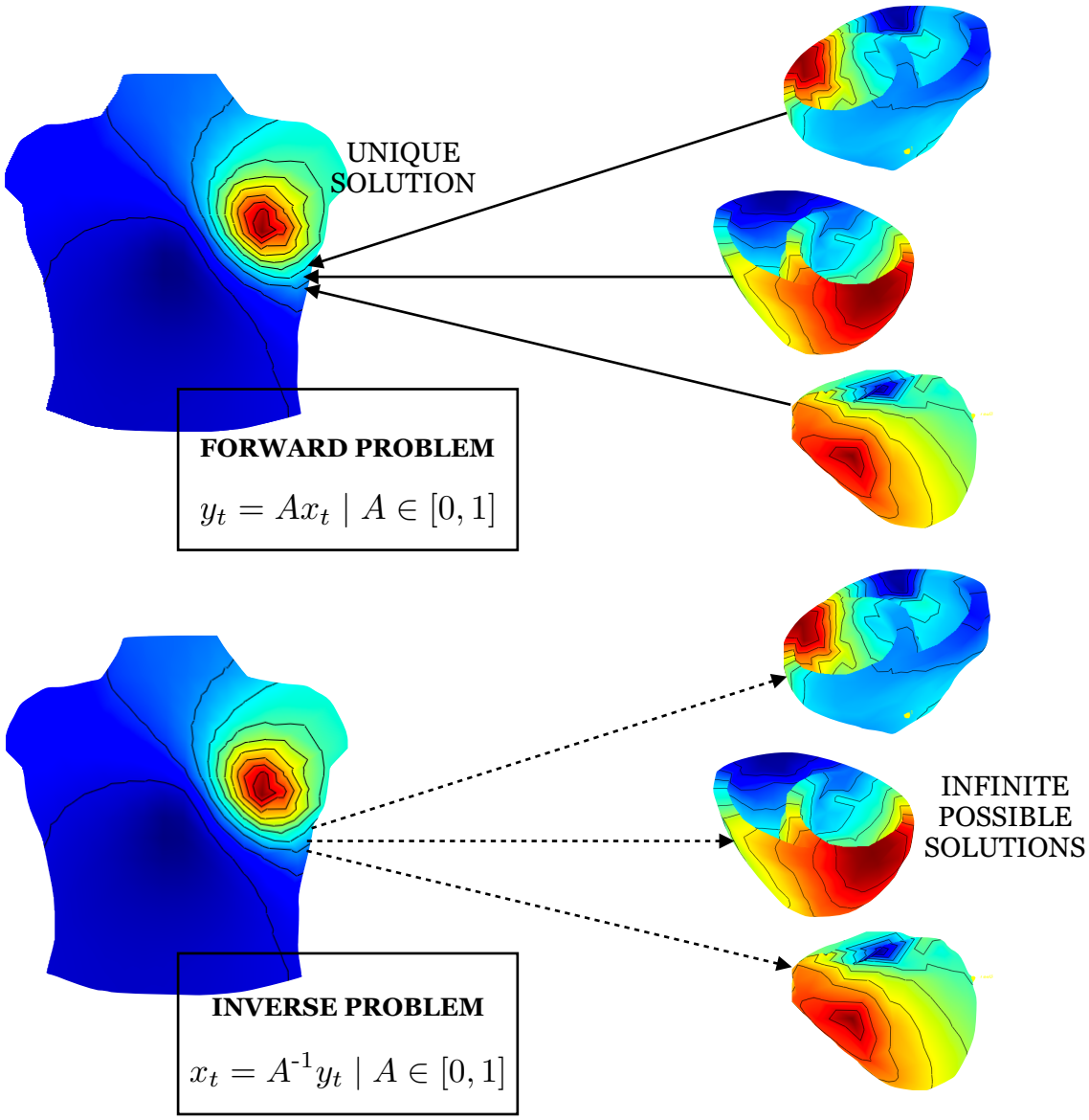

Figure 2.2.1. The Forward and Inverse Problems.

Besides that, **the Inverse Problem** is ill-posed due to multiple reasons presented below:

- **Unavoidable noise introduced when recoding the ECGs:** In the pursuit of solving the inverse problem, small perturbations in the body surface potentials would result as a considerable error in the reconstructed solutions of the cardiac potentials, to the extent which the Forward Matrix would relate both of them. These small perturbations are caused by noise introduced during the recording of the ECGs due to either non-idealities in the equipment or friction between the electrodes and the subject's skin.
- **Inhomogeneous conductivities within the volume conductor model:** Despite the fact of assuming an homogeneous conductivity throughout all the elements enclosed in the mesh, the human torso is composed by internal organs, tissue and mostly blood that have different material conductivities and that should be taken into consideration when defining the model. This assumption causes the Forward Matrix to be non-ideal, and thus ill-posed.
- **Subject's Respiration:** As mentioned in the previous section, the volumetric model is computed once for all the time instants, i.e. it is treated static in time. However, the actual geometry of the subject does change meanwhile the potentials are being recorded by reason of the breath. Respiration causes movement of the heart and consequently its position within the geometry changes during the ECGs recording. This statement leads to the need of adapting and computing iteratively the Forward Matrix in real time, because otherwise it would be ill-posed as well.
- **Spatial superposition of the electric fields:** The volume conductor model is constructed by the superposition theorem - i.e. the effect of multiple current sources would be the direct sum of the effects of the elementary sources involved in the complete source - which relates both the nodes placed in the torso and the heart by means of a linear function classed as the Forward Matrix.
  Hence, a given potential value in the torso is the linear combination of all the potentials along the heart, each of which being pondered with a weight in function of its proximity towards the given node in the torso.
  The Forward Matrix also acts as a spatial low-pass filter - it computes a pondered average of all the heart nodes per every node in the torso such that large potential differences between consecutive nodes in the heart would be negligible on the resulting potential value in the torso.
  In consequence of this linear relation, small perturbations on the recorded body surface potentials would lead to extremely unstable inverse potentials on the heart. Therefore, the Forward Matrix is not invertible in practice.

All of these problematic issues contribute in reducing the reliability of the reconstructed heart potentials and call for the need to seek other formulations to solve the inverse problem.

2.3. Solve the Inverse problem

In order to attempt solving the inverse problem, it is needed dealing with two troublesome characteristics that are intrinsic to the pose of the problem itself:

1. Regarding to the first problematic stating that there is no existence of a unique solution for the reconstructed heart potentials, it would be assumed on the formulation of the problem that is has a well-defined solution - a unique source model configuration to cause the set of body surface potentials.
2. In terms of reducing unavoidable noise errors in the data or possible inaccuracies in the definition of the Forward Model, a priori physiological information would be imposed by adding constraints to the mathematical formulation for solving the problem and thus obtain stable inverse solutions.

The most widely used approaches to this problem are the Tikhonov regularization and the Truncated Singular Value Decomposition (TSVD), although the most common technique is by far the Tikhonov regularization.

While Tikhonov regularization impose the constraints by adding a regularization term to the mathematical formulation, TSVD attempts to remove the deviations on the Forward Matrix by truncating its singular values and so enabling to solve the problem with a well-conditioned rank transfer matrix.

2.3.1. Tikhonov regularization

The Tikhonov regularization is a minimization problem over the possible inverse solutions expressed as a least-square cost function of two complementary terms.

The first term is classed as **the fitting term** and represents the residual error between the recorded body surface potentials and the estimated ones that would result from a given Forward Model. Therefore, the smaller the residual error, the closer the resulting inverse solutions will be to generate, through the Forward Matrix, a set of body surface potentials equal to the real data.

The second term is classed as **the regularization term** and is in charge of penalizing large values of a chosen property of the inverse solutions. Hence, unstable inverse solutions ill-posed by small perturbations on the recordings can be moderated.

The mathematical formulation of the Tikhonov regularization is presented as follows:

$$\min_{x_t} \underbrace{||Ax_t - y_t||_2^2}_{\text{Fitting TERM}} + \underbrace{\lambda||Rx_t||_2^2}_{\text{Regularization TERM}}$$

Where every element corresponds to:

- **A:** the forward matrix.
- **y:** the recorded potentials on the thoracic surface.
- **x:** resulting inverse solutions of the reconstructed cardiac potentials.

- λ **:** the regularization parameter.
- **R:** the regularization matrix. A specific property or estimation of the results.
- **Rx:** the constraint or regularizer. It is the result from the multiplication of the regularization matrix by the inverse solutions that conforms the particular spatial representation of the reconstructed potentials to be regularized.

Despite the fact that the minimization could be solved by means of a l1_norm or a **l2_norm least-square problem**, in this project it will be used the second formulation since it provides a mathematically less complex manner to solve the problem.

This regularization technique can also be described as a method to achieve inverse solutions by establishing a **trade-off** between fidelity to the **recorded data** - small residual error and thus likely unstable and non-linear results - and fidelity to the **imposed regularizer** - small regularization error which imply a lost of the remote cardiac information and the obtention of unrealistic inverse solutions.

As presented on the equation above, this trade-off is weighted by the value of the regularization parameter, λ :

$\lambda \downarrow\downarrow\downarrow$ $\quad y_t \approx Ax_t$ Fidelity to the **Data**

$\lambda \uparrow\uparrow\uparrow$ $\quad x_t \approx 0$ Fidelity to the **Constraint**

The development of the minimization problem ends up with the expression below, where it can be observed that the regularization parameter, placed on the denominator of the equation, attempts to compensate the low values of the singular values that cause the ill-condition of the Forward Matrix [19].

$$A = USV^T$$

$$x = (A^T A + \lambda I)^{-1} A^T y$$

$$\sum_{i=1}^{r} \left(\frac{\sigma_i}{\sigma_i^2 + \lambda}\right) v_i u_i^T y \longrightarrow \sigma_i^2 << \sigma_i^2 + \lambda$$

FILTER FACTOR

There are two decisive issues applying to the regularization that directly influence on the retrieved results:

- **Choosing the appropriate regularization parameter.**

Although there exist numerous techniques to obtain this parameter, this project would only conduct one *a posteriori* technique, which consists of solving the minimization problem iteratively per a given set of regularization parameters and then choosing the one that best provides inverse solutions.

$$\forall \lambda_k \ , \quad k \in \{1, K\}$$

This *a posteriori* technique leads to the need of also choosing the following items:

- **First and last samples** of the given set of regularization parameters.
- **Number of samples** included in the set.
- **Criterion in which samples are distributed** within the set.

The choices selected as well as the criterion to properly determine the regularization parameter which accomplishes best the trade-off will be explained in the section 2.3.2, L_curve.

- **Choosing the appropriate regularization matrix.**

The resulting inverse solutions would vary in function of the chosen regularization matrix, because the regularization would be applied to a particular spatial estimation of the results per every case.

Therefore, in order to examine how the potential distribution varies along the heart in function of the regularization applied, inverse solutions per different regularization matrices, each of which reflecting a particular spatial property, would be computed.

2.3.1.1. Types of regularization matrices

As explained in the previous sections 2.3 and 2.3.1, solving the inverse problem requires the imposition of prior knowledge by adding one or more constraints, i.e. regularizing the inverse solutions.

Tikhonov regularization adds this prior knowledge through the second term of the minimization least-square problem: $||Rx_t||_2^2$ .Consequently, the type of prior knowledge imposed in the inverse solutions will be directly related to the choice of the regularization matrix.

The regularization matrix is composed by a set of elements that define a particular spatial property along a surface of a given dimensionality. In this case, the regularization matrix is applied to the potentials defined on the surface of the heart mesh, so the multiplication of the matrix by the inverse solutions $Rx_t|$ would result as an estimated potential distribution of a given spatial property along the heart surface.

In the following sections, four distinct regularization matrices would be described as follows: its spatial definition, how the estimation of its spatial distribution changes along the heart surface and the spatial behavior of the resulting potential distribution when applied to the regularization.

2.3.1.1.1. Identity Regularization

The Identity matrix or unit matrix is the simplest non-trivial square matrix in linear algebra, composed by ones on the main diagonal and zeros elsewhere:

$$I = \begin{bmatrix} 1_1 & \cdots & 0 & \cdots & 0 \\ . & & . & & . \\ 0 & \cdots & 1_i & \cdots & 0 \\ . & & . & & . \\ 0 & \cdots & 0 & \cdots & 1_N \end{bmatrix}$$

It is invertible, idempotent - i.e. when multiplied by itself, yields itself - and full rank - all of its elements are linearly independent [20].

The identity matrix is defined such that

$$I_x = diag(1_1, \cdots, 1_N) x_1^N = x_1^N$$

for all the vectors *x* belonging to the real domain.

Ergo, when the Identity matrix is applied to the regularization, the regularizer *Rx* equals to the inverse solutions themselves, x, which means that the **unique constraint** imposed by the regularization is the resulting **inverse solutions to be small**.

$$\min_x ||I_x||_2^2 \longrightarrow x_1^N \approx 0$$

2.3.1.1.2. Hessian Regularization

The Hessian matrix comprises the second-order derivatives of a scalar-valued function *f*, also defined as function such that $f : \mathbb{R}^n \rightarrow \mathbb{R}$, where the input is a vector $x \in \mathbb{R}^n$ and the output is a scalar $a = f(x) \in \mathbb{R}$.

Assuming that all the second-order derivatives of the function exist and are continuous over its domain, the Hessian matrix result as a square matrix expressed as follow:

$$H_{x_i} = \begin{bmatrix} \frac{\partial^2 f}{\partial x_i^2} & \frac{\partial^2 f}{\partial x_i \partial y_i} & \frac{\partial^2 f}{\partial x_i \partial z_i} \\ \frac{\partial^2 f}{\partial y_i \partial x_i} & \frac{\partial^2 f}{\partial y_i^2} & \frac{d^2 f}{\partial y_i \partial z_i} \\ \frac{d^2 f}{\partial z_i \partial x_i} & \frac{\partial^2 f}{\partial z_i \partial y_i} & \frac{\partial^2 f}{\partial z_i^2} \end{bmatrix}$$

If the function *f* is over multiple variables, then it is said that the Hessian matrix's spatial property is to describe the curvature of the function.

Let's consider that the surface of the heart is given by a graph expressed as a function **f(x,y,z)** such that f : $\mathbb{R}3 \rightarrow \mathbb{R}$, where x,y,z are the coordinates of the surface in the 3D space [21].

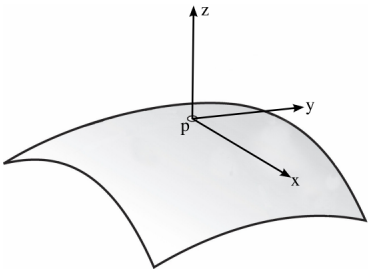

Then, the linear approximation of the Hessian operator ***Htan*** is computed over the function expressed as follows:

$$f(x_i, y_i, z_i) \mid i \in 1, N$$

Where N is the number of nodes in the heart mesh and f(x,y,z) a supposed potential distribution defined by the 3D coordinates (x,y,z) of that mesh.

Applying thus the operator Htan to a particular potential distribution on the heart mesh, it retrieves its respective Hessian estimation.

Htan: x → Hx

Therefore, the computation of the constraint *Hx* results as the Hessian estimation of the inverse solutions distribution along the heart mesh - which would represent the curvatures of the resulting potential distribution over the cardinal coordinates along the heart mesh.

In overall, this estimation retrieves the second derivate of the function - it captures the spatial shape change along the potential values of a given distribution - and thus provides a measure of the curvature - it either amplifies positively or negatively the potentials placed on the curvatures of the function or attenuate them if potential distribution is flat - i.e. no amplitude variation among consecutive potentials.

$$\min_x ||H_{x_1^N}||_2^2 \longrightarrow H_{x_1^N} \approx 0$$

Even though, minimizing **the Frobinius norm** of the hessian estimation does not guarantee the reduction of the curvature of the function - the elements of the hessian estimation can be cancelled with each other and thus the provided measure would be unreliable. For this reason, the Laplacian matrix is used as a surrogate operator to calculate the curvature of the function given by the potential distributions.

2.3.1.1.3. Laplacian Regularization

The Laplacian matrix *Ltan* is a linear operator that also measures the curvature of a function *f*. Unlike the Hessian operator though, the Laplacian matrix maps the entire curvature of the function to a single scalar value. The Laplacian estimation is calculated through the Hessian estimation by the equalities presented below:

$$L_{x_i} = \mathrm{tr}(H_{x_i}) = \frac{\partial^2 f}{\partial x_i^2} + \frac{\partial^2 f}{\partial y_i^2} + \frac{\partial^2 f}{\partial z_i^2}$$

As in the Hessian estimation, the Laplacian matrix is a function expressed as follows:

Ltan: x → Lx

And it is defined such that the resulting Laplacian estimation Lx of a given potential distribution x would be composed by positive values when the distribution becomes convex, negative values when the distribution becomes concave and nearly zero when the distribution is roughly flat. Therefore, unlike the Hessian matrix, the Laplacian matrix describes **the local curvatures** of a function.

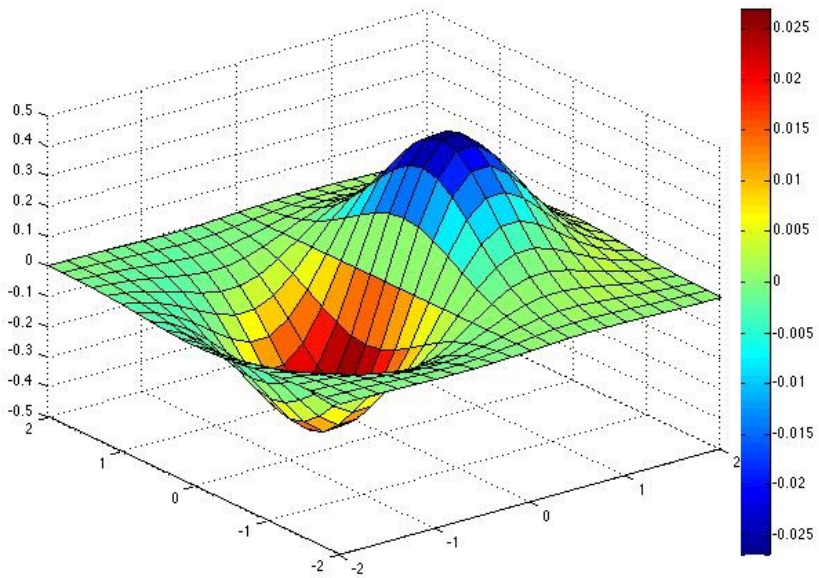

Figure 2.3.1.1.3. Example of the retrieved values from a Laplacian estimation over a given distribution in function of its local curvatures.

Another estimation of this local curvature could be the sum of the eigenvalues of the Hessian estimation, which corresponds to its trace. Given multiple curvature estimations over the directions x,y and z in a particular node, this measure would represent which one mask the others and thus is the main curvature estimation locally in that node.

The steeper the curvature spatially is, the larger - either positive or negative - the estimated value on the Laplacian would be. Therefore, the Laplacian matrix acts as a spatial high-pass filter along the potential distribution - it emphasizes the potential variations between consecutive nodes.

So by means of imposing this constraint in the regularization, these large values of the resulting potential distribution, which correspond to abrupt changes in space and fast variations in time, would be stabilized; providing then results that change smoothly along the surface of the heart.

$$\min_{x} ||L_{x_1^N}||_2^2 \longrightarrow L_{x_1^N} \approx 0$$

This regularization is one of the most widely used ones, since it imposes the physiological recognized constraint that electrical potentials between consecutive nodes do not almost vary, except for the ones where the electrical activation wavefront arises.

This trade-off between assuming a spatially smooth distribution of the potentials and simultaneously preserve an acceptable and realistic propagation of the electrical wavefront is controlled by the regularization parameter previously explained in the section 2.3.1.

2.3.1.1.4. Gradient Regularization

The gradient function over three multiple variables is expressed as follows:

$$D_{x_i} = \nabla f(x_i, y_i, z_i) = \left[\frac{\partial f}{\partial x_i} \quad \frac{\partial f}{\partial y_i} \quad \frac{\partial f}{\partial z_i}\right]$$

Where the first derivative of a given function F is computed over the variable x, the variable y and the variable z. These derivates indicate numerically how much the function F changes for a change in either variables [22].

As it has been seen in the section 2.3.1.1.2, in order to apply the regularization, the gradient matrix *Dtan* would be computed over the surface of the heart mesh, considering **f(x,y,z)** as the function given by the potential distribution along the nodes of the heart surface.

Considering the gradient matrix *Dtan* as the function that retrieves a gradient estimation Dx of a given potential distribution x, the gradient operator is defined such that

Dtan: x → Dx

And aimed at estimating the direction with which a function progresses spatially. Thus, the resulting gradient estimation of a given potential distribution would show vectors tangent to the surface, since all the the potential distributions would change along the surface of the heart mesh, and not along its volume.

By minimizing this gradient estimation, the regularization would pale abrupt and quick spatial changes among the reconstructed potentials and thus provide a smoother potential distribution along the heart surface.

$$\min_{x} ||D_{x_1^N}||_2^2 \longrightarrow D_{x_1^N} \approx 0$$

As the Laplacian regularization, the Gradient regularization also approximates spatially stable reconstructed cardiac potentials but it deals with the problematic of preserving realistic activation patterns as well - apply a balanced regularization parameter that constraints the potentials to change spatially smoothly along the surface and also keeping a realistic activation of the electrical wavefront.

2.3.1.1.5. Extended Gradient Regularization: Transmural Derivative Regularization

As previously mentioned in the section 1.1, the heart's electrical activation wavefront propagates along the transmembrane of the heart as well as across the cardiac ventricular muscle. For this reason, when regularizing the potential distributions on the heart, the spatial smoothness should be imposed not only along the neighboring nodes on the surface but also including the nearby nodes from both endocardial and epicardial surfaces [23].

Unlike the previous Gradient regularization, this extended regularization would approximate the derivatives of the potential distributions transmurally, by simultaneously estimating the Gradient and the Hessian of a scalar function over the set of point measurements on the heart.

In order to define the local neighbors per each node, the mesh of the heart would be discretized into three dimensional points - considering the geometry of the heart as a volumetric mesh - and the pairwise distances among all the node coordinates would be computed. Therefore, the corresponding local neighbors would be given by a weight function that will be detailedly explained in the section 2.3.1.1.5.2.

2.3.1.1.5.1. Description

Let's consider a scalar function V: $\mathbb{R}3 \rightarrow \mathbb{R}$ defined such that

$$\mathbf{V: (x,y,z) \rightarrow v}$$

Where

- **v** is the voltage at a certain node of the heart mesh
- **(x,y,z)** are the position coordinates of this node in the 3D space

The main goal of this regularization is to minimize as possible the voltage variations between a given node and its neighbors, including both the ones belonging to endocardial and epicardial surfaces.

A voltage variation between nodes can be expressed by means of the function V as the amount of change on the voltage function when there is a displacement over the variables x,y and z. This is mathematically, the gradient of V(x,y,z) between two points.

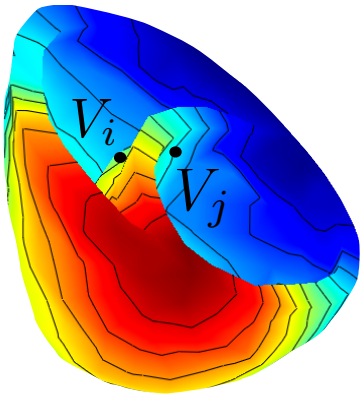

$$V_j - V_i \approx 0$$

$$\nabla V_i \approx 0$$

Figure 2.3.1.1.5.1.1. The basic aim of the proposed Transmural Derivative Regularization.

The theorem of Taylor states that given a continuous and k_times differentiable function *f* over a real variable, the function around a particular point *x* can be linearly approximated by a k-th order Taylor polynomial. Particularly, the second-order Taylor polynomial is expressed as follows:

$$p_2(\boldsymbol{x}) = f\left(\boldsymbol{x}^{[0]}\right) + \nabla f\left(\boldsymbol{x}^{[0]}\right)'\left(\boldsymbol{x} - \boldsymbol{x}^{[0]}\right) + \frac{1}{2}\left(\boldsymbol{x} - \boldsymbol{x}^{[0]}\right)' \nabla^2 f\left(\boldsymbol{x}^{[0]}\right)\left(\boldsymbol{x} - \boldsymbol{x}^{[0]}\right)$$

Figure 2.3.1.1.5.1.2. Lineal approximation of a given function f with a quadratic Taylor polynomial [24].

Where the second term corresponds to the estimation of the Gradient and the sixth to the estimation of the Hessian, both between two particular points.

Thus, by defining **pi = (xi,yi,zi)**, where *i* goes from 1 to N, as the entire set of nodes of the heart mesh and **Vi** as the potentials at those nodes, **the Gradient and the Hessian** at *pi*, denoted by ***Di*** and ***Hi*** respectively, can be estimated by the linear approximation of the voltage at pi and its local neighbors:

$$p_i = (x_i, y_i, z_i) \mid i \in [1, N]$$

$$p_{ij} = (x_{ij}, y_{ij}, z_{ij}) \mid p_{ij} = \begin{bmatrix} p_{11} & \cdots & p_{1P} \\ p_{N1} & \cdots & p_{NP} \end{bmatrix}$$

where
- N = # heart nodes
- P = # neighboring nodes per p_i

$$V_{ij} \approx V_i + \nabla V_i'(p_{ij} - p_i) + \frac{1}{2}(p_{ij} - p_i)'\nabla^2 Vi(p_{ij} - p_i)$$

$$V_{ij} - V_i \approx D_i^\top (p_{ij} - p_i) + \underbrace{\frac{1}{2}(p_{ij} - p_i)^\top H_i (p_{ij} - p_i)}_{\mathbf{A}}$$

As the expression *A* would result in an scalar, and thus it can be applied the cyclic property of the trace, the formulation above would end up in the following equation:

$$V_{ij} - V_i \approx \begin{bmatrix} D_i^\top & vec(H_i)^\top \end{bmatrix} \begin{bmatrix} (p_{ij} - p_i) \\ \frac{1}{2} vec((p_{ij} - p_i)(p_{ij} - p_i)^\top) \end{bmatrix}$$

Finally, the approximation presented above would be solved for every node through a least-square minimization problem over the matrix *F*:

$$\min_F ||V_i - F_i V_{ghi}||_2^2$$

Where

$$V_i = \begin{bmatrix} g_{i1}V_{i1} - V_i & \cdots & g_{iN}V_{iN} - V_i \end{bmatrix}$$

$$F_i V_{ghi} = \begin{bmatrix} D_i^\top (p_{i1} - p_i) + \frac{1}{2}(p_{i1} - p_i)^\top H_i (p_{i1} - p_i) & \cdots & D_i^\top (p_{iN} - p_i) + \frac{1}{2}(p_{iN} - p_i)^\top H_i (p_{iN} - p_i) \end{bmatrix}$$

Being *g* the weighting function, which would be explained in the following section.

The resulting matrix F is the linear operator *cDf* defined such that, from a given potential distribution x, it returns the **Transmural Derivative Estimation TDx** - i.e the combination of the Gradient and the Hessian estimations:

$$TD_x = Fx$$

2.3.1.1.5.2. Choosing sigma and the weight function

The weight function is a radially-symmetric inverse exponential function that defines the local area of neighborhood along the heart mesh for any given node *pi = {xi,yi,zi}*. In order that any particular node could have a finite set of neighbors in the heart mesh, the weight function has been truncated at a pre-defined threshold, E. The weight function per every point composing the heart mesh is expressed as follows:

$$g(x_i) = exp^{(-\frac{||p_{ij} - p_i||_2^2}{\sigma^2})}$$

$$\phi(x_i) = \begin{cases} g(x_i), g(x_i) \geq \epsilon \\ 0, g(x_i) < \epsilon \end{cases}$$

It can also be expressed as a NxN square matrix where every row *i* corresponds to all the assigned weights - valued between [0,1] - relating all the nodes of the heart to a particular node *i*.

$$g_{ij} = \begin{bmatrix} g_{11} & \cdots & g_{1N} \\ g_{N1} & \cdots & g_{NN} \end{bmatrix} \mid g_{ij} \in [0,1]$$

The sigma parameter σ^2 controls the decay of the weight function's values for points moving away from, and thus it has a direct influence on the selected area of neighborhood. The higher the sigma is, the higher would be the set of local neighbors per each node. This relationship can be observed on the representation of the weight function as a normal Gaussian distribution:

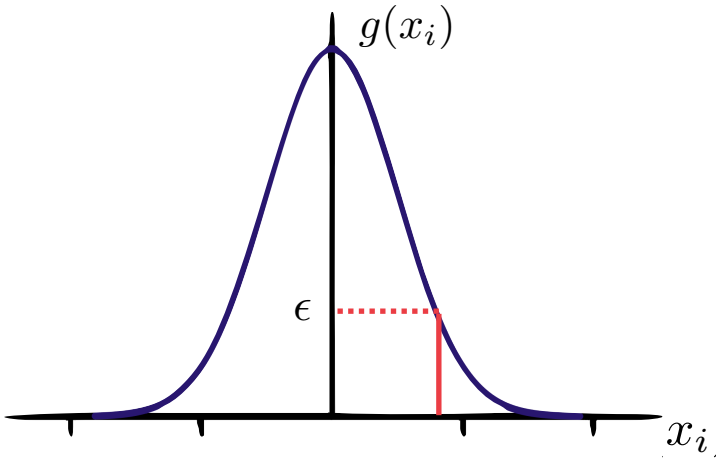

Figure 2.3.1.1.5.2. The function expressed as a Normal Gaussian distribution of weights per a given node i.

The choices of the parameters σ^2 and ϵ are totally correlated with how the nodes are distributed within the geometry. Regarding to this project, the chosen sigma corresponds to the 5 % percent of the average pairwise distances between all the nodes and E=0.1.

These parameters have been chosen by visualizing the weighting functions on the heart surfaces and thus selecting the sigma value that properly satisfies the trade-off between supporting nodes from both the epicardial and endocardial surfaces as well as imposing relative non-large smoothness in the regularization.

2.3.2. L_curve

The L_curve is a widely used visual tool to analyze the ill-condition of inverse problems: it consists of a logarithmic-scaled plot of the norm of the regularization error versus the norm of the residual or fitting error per multiple regularizations applying diverse values of the regularization parameter, λ [25].Thus, this graph displays the trade-off between the minimization of both terms in the regularization: the data fitting and the imposition of a priori knowledge - constraints.

Therefore, the resulting inverse solutions would be more or less constrained according to the variation of the regularization parameter along the L_curve.

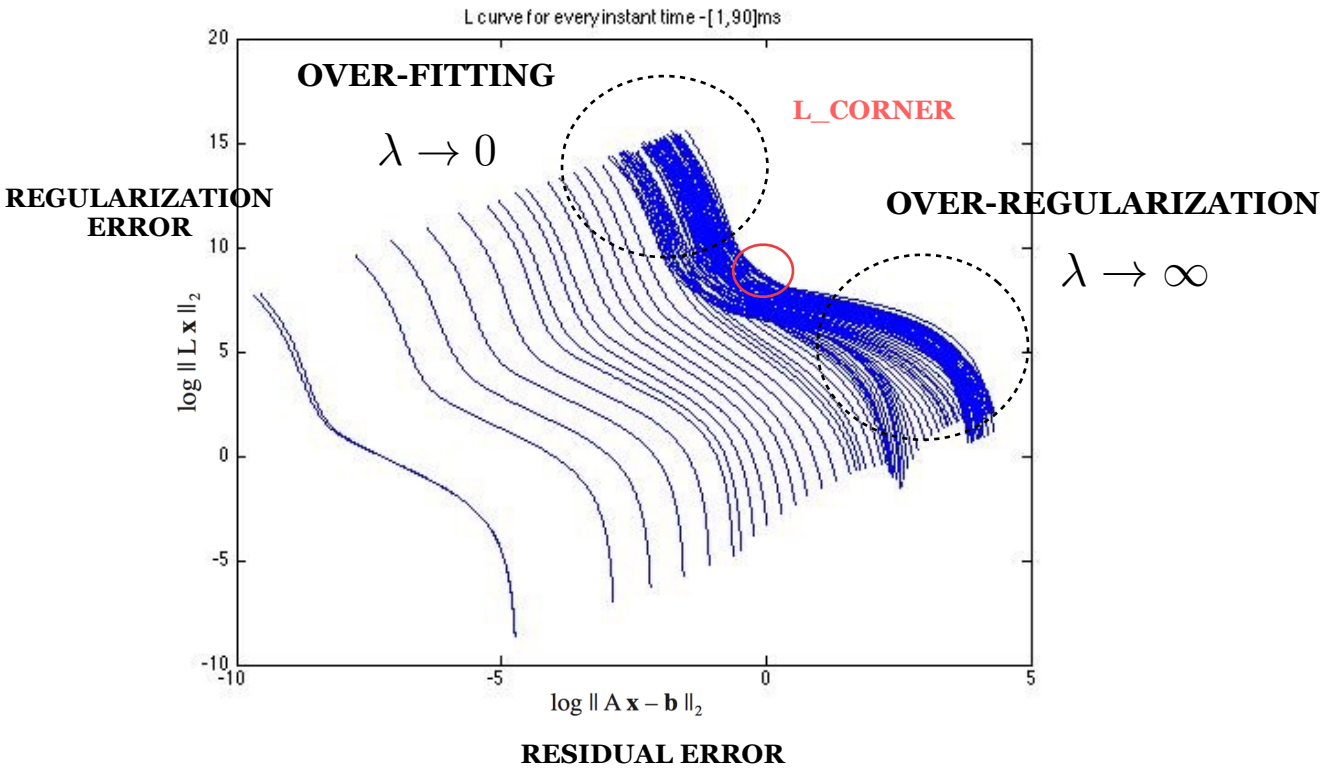

Figure 2.3.2.1. Multiple L_curve plots computed over every time instant of an ECG recording.

As presented in the figure above:

- The vertical part of the curve corresponds to large regularization errors, resulting from the selection of lower lambda values - $\lambda \to 0$ - and thus enforcing the regularization term to be more sensitive to changes.
- On the other hand, the horizontal part of the curve corresponds to large errors in the fitting term as a result from larger values of lambda - $\lambda \to \infty$, which would lead to more sensitivity on the data fitting term.
- When the L_curve is plotted in a logarithmic scale, its shape adopts an L-form, hence its name, presenting a distinct point of inflection between both parts of the curve which is classed as the **L_corner**.

The L-shape of the curve though, is directly related to the a priori choice of the regularization parameters. In consequence, it is fundamental to properly decide the range of these parameters, whose constraints have been previously introduced in the section 2.3.1:

- **First and last samples:**

In this project, this choice would be made by trial and error, i.e by means of evaluating the shape of the L_curve per multiple initial and final points of the regularization parameter and ensuring that the selected ones provide a well-defined L-shape on the curve.

- **Number of samples:**

The L_curve would be sampled in 1000 points, each of which corresponding to a distinct value of the regularization parameter. This number has been carefully chosen to satisfy the trade-off between providing an accurate enough representation of the L_curve to identify the corner and ensuring a relative acceptable computational cost.

- **Criterion in which samples are distributed in the range:**

The lambda values would be equally-spaced in the exponential domain along the range. As previously explained in the section 2.3.1, the regularization parameter is aimed at contrasting the small singular values which cause the ill-condition on the Forward Matrix. And because these singular values change exponentially, the lambda values should also do so.

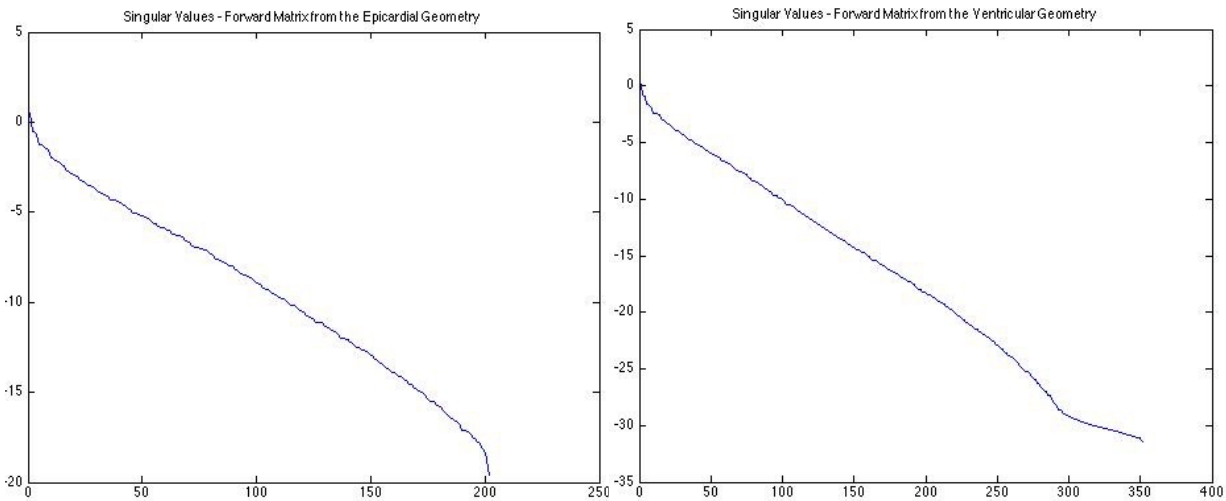

Figure 2.3.2.2. The Singular Values of the Forward Matrices from the Epicardial and the Ventricular Geometries, respectively.

Choosing the optimal regularization parameter to best reconstruct the electrical activity on the heart is a significantly problematic issue, since the necessary regularization to be applied is unknown from a set of remote measurements on the body surface.

However, a well-defined L_curve displays the regularization parameter that best satisfies the trade-off between the data fitting and the imposed regularization, which is presented on the curve as the point where the error in both cases is minimum: **the L_corner**.

2.3.3. Corner Decision

Despite the fact that selecting the corner by eye would be more reliable, the amount of selections to be made discarded this option. This project counts with ECGs from several subjects, which implies that the L_curve is not only computed once per every time instant but also per all the subject-specific measurements.

An alternative manner to solve this problem would be selecting a priori the regularization parameter through the visualization of several L_curves, and applying afterwards the same value all over the time instants. In spite of that, the noisy perturbations introduced in the recordings are not constant over time, and thus the selected regularization parameters should vary in function of them.

Therefore, the corner on the L_curve would be determined per every time instant by means of an algorithm that would automatically detect the maximum curvature of the L_curve - i.e. the inflection point between both parts of the curve.

2.3.3.1. Spline Interpolation

The L_curve is defined by a set of points on the two-dimensional plane, the positions of which are given by the fitting and regularization errors. Then, since it is characterized by this condition, the L_curve is also defined as a tabulated function.

Despite of that, the corner of the L_curve lays on its maximum curvature, and thus to determine it, the L_curve should be approximated as an analytical function.

Spline interpolation is a commonly-used technique that, given a tabulated function, it returns a piecewise polynomial between each pair of tabulated points. Any of these piecewise polynomials is classed as a spline and its coefficients are determined locally but with the imposition of certain conditions that guarantee global smoothness along the interpolated function [26].

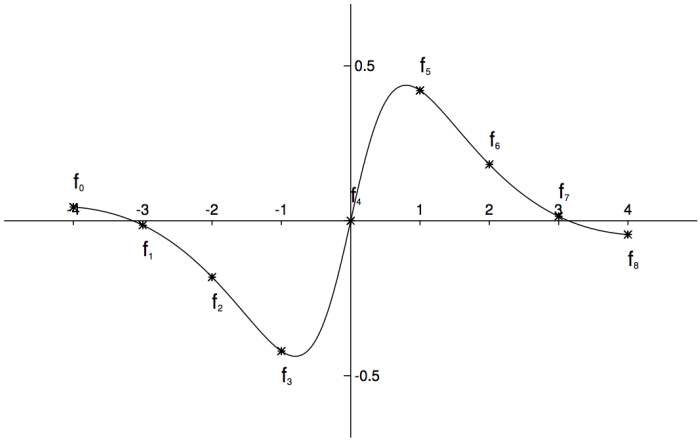

$$f(x) = \begin{cases} p_1(x) & x^{[1]} \le x < x^{[2]} \\ p_2(x) & x^{[2]} \le x < x^{[3]} \\ \vdots & \vdots \\ p_{m-1}(x) & x^{[m-1]} \le x \le x^{[m]} \end{cases}$$

Figure 2.3.3.1. Example of a spline interpolated function f(x) given a set of tabulated points xi and being pi the resulting piecewise polynomials.

Based on the fact that the local curvatures of a cubic function are estimated by its second order derivatives, the L_curve function would be approximated as a cubic spline interpolated function.

Cubic spline interpolation ensures the smoothness of the resulting interpolated function by imposing its continuity through to the second derivative, which is that the second derivatives of the fitted polynomials have to be equal among tabulated points.

Furthermore, the second derivatives of the piecewise polynomials are set to zero at the endpoints as a boundary condition to the interpolated function.

2.3.3.2. Proposed algorithm

This section is aimed at describing the algorithm that has been designed in this project to automatically find the corner of the L_curve.

Instead of considering the L_curve as the input, this algorithm would operate separately over the x-axis and the y-axis of the curve, corresponding to the regularization and fitting errors and labeled as *eta* and *rho* respectively.

Where

$$\eta = log||Rx_\lambda||_2^2 \qquad \rho = log||Ax_\lambda - y||_2^2$$

The various steps involved in the algorithm are presented as follow:

- Eta and rho are defined as tabulated functions on all the range of the regularization parameters that have been used to compute the L_curve. Given that both terms of the regularization are expressed in the logarithmic scale, the regularization parameters of which they are in function would also be in that scale.

- Thereafter, these inputs are characterized as cubic functions, by means of the cubic spline interpolation technique, obtaining from each of them a set of 4th piecewise polynomials.

$$f_\eta(\lambda) = \begin{cases} p_{\eta_1}(\lambda) & \lambda_1 \leq \lambda < \lambda_2 \\ \vdots & \vdots \\ p_{\eta_{k-1}}(\lambda) & \lambda_{k-1} \leq \lambda \leq \lambda_k \end{cases}$$

$$f_\rho(\lambda) = \begin{cases} p_{\rho_1}(\lambda) & \lambda_1 \leq \lambda < \lambda_2 \\ \vdots & \vdots \\ p_{\rho_{k-1}}(\lambda) & \lambda_{k-1} \leq \lambda \leq \lambda_k \end{cases}$$

- Then, the first and the second derivatives for both sets of 4th order piecewise polynomials are computed. To do so, it is applied the differentiation process.

$$\frac{dp_{\eta 1}^K}{d\lambda} \qquad \frac{d^2p_{\eta 1}^K}{d\lambda^2} \qquad \frac{dp_{\rho 1}^K}{d\lambda} \qquad \frac{d^2p_{\rho 1}^K}{d\lambda^2}$$

- The next step is the evaluation of both the first and second derivatives of all the piecewise polynomials on the tabulated points to which they correspond.
- The second derivatives of the tabulated function given by the L_curve are calculated through the following mathematical equation, which have been extracted from the software code of the SCIRun program [27]:

$$\frac{d^2p_{Lcurve_i}}{d\lambda^2} = \frac{\frac{dp_{\eta_i}}{d\lambda}\frac{d^2p_{\rho_i}}{d\lambda^2} - \frac{d^2p_{\eta_i}}{d\lambda^2}\frac{dp_{\rho_i}}{d\lambda}}{\frac{d^2p_{\rho_i}}{d\lambda^2} + \frac{d^2p_{\eta_i}}{d\lambda^2}}$$

Where every computation of the first and second derivative of the eta and rho piecewise polynomials result as a second derivative of the L_curve.

- Lastly, the algorithm finds the absolute maximum value of these second derivatives of the L_curve. Its output is the position of this maximum on the L_curve, corresponding to the position of the ***optimal*** **regularization parameter** λ_{max} as well.

$$\max_i(|\frac{d^2p_{Lcurve_i}}{d\lambda^2}|) \longrightarrow \lambda_{max}$$

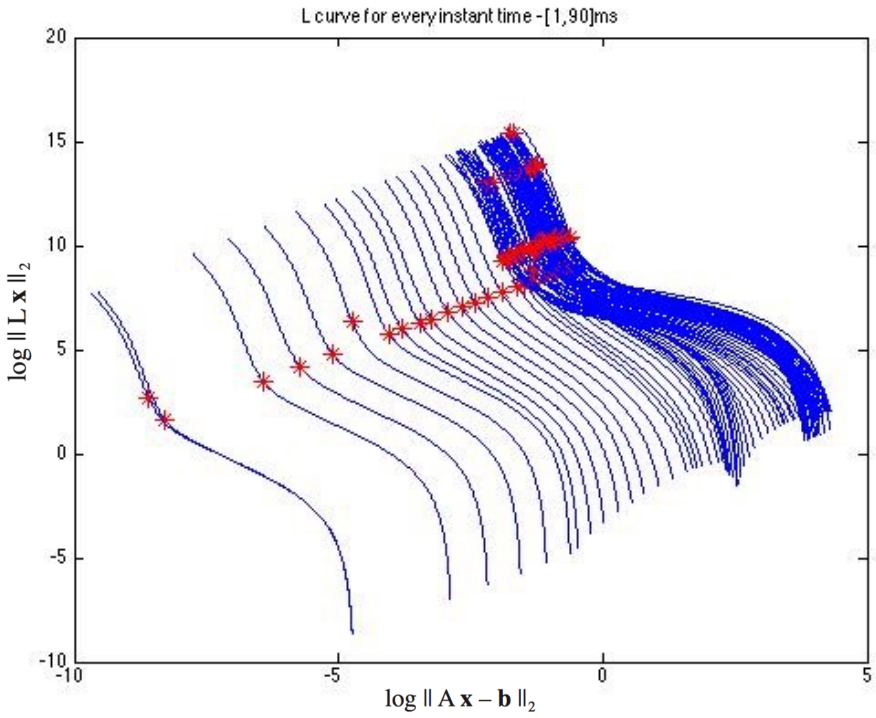

Figure 2.3.3.2. Multiple L_curve plots displaying the performance of the proposed algorithm given that the red points correspond to the automatically found L_corners.

2.3.4. Singular Value Decomposition

The Singular Value Decomposition is a broadly recognized algebraic theorem that has many applications in signal processing and inverse problems. For this reason, in this section its main basics would be introduced.

This theorem states that given a rectangular *n x p* matrix A, it can be decomposed into a factorization such that:

$$\mathbf{A}_{nxp} = \mathbf{U}_{nxn} * \mathbf{S}_{nxp} * \mathbf{V}^{\mathbf{T}}_{pxp}$$

Where

- $\mathbf{U}_{nxn}$ and $\mathbf{VT}_{pxp}$ are real or complex unitary matrices
- $\mathbf{S}_{nxp}$ is a non-negative real diagonal matrix of the same dimensions as $\mathbf{A}_{nxp}$

And $\mathbf{U}_{nxn}$ and $\mathbf{VT}_{pxp}$ are defined such that:

- $U^T U = I_{nxn}$
- $V^T V = I_{pxp}$

The diagonal values of S are commonly named as the singular values of the matrix A, whereas the columns of U and the rows of V^T are classed as the left-singular and right-singular vectors of A [28]. In overall, the Singular Vector Decomposition provides a representation of the data in a coordinate system where the covariance matrix of A is diagonal.

When A is a *nxn* square matrix, the unitary matrices U and VT become nxn square matrices as well, and thus the decomposition of A can be divided into the transformations of rotation, scaling and rotation, as it is expressed in the figure below. This particular case is known as eigenvector decomposition, since the columns and rows of the matrices U and V correspond to the eigenvectors of A.

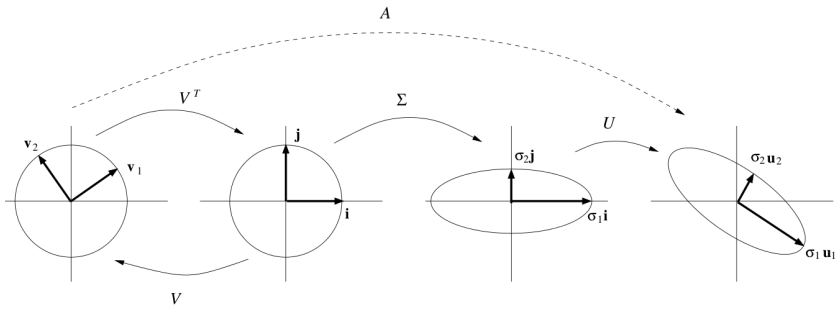

Figure 2.3.4. Visualization of the Singular Value Decomposition of a square and symmetric matrix A [29].

2.3.5. Proposed regularization by using SVD. Hansen approach

Estimating inverse solutions by means of the Tikhonov regularization requires a considerable computational costs, as the minimization problem is solved all over the range of regularization parameters, which enables a posteriori the evaluation of the L_curve to properly choose the corner and thus reconstructing the potential distribution on the heart.

By decomposing the Forward Matrix A through SVD, it is possible to estimate the terms || x || and ||Ax-b|| without solving the regularization, so that the L_curve and its corresponding corner can be rapidly computed and the minimization problem can be uniquely solved per the selected regularization parameter.

In this section, it will be proved through a mathematical demonstration that applying SVD leads to a simple equation which solves both terms of the Tikhonov regularization and thus reduces extensively the computational cost of the L_curve. This method has been proposed by the author P.C. Hansen [30].

From the developed minimization problem of the Tikhonov Regularization then, it is deduced that:

$$x = (A^T A + \lambda I)^{-1} A^T y \qquad A = LSR^\top$$

$$x = (RS^2R^\top + \lambda I)^{-1}(RSL^\top y)$$

$$x = (R(S^2 + \lambda I)R^\top)^{-1} RSL^\top y$$

$$x = RS_nL^\top y \quad \text{where} \quad S_n = (S^2 + \lambda I)^{-1} S$$

$$Ax - y = LSR^\top(RS_nL^\top y) - y = LSS_nL^\top y - y$$
$$Ax - y = (LSS_nL^\top - I)y = (L(SS_n - I)L^\top)y = LS_fL^\top y$$
$$\text{where} \quad S_f = SS_n - I$$

Accordingly to the expressions above, both terms of the Tikhonov regularization can be now expressed such that:

$$||x||_2^2 = x^\top x = (RS_nL^\top y)^\top(RS_nL^\top y) = y^\top LS_n^2L^\top y$$
$$||Ax - y||_2^2 = y^\top LS_f^2L^\top y$$

Which can also be expressed as the following equations, being *K* the range of λ values over which the L_curve is computed:

$$||x||_2^2 = \sum_{i=1}^{K} S_{n_{ij}}^2 z_i^2$$
$$||Ax - y||_2^2 = \sum_{i=1}^{K} S_{f_{ij}}^2 z_i^2$$

where

$$z = L^\top y$$
$$S_{n_{ij}} = \frac{S_{ij}}{S_{ij}^2 + \lambda_i}$$
$$S_{f_{ij}} = \frac{-\lambda_i}{S_{ij}^2 + \lambda_i}$$

Therefore, the process to obtain the reconstructed inverse solutions, using the Hansen approach as the regularization method, is described in the scheme below:

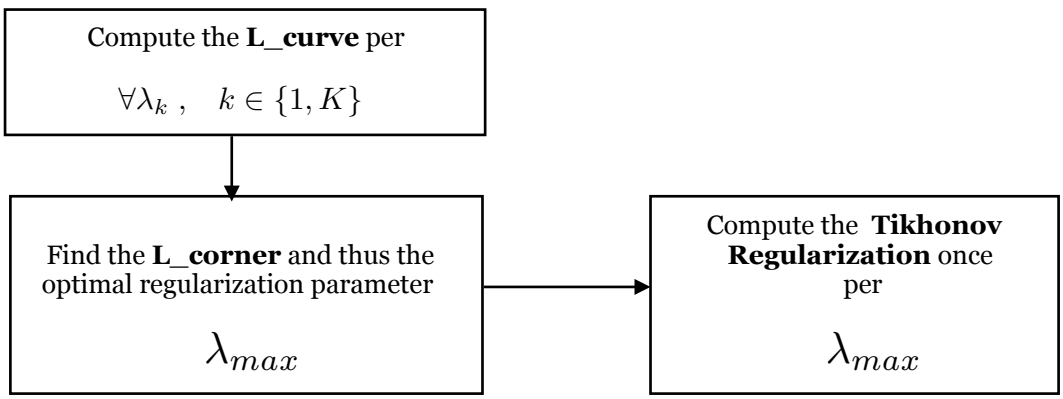

Figure 2.3.5.1. Hansen approach Block diagram.

Standard Tikhonov Regularization method

Hansen approach

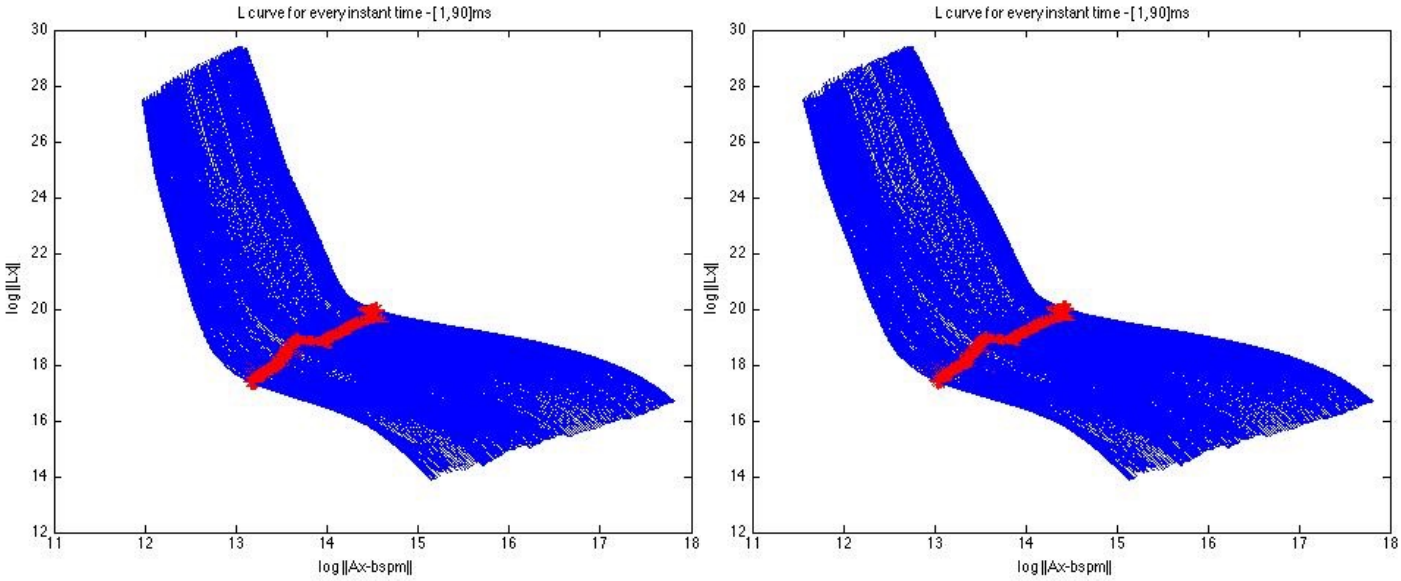

Figure 2.3.5.2. L_curve plots by the use of the Tikhonov regularization per multiple lambda values and the Hansen approach, respectively. It is displayed above that the difference between both regularization methods is almost negligible.

3. The dynamic model. An extension of the Tikhonov Regularization.

In the previous sections, the Tikhonov regularization and its respective type variants assumed prior information in order to obtain spatially smooth inverse solutions throughout the heart mesh with the balance of the electrical activation wavefront to be noticeable. Given that the body surface measurements are exposed to unavoidable noise which causes small perturbations in the ECGs, a temporal model would be proposed in this section to provide continuity and smoothness along the whole time sequence of the recorded data samples.

This temporal model is based on defining a low-order parametrized approximation, a curve, in a high-dimensional space, where its dimension corresponds to the number of electrodes that has been used to record the measurements. To do so, the entire set of multi-electrode body surface measurements are fitted non-linearly by means of an adaptive piecewise cubic spline parametrized by a set of time-independent points, classed as knot points.

Finally, to obtain the resulting inverse solutions, the approximated signal represented through the estimated spline coefficients is placed in the time domain.

3.1. Temporal Multichannel Curve Approximation

3.1.1. Definition. Knot points and pseudo-time manifold

The use of knot points instead of time samples is due to the proper fitting of the parametrized approximation, since it requires an **equally-spaced dynamic range** and the time samples distribution is non-uniform. Therefore, the fitting is non-linear - it does not depend on time - and the curve is in function of these pseudo-time parameters placed in the high-dimensional space and representing the position along the curve.

The function which relates both the time and the pseudo-time manifolds is linear, enabling *warping* or *un-warping* the curve such that $\theta: \mathbb{R} \to \mathbb{R} \mid t \to \theta(t)$:

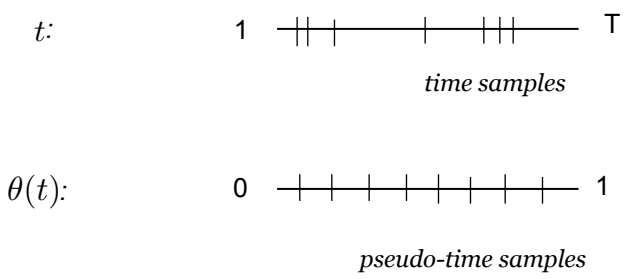

The choice of the number of knot points and their location controls the performance of the spline fitting. In this project, the number of knot points would be 12 and its choice has been done to satisfy the trade-off between data fidelity and stability of the solutions. The derivatives of the approximated curve at its end-points are returned such that the curve has also two degrees of freedom.

Let's consider every multi-electrode body surface measurement as a point $Y_i = [Y_1 \quad \cdots \quad Y_N]$ where $Y_i \in \mathbb{R}^N$ and N is the number of electrodes. These points are modeled as trajectories on the manifold, ignoring the rate in which the set of points traverses the manifold, and thus only approximating the set of points which are traversed by the signal.

As represented in the expression below, the set C is composed by a given set of points *x*, such that, $x = c(\theta)$ considering *x* as the possible points along the approximated curve c, and θ as the pseudo-time manifold defined arbitrarily in the range: [0,1].

$$\mathcal{C} = \{x \mid \exists \theta \in [0,1] \; s.t. \; x = c(\theta)\}.$$

The approximated curve is parametrized by a B-spline fitting described as follows:

$$c(\theta) = \sum_{i=1}^{K} \alpha_i B_i(\theta)$$

Where α_i. are the spline coefficients and the $B_i(\theta)$ the respective basis functions over θ.

3.1.2. Iterative algorithm

This algorithm is aimed at finding a curve c such that the difference between the real data samples from the body surface measurements and the projection of these samples onto the set C given the curve c is minimal, in order that the curve c approximates to the maximum extent to the data samples.

$$\min_{\theta,k} ||Y - proj(Y, c(\theta(t)))||_2^2$$

The curve c is approximated by a finite dimensional parameterization by means of the piecewise cubic spline interpolation technique and the fitting is based on a number of knot points placed at unknown locations. There are two more unknown conditions which correspond to the first order derivatives of the curve at the first and end knot points.

The problem is approached by the use of the optimization algorithm Expectation and Maximization, in which the minimization least-square problem is solved iteratively. The Expectation part consists of approximating the curve and projecting the data samples to this curve whereas the Maximization part corresponds to the update of the spline parameters.

Once this iterative algorithm comes to the minimal solution, the final approximated curve projection results as a filtered version of the original signal, as it is expressed below:

$$\tilde{Y} = proj(Y, c(\theta(t)))$$

Finally, to provide the temporal regularization for the heart surface potentials, it is considered the relationship below:

$$Y \approx K_Y P = K_Y P_1 P_2$$

Where

- Y is the approximated curve defined over the time.
- Ky is a matrix composed by the coefficients of the knot points and the spline derivatives, whose function is to map the set of filtered body surface potentials to the actual time manifold.
- P1 is the spline interpolation in the given pseudo-time parameters.
- P2 is the mapping function from the pseudo-time to the time manifold.

Since the forward problem is quasi-static, the same warping function and knot locations are assumed such that they would provide an acceptable basis to approximate the unknown heart surface potentials. Thus, classing X as the heart surface potentials and P as the same warping matrix, the inverse problem is solved by:

$$K_x : X \approx K_x P$$

And when assuming this forward relationship:

$$Y \approx K_Y P = A K_x P$$
$$K_Y = A K_x$$

Therefore, the inverse problem is to estimate *Kx* and it is solved by the Tikhonov regularization per each column separately, choosing the appropriate regularization parameter by the use of the L_curve technique and thus finding the L_corner, as it has been explained in the previous sections 2.3.1, 2.3.2, and 2.3.3.

The final heart surface potentials are obtained through the earlier warping function:

$$X = K_x P$$

4. The Data. Pacing site localization

4.1. Data Description

In the conduction of this project, the data has been provided from the Department of Medicine and Mathematics of the Dalhousie University, Canada.

This data is based on body surface potential measurements (ECGs) recorded from 52 subject-specific cases including one or a pair of QRS complex waves. These data files are composed by:

- **RAW data:** where the data files correspond to body surface potentials directly recorded from the Electrocardiogram technique.
- **Interpolated Data:** where the data files have been previously pre-processed by the use of the interpolation technique - i.e. assuming potential values in the nodes of the torso mesh in-between the physical locations of the actual electrodes.

These ECGs files have been extracted from patients with distinct cardiac diseases such as Right Bundle Branch Block (RBBB), Left Bundle Branch Block(LBBB) or Ventricular Tachycardia (VT).

The RBBB and the LBBB are cardiac diseases where the activation of the right or left ventricle, respectively, is delayed whereas the other ventricle is activated normally.

The VT is classed as the disease in which the ventricular activation is abnormal, either by delays, tissue blocks or scars on the myocardium.

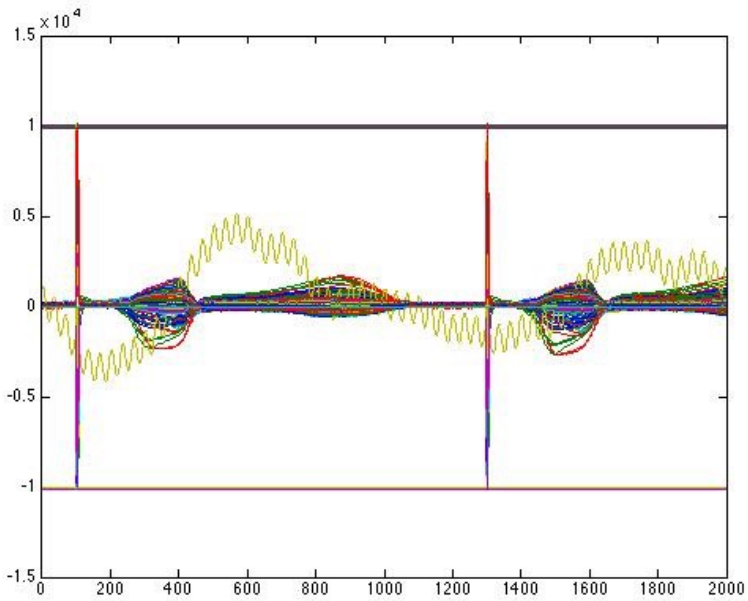

Figure 4.1.1. Example of a RAW Data file containing the BSPM measurements directly recorded from the Electrocardiogram.

Case	W-onset	QRSon	Remark	Description
C1	5000	225	SR	BASELINE SR MAGNET OFF
C2	0	115	PACED	PACED RHYTHM- VAGAL
C3	600	115	PACED	PACED CL = 1000 ms
C4	6000	50	VT1	VT1 CL = 260 ms
C5	7000	30	VF	VF (7000-9500 ms); DEFIB @ 200J
C6	3000	30	VT2	VT2; RBBB morphology; CL = 240 ms
C7	9000	0	VF	VF (9000-15000 ms); DEFIB 200J
C8	0	0	JUNK	DELETE
C9	1850	160	M1 C13	CL = 600 ms; DELAY = 90 ms
C10	2100	120	M1 C18	PACE; PHRENIC CAPTURE
C11	0	0	JUNK	DELETE
C12	400	115	M1 C19	PACE
C13	100	80	M1 C22	PACE FRACTIONATED
C14	400	120	M1 C24	PACE; LBBB morphology
C15	500	80	M1 C30	M1 C30 PACE
C16	1000	110	M1 C32	M1 C32 PACE PROBABLY RV
C17	500	95	M1 C36	M1 C36 PACE -POSITIVE LEAD 1
C18	100	120	M1 C40	M1 C40
C19	500	110	M1 C41	PHRENIC STIMULATION
C20	520	185	M1 C46	RBBB morphology; DELAY = 80 ms
C21	100	220	M1 C48	PACE: DELAY 130 ms
C22	320	155	M1 C50	PACE; DELAY 80 ms
C23	520	120	M1 C55	PACE -PHRENIC capture
C24	220	110	M1 C58	M1 C58 PACE (VT2 MATCH)
C25	520	70	M1 C62	M1 C62 PACE
C26	600	150	M1 C69	M1 C69 PACE; DELAY = 50 ms
C27	80	115	M1 C74	M1 C74 PACE
C28	400	80	M1 C86	M1 C86 PACE
C29	60	65	M1 C100	M1 C100 PACE-RV 2/3 APICAL
C30	3000	135	M1 C150	ALTERNATING; DELAY = 75 ms
C31	3000	180	M1 C158	PACE 10/12 FOR VT2; DELAY = 80 ms
C32	2080	175	M1 C167	M1 C167 PACE; DELAY = 75 ms

Case	W-onset	QRSon	Remark	Description
C33	5000	175	M1 C170	M1 C170 PACE; DELAY = 55 ms
C34	550	160	M1 C189	10/12 FOR VT2; DELAY = 60 ms
C35	450	100	M2 C34	PACE FROM ENDOCARDIUM- 9/12 VT1
C36	120	100	VT	ATH INDUCED VT (RBBB); CL = 570 ms
C37	4000	115	M2 C98	CARDIAL PACE@400-MID POSTERIOR
C38	280	65	M2 C99	M2 C99 PACE
C39	200	140	M2 C101	M2 C101 PACE @400
C40	0	60	M2 C106	M2 C106 PACE NOT BAD VT1
C41	250	90	M2 C113	M2 C113 PACE
C42	120	110	M2 C114	M2 C114 PACE
C43	200	105	M2 C115	M2 C115 PACE
C44	4040	100	M2 C116	M2 C116 PACE; CL = 400 ms
C45	0	65	M2 C117	M2 C117 PACE
C46	240	70	M2 C118	M2 C118 PACE-DIAPHRAGM CAPTURE
C47	120	65	M2 C119	C119 PACE INFERO POSTERIOR APEX
C48	200	135	M2 C121	M2 C121 PACE APICAL SEPTUM
C49	200	90	M2 C122	M2 C122 PACE LVOT
C50	10000	70	VT1	VT1 RE-INDUCED; CL = 260 ms
C51	10000	90	VT	VT-Vflutter (CL = 290 ms)- DEFIB 200 J
C52	14000	0	VT	VT; CL = 240 ms

Table 4.1.2. Data description provided by the Dalhousie University, Canada.

4.2. Preprocessing of the Data

Considering that the RAW data is directly given from the ECG recordings, it requires previous preprocessing steps before the reconstruction of the inverse solutions.

The data preprocessing that has been carried out in this project is presented as follows:

- **Bad Leads Removal:** the Dalhousie University also provided a particular file containing the ill-conditioned electrodes causing noisy pics in the resulting recorded signals. This file was loaded and these electrodes introducing noise were removed from the ECGs measurements.
- **Filtering:** These signals are composed by one or a pair of QRS complex waves, such that every body surface potential measurement was filtered in order to extract the very first QRS wave of the signal.

4.2.1. BSPM Filtering

In this section it is explained the filtering process to extract the first QRS complex wave of the set of RAW data files containing the body surface potential measurements.

The multiple steps conforming this process are the following ones:

- The averaged energy of all the multi-electrode signals placed in the nodes of the torso mesh is computed over the entire time sequence of the ECG recording.
- This averaged energy is evaluated and any pic exceeding a given threshold is removed from the RAW data file.
- The initial and ending positions of the first QRS complex are extracted by means of estimating the signal gradient from the energy function. The starting point is detected by the first change in the slope of the function whereas the ending point is identified by establishing a fixed range of the QRS wave from the starting point.

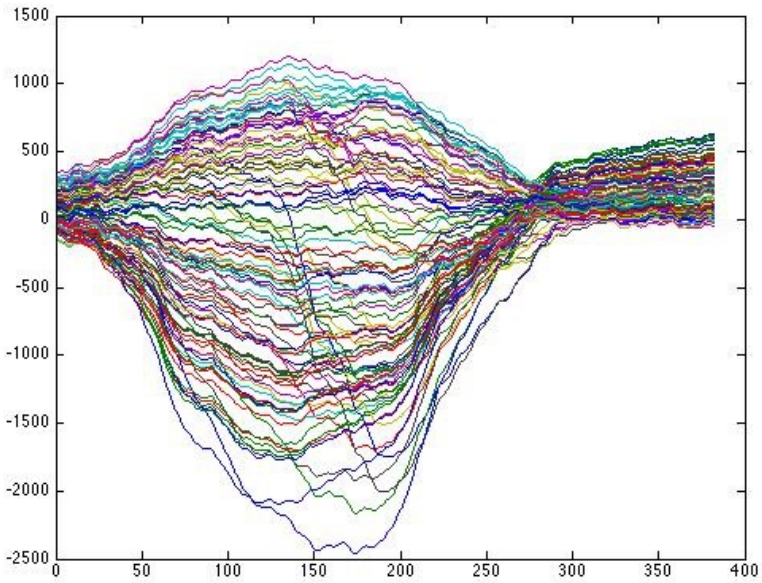

Figure 4.1.1. Example of a resulting RAW Data file after the Preprocessing Block.

4.3. Geometries generation

The geometries employed in this project have been extracted from images obtained by Magnetic Resonance Imaging (MRI) and Computed Tomography (CT) scans.

These employed geometries are described as follows:

- **Torso Surface Geometry**: this geometry is composed by 352 nodes and represents the mesh of the torso from a specific subject.

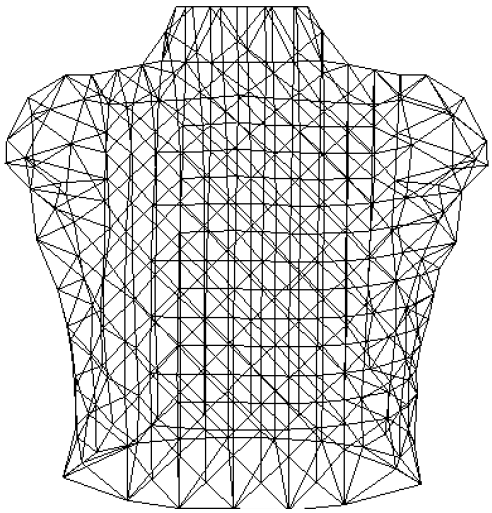

Figure 4.3.1. Torso Surface Geometry.

- **Heart Surface Geometries**: these geometries represent the mesh of the heart from a specific subject.
  - **Epicardial Geometry**: this geometry is composed by 202 nodes and represents the outer surface mesh of the heart - i.e. its nodes define the epicardial layer of the heart mesh. The boundary of this geometry is given by a flat surface covering the top of the heart mesh, as the model of the bioelectric source assumes this source to be located in an enclosed volume.

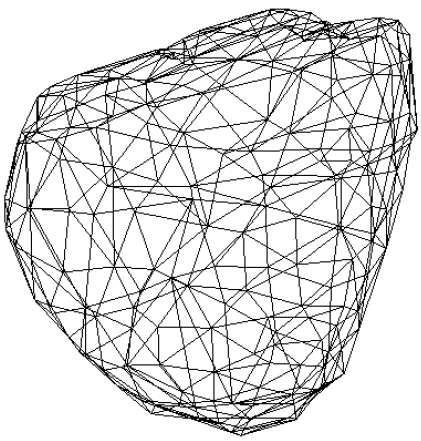

Figure 4.3.2. Epicardial Surface Geometry.

- **Ventricular Geometry**: this geometry is composed by 490 nodes and represents the outer and inner surface mesh of the heart - i.e. its nodes define both the endocardial and epicardial layers of the heart mesh.

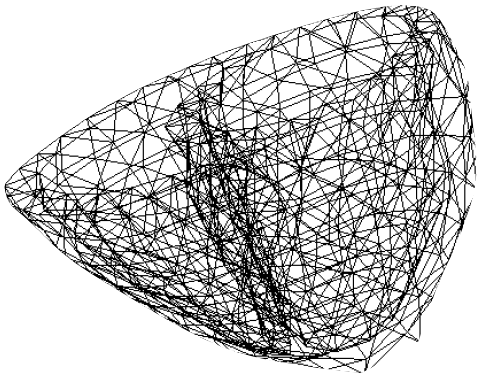

Figure 4.3.2. Ventricular Surface Geometry.

4.4. Catheter interventions

Catheter ablation is an invasive procedure that consists of inserting a catheter - a thin, flexible tube - into the heart and delivering energy through it in order to remove or terminate faulty electrical pathways - ectopic beats - from areas of the heart that cause abnormal heart rhythms and thus are prone to develop cardiac arrhythmias such as atrial fibrillation, atrial flutter, supra-ventricular tachycardias (SVT) and Wolff-Parkinson-White syndrome.

In the practice of this procedure for treating cardiac arrhythmias, the locations in the heart from which the ectopic beats suddenly appear are observed and thus they can be possibly captured by the medical system classed as **cardiac catheterization (CARTO)**.

Therefore, these CARTO points, also commonly named as the **Pacing Site locations,** are medically used by reason of providing the positions in the heart where the electrical activation wavefront arises.

4.4.1. Ground-truth

The ground-truth is a well-known term in research meaning the absolute truth in terms of the accuracy of a given technique or method over training sets.

In this project, the ground-truth refers to a set of files, which have been also provided from the Dalhousie University, containing the pacing site locations earlier extracted from CARTO points, per 20 subject-specific cases corresponding to the cases previously described in the section 4.1, and by which the resulting inverse solutions are obtained.

Regarding to this project then, the ground-truth is a set of 3 dimensional coordinates that would be used to evaluate the results and consequently, the performance of the diverse regularization methods.

4.5. Heart earliest activation location

In order to evaluate the performance of the regularization methods, a comparison between the resulting inverse solutions and the previously mentioned ground-truth would be conducted. Hence, given that this ground-truth describes the pacing site locations per various subject-specific cases, it is required to design an algorithm that detects the location in the heart mesh of the earliest electrical activation per each resulting solution.

The heart surface potential distributions are represented by means of **isochronal maps**, such that negative potential values are mapped into cold color tones and thus positive potential values into warm color tones.

Accordingly, the basic goal of the detection algorithm is to seek in time the earliest potential increase over the entire set of nodes in the heart mesh and return its position.

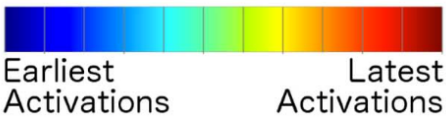

Figure 4.5. Isochronal color bar in relation to the electrical activation.

The detection of the electrical wavefront would not be straight-forward as the resulting inverse solutions have been regularized to behave smoothly in space and time. In consequence, the exact location where this electrical wavefront is first noticed would not be showed clearly and evidently in the results.

By cause of that, two distinct detection algorithms would be proposed in the following sections, each of which focused on a particular method to measure this earliest potential increase: the computation of the derivatives or the overall divergence per every node in the heart mesh throughout the time sequence.

Once the pacing sites per all the subject-specific cases would have been detected, the resulting location of the earliest activation from the reconstructed inverse solutions and the respective ground-truth coordinates mapped into the heart mesh would be compared by means of the computation of the **euclidean distance measure**.

$$d(p,q) = \sqrt{\sum_{i=1}^{3}(p_i - q_i)^2}$$

4.5.1. Proposed algorithm using temporal negative derivative

As mentioned in the section above, the reconstructed inverse potentials have been obtained by regularizations assuming smoothness spatially and temporally. For this reason, the electrical wavefront can not be directly detected by an interpolation or a simple search, despite the fact that it can be visually observed through isochronal maps, and thus the estimated earliest activation locations require an additional smoothing step.

This proposed algorithm consists of estimating the Activation Times τ per every node in the heart mesh considering these instants as the time samples with the larger negative derivative over the entire time sequence. Thereafter, the dominant electrical propagation pattern τ_D is extracted from these activation times and their spatial distribution is smoothen through a Laplacian matrix L_{τ_D} as follows:

$$\min_{\tau_D} ||\tau - \tau_D||_2^2 + \gamma||L_{\tau_D}||$$

Where the parameter γ controls the amount of smoothness of the resulting propagation pattern.

This minimization problem is solved repeatedly over a wide range of the parameter γ and afterwards both terms are plotted by means of the L_curve a posteriori technique.

The earliest activated node in the heart mesh - i.e. the pacing site - would correspond to the node with the minimum element of the Activation Times vector, which has been obtained regularizing over the parameter γ extracted from the automated L_corner algorithm previously explained in the section 2.3.3.

4.5.2. Proposed algorithm using radial divergence

The ectopic foci or abnormal pacing sites can be characterized by analyzing the electrical vector fields of the assumed bioelectric source through the divergence computation [31]. Accordingly, this mathematical operator measures the density of the outward flux of the electrical vector fields from an enclosed volume given a particular point.

On the pacing site nodes there would be an abrupt potential change in time, and thus its electrical fields would be larger in magnitude causing the **divergence function** at that point to be **maximum**. Therefore, considering the electrical vector fields as unit vectors, the calculation of the divergence as a scalar-valued function of these 2 dimensional electrical vectors over each directional component *Fx,y,z* in the Cartesian space would be expressed as follows:

$$\nabla V_p = \frac{\partial V_{px}}{\partial x} + \frac{\partial V_{py}}{\partial y} + \frac{\partial V_{pz}}{\partial z}$$

Such that the pacing site would be placed at the node *p* where the divergence function equals to $\max(\nabla V_p)$

From the formulation above it can be deduced that the divergence can be also determined by summing the diagonal of the volumetric hessian estimation from the spatial function given by every node in the heart mesh.

Although the divergence function is computed over all the time instants and all the nodes composing the heart mesh, the pacing site has not been chosen as the node where the divergence is maximum per the entire matrix, but as the node where the magnitude of the electrical wavefront - i.e. the divergence - is maximum for the longest period of time. To do so, the divergence values are summed over all the time instants per each of the nodes in the heart mesh and consequently the pacing site would correspond to the node where this summation is maximal.

The electrical vector fields can be represented by means of the spatial gradient estimation computed over the function given by the heart surface mesh, as it is displayed in the figures below:

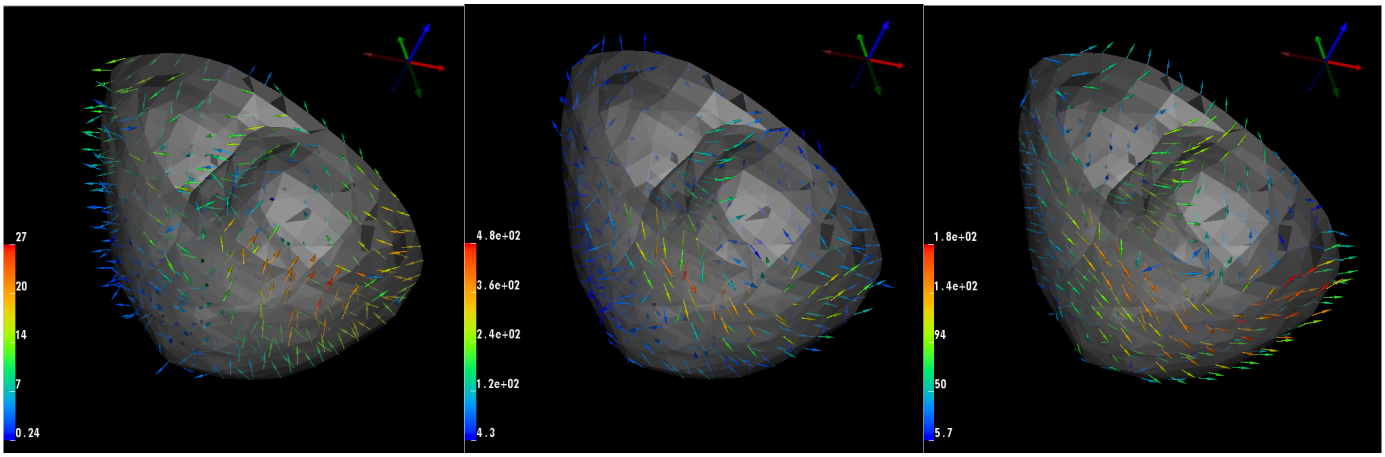

Figure 4.5.2. Gradient maps per three distinct time instants of a given Data file.

4.6. Final pipeline block diagram

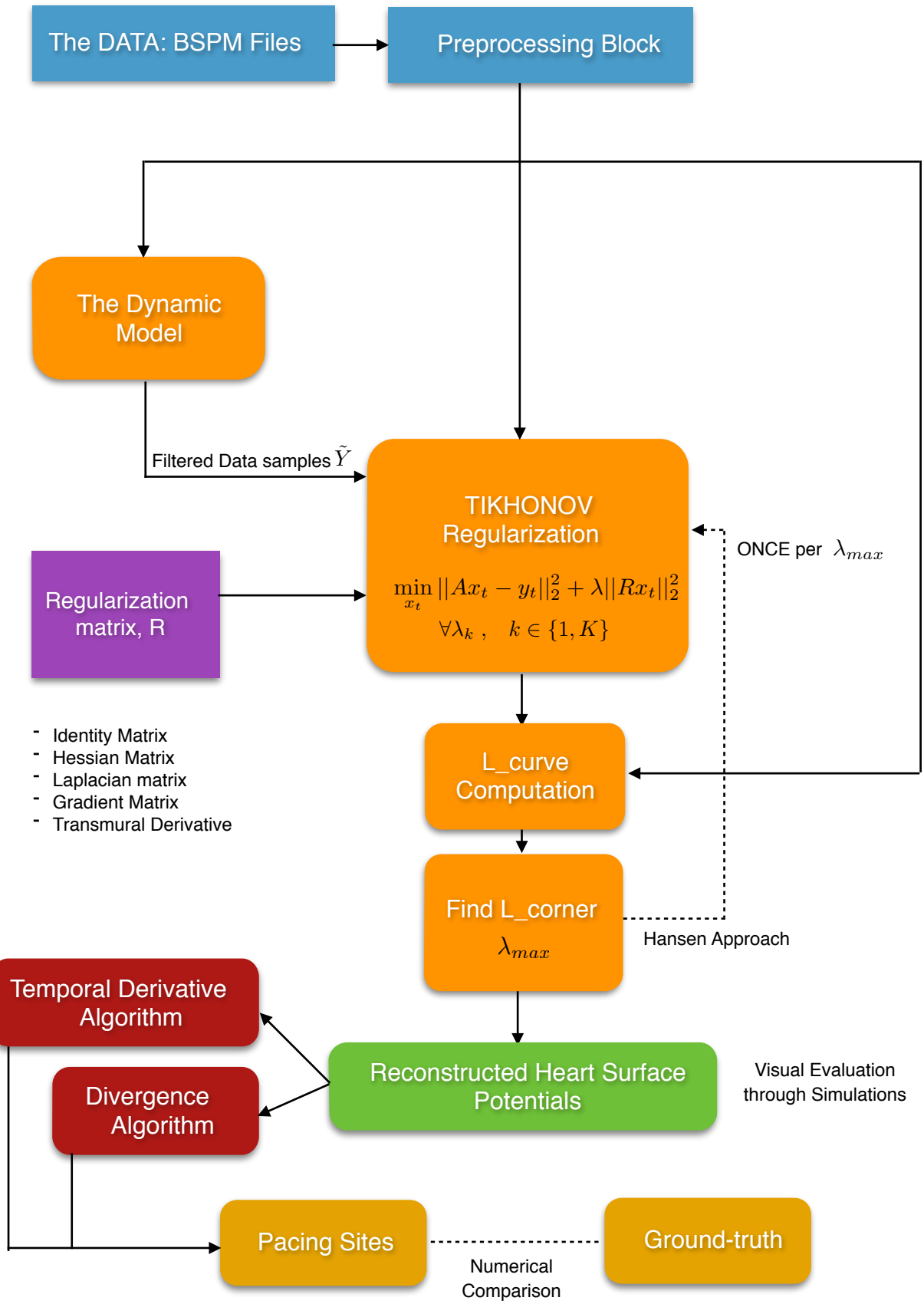

5. Results. Experiments

5.1. Reconstructed potentials on the Epicardial geometry

5.1.1. Simulations. Results per Regularization Matrix

Case C_46: RBBB morphology; DELAY = 80 ms

Pacing Site: # Node 73

RAW Data

IDENTITY REGULARIZATION

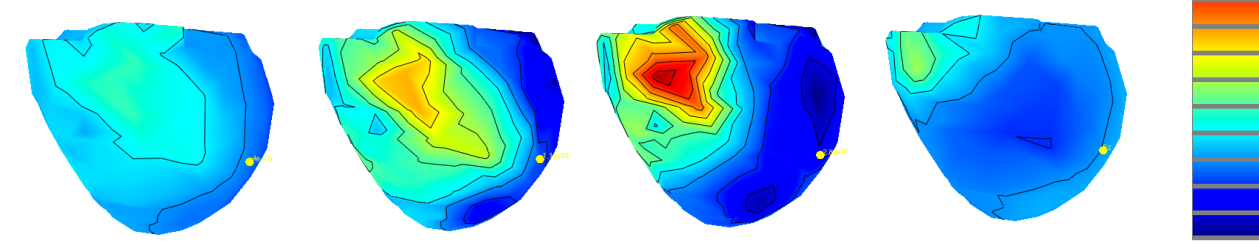

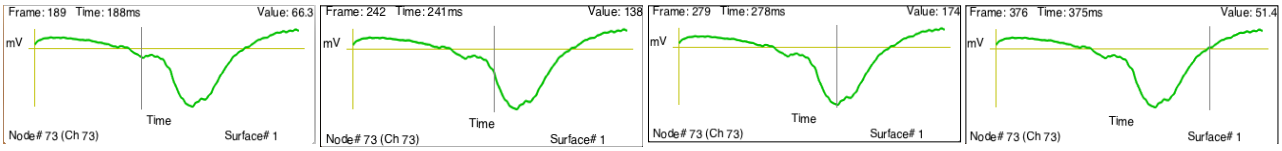

HESSIAN REGULARIZATION

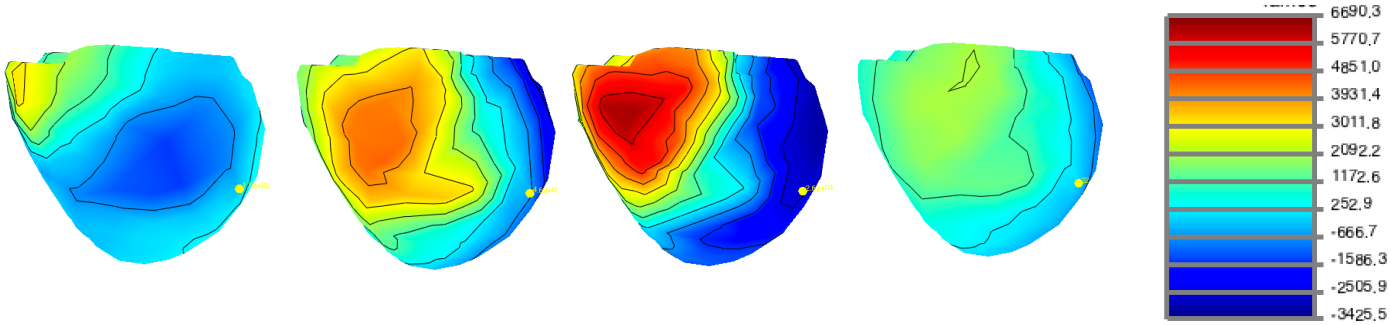

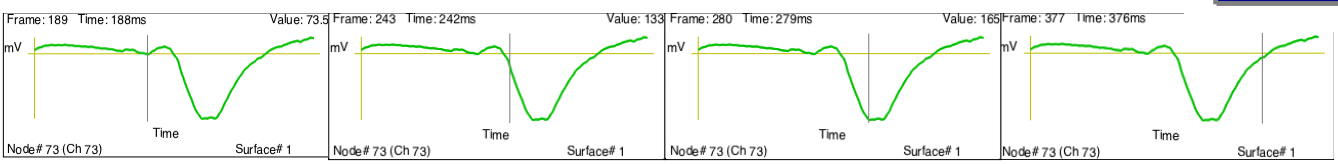

LAPLACIAN REGULARIZATION

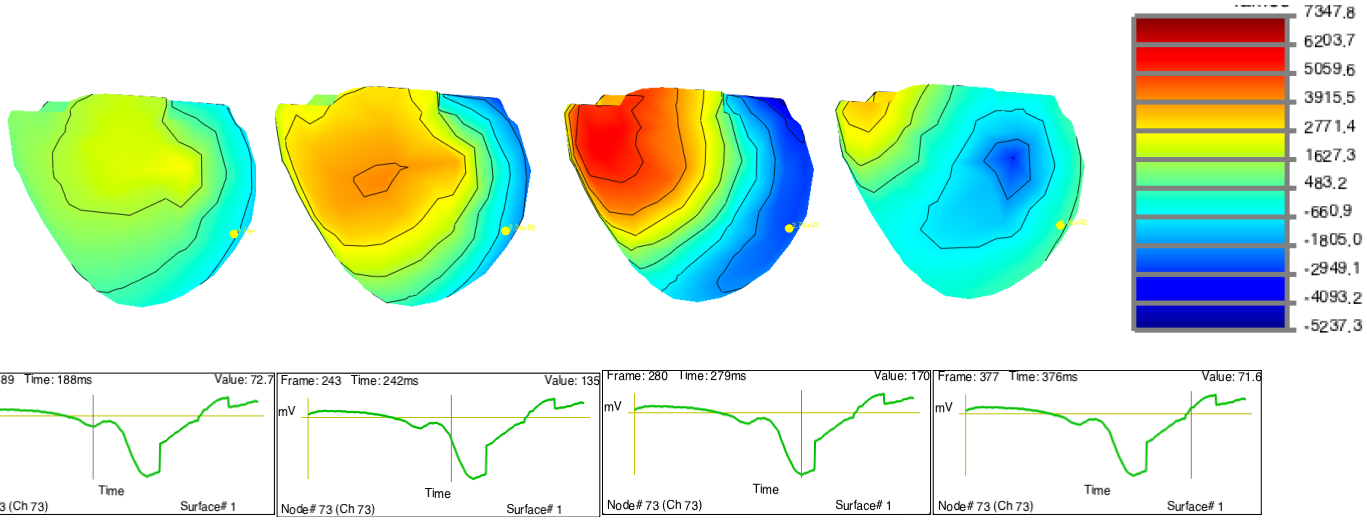

GRADIENT REGULARIZATION

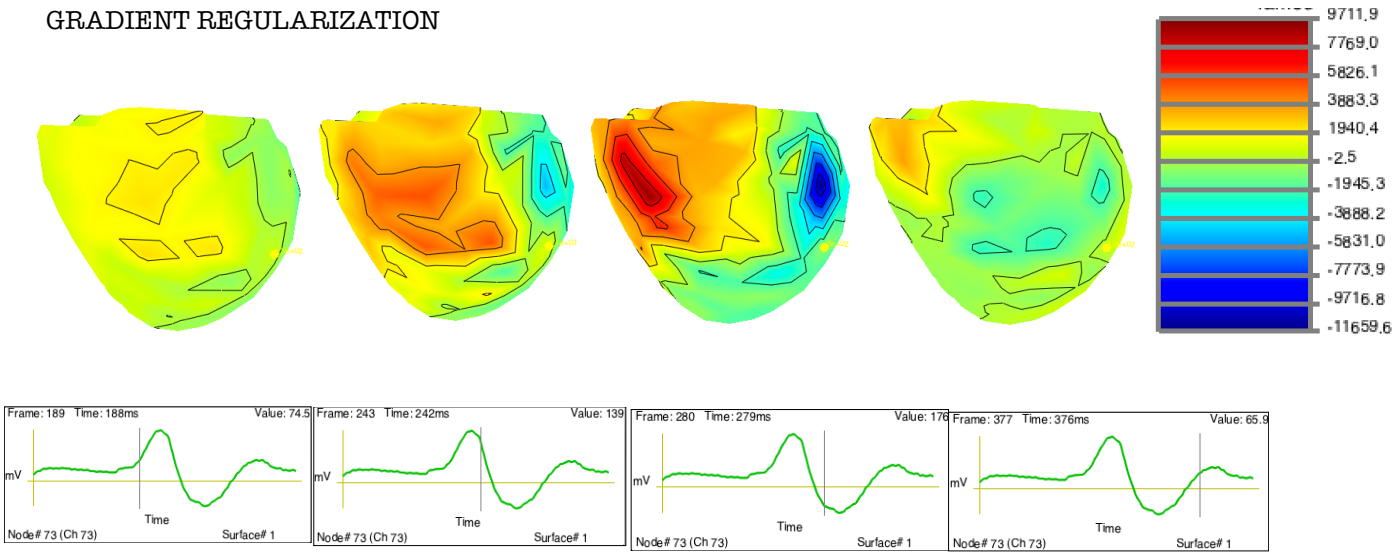

Case C_58: PACE (VT2 MATCH)

Pacing Site: # Node 68

RAW Data

IDENTITY REGULARIZATION

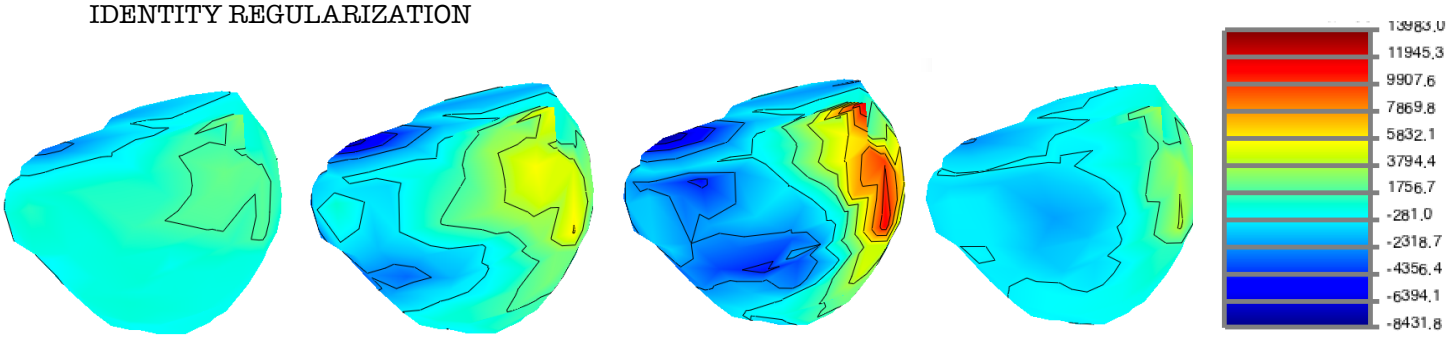

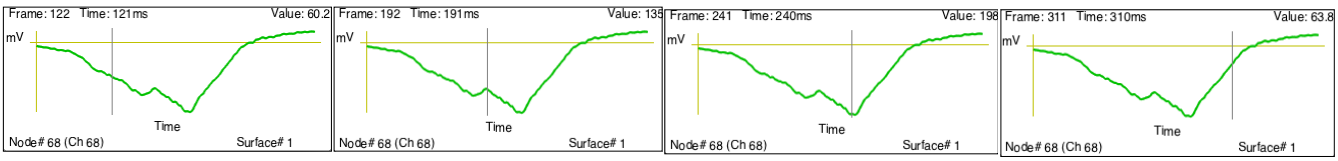

HESSIAN REGULARIZATION

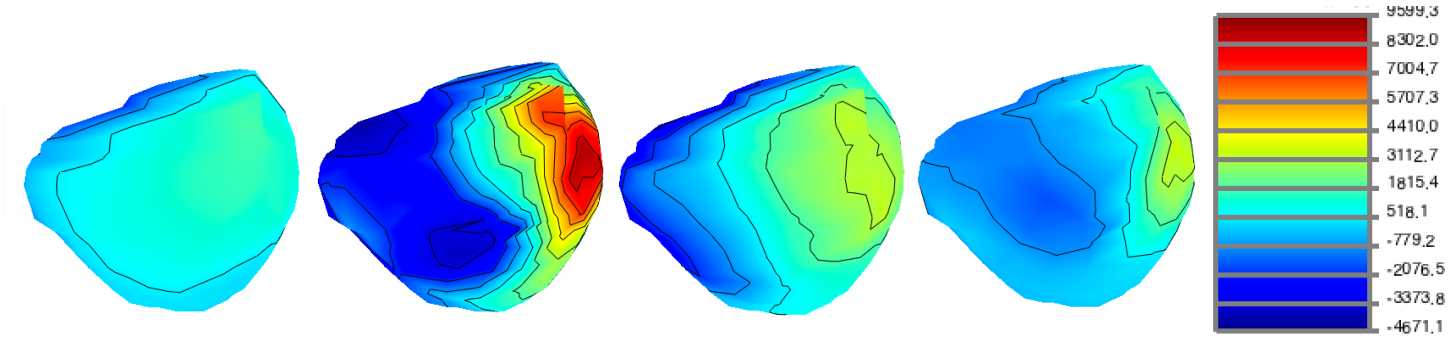

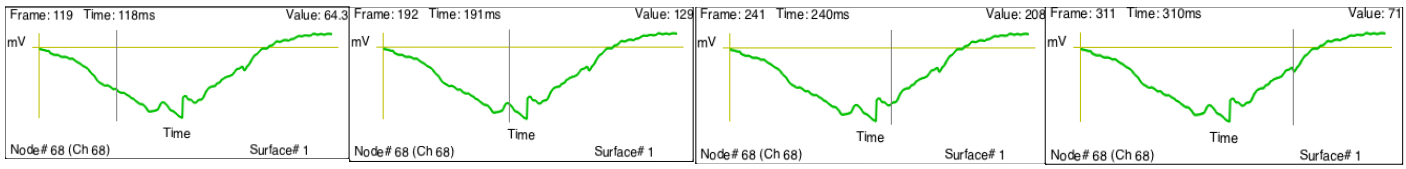

LAPLACIAN REGULARIZATION

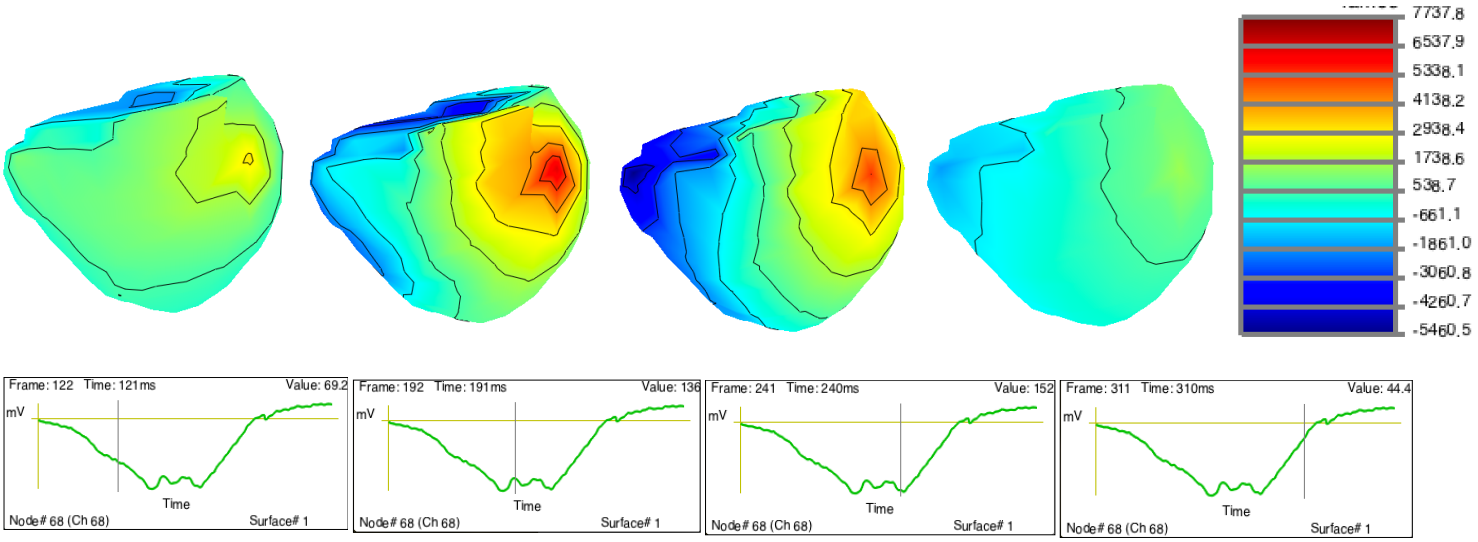

GRADIENT REGULARIZATION

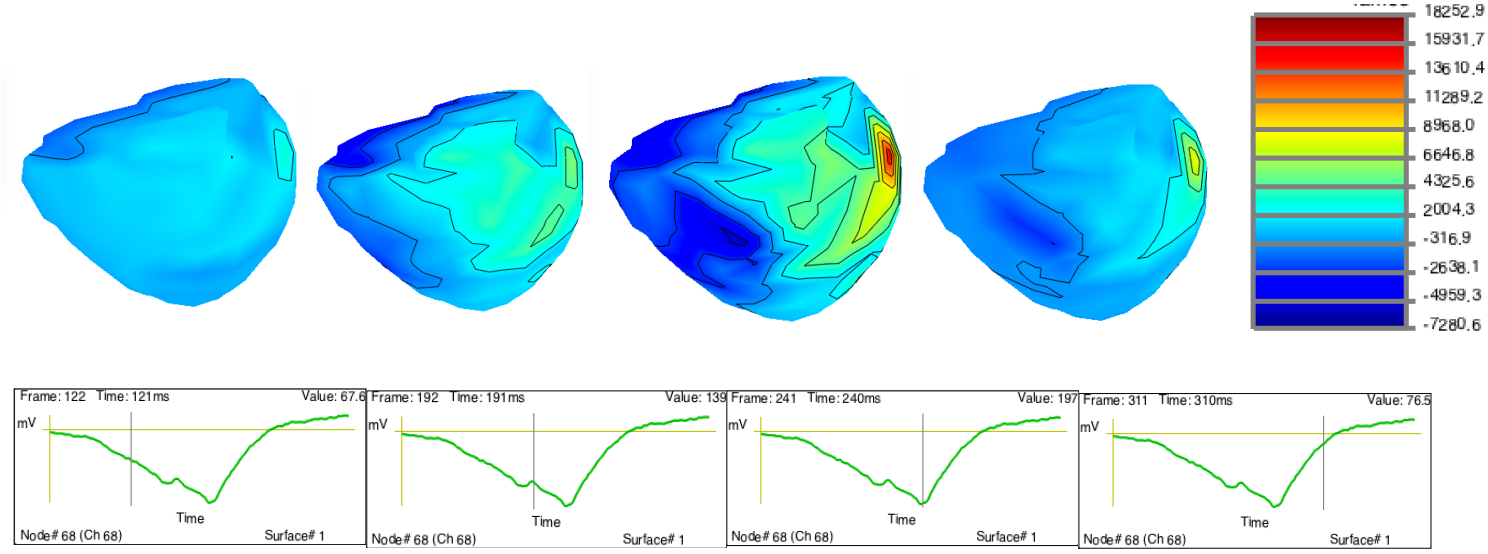

Case C_158: PACE 10/12 FOR VT2; DELAY = 80 ms

Pacing Site: # Node 172

RAW Data

IDENTITY REGULARIZATION

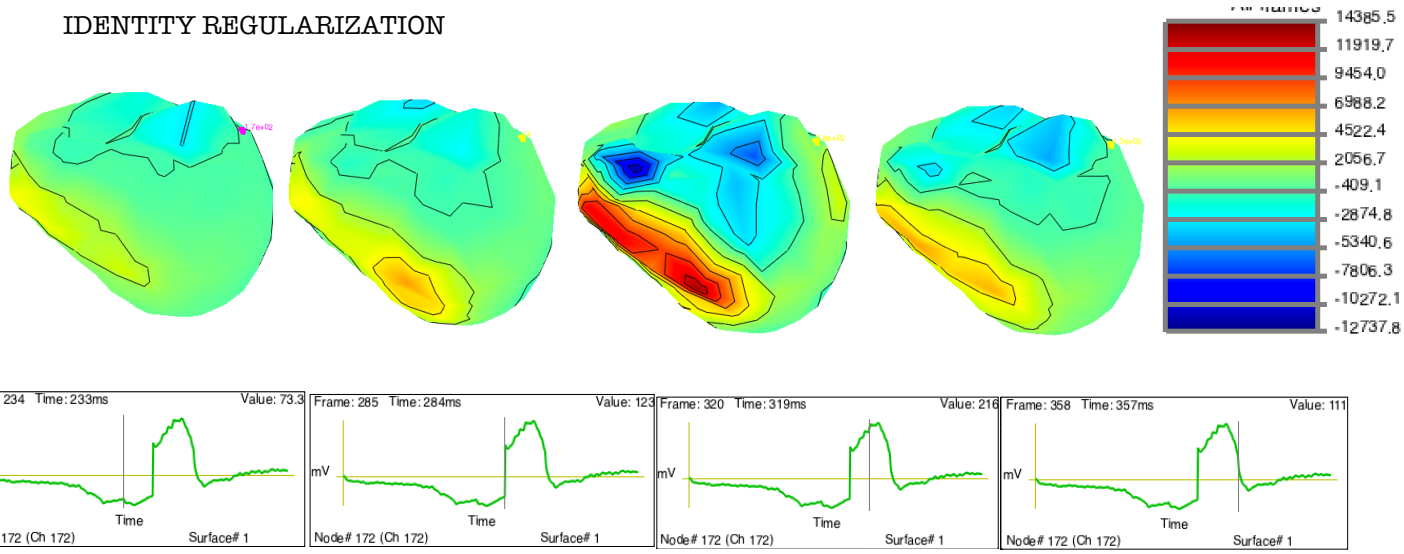

HESSIAN REGULARIZATION

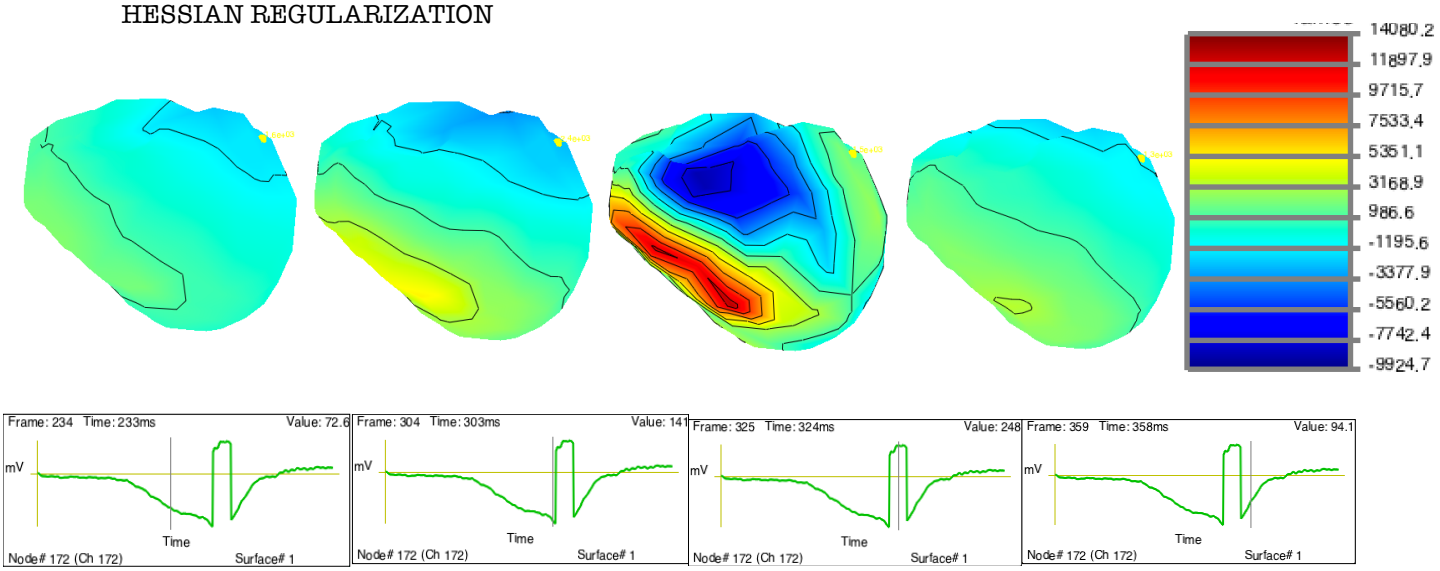

LAPLACIAN REGULARIZATION

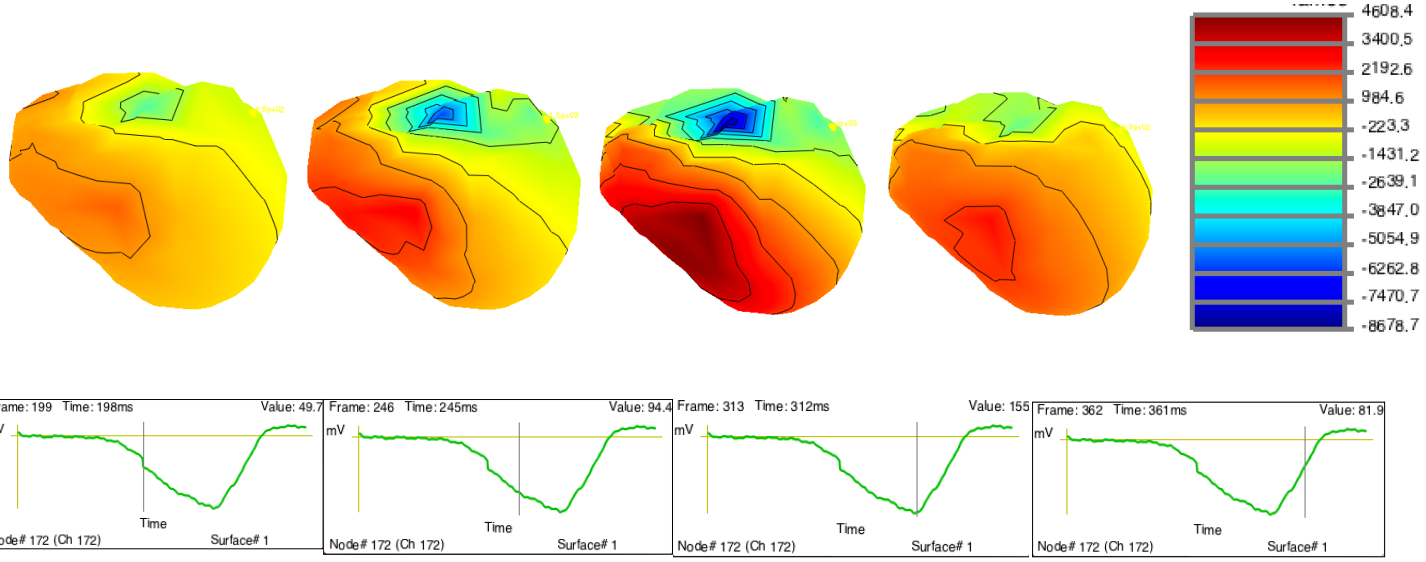

GRADIENT REGULARIZATION

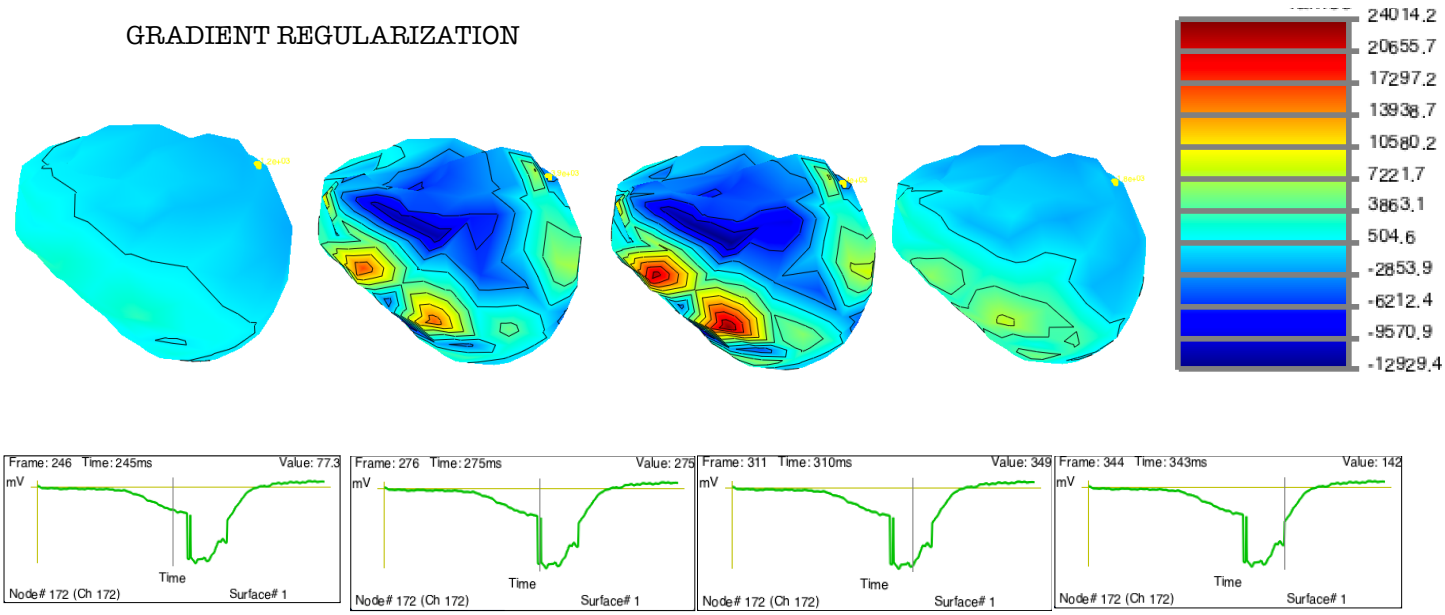

Case C_170: M1 C170 PACE; DELAY = 55 ms

Pacing Site: # Node 125

RAW Data

IDENTITY REGULARIZATION

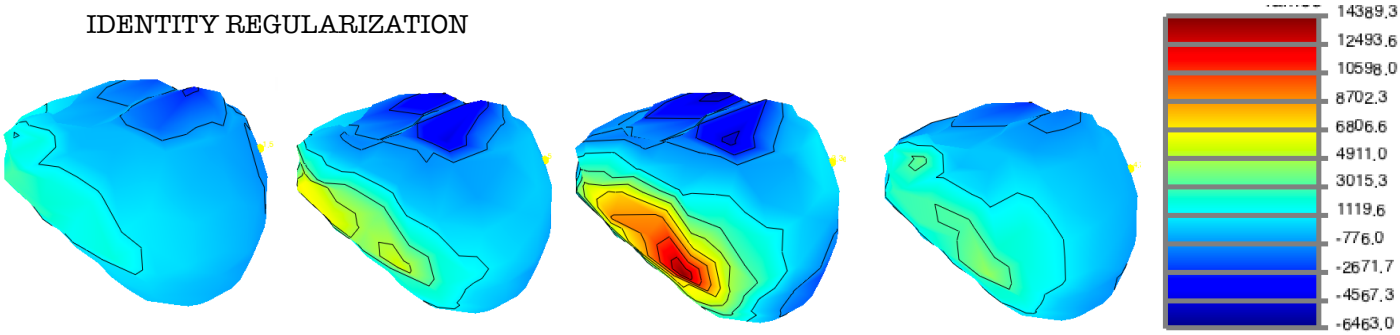

HESSIAN REGULARIZATION

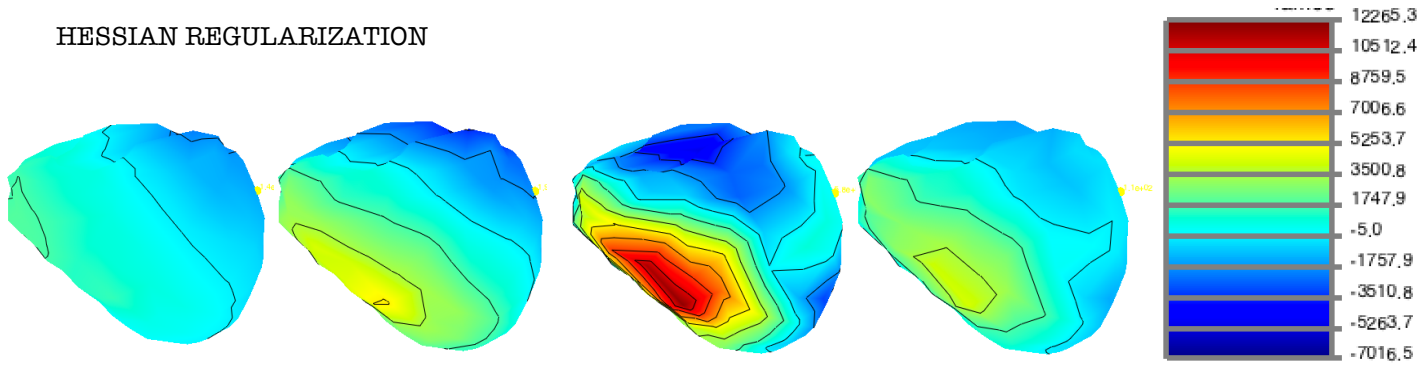

LAPLACIAN REGULARIZATION

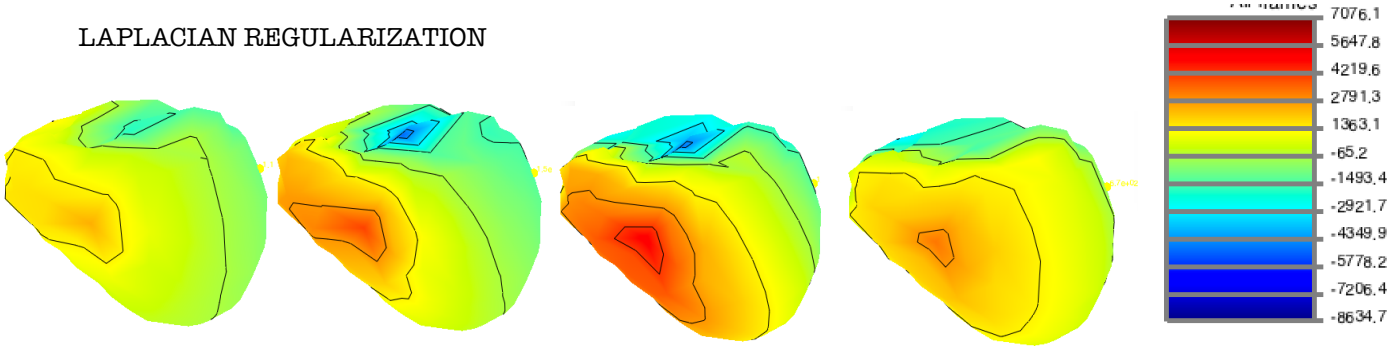

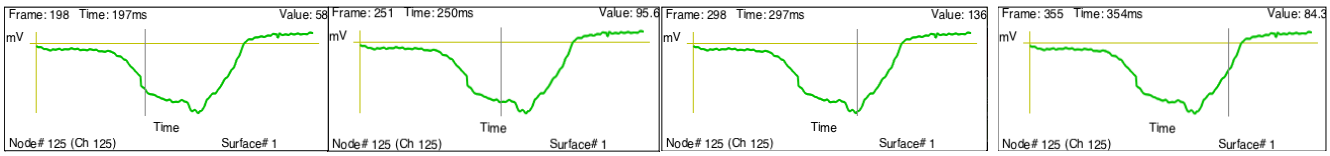

GRADIENT REGULARIZATION

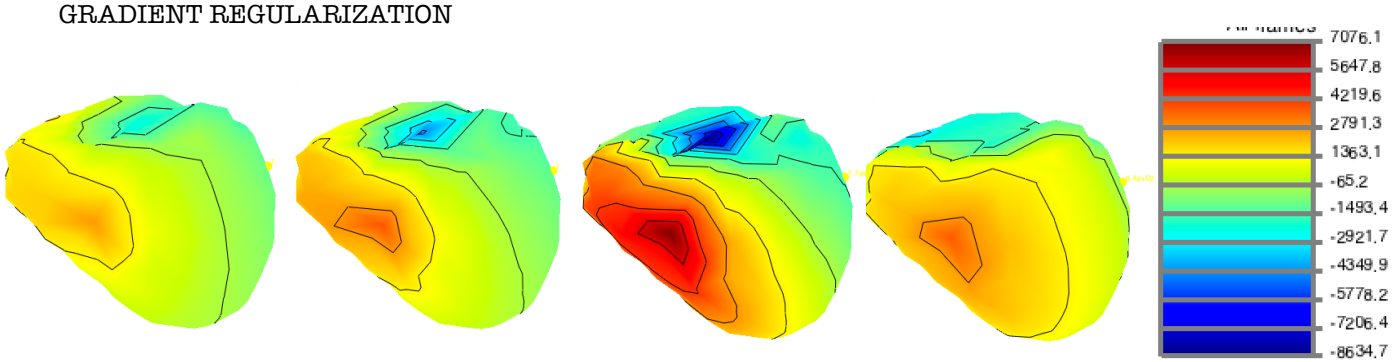

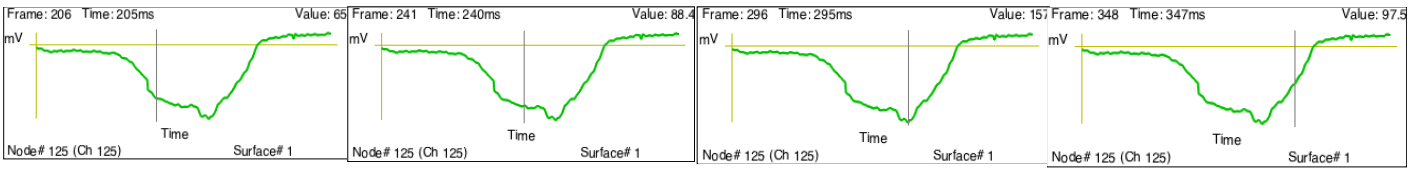

5.1.2. Pacing site localization.Relative errors per Regularization Matrix

IDENTITY REGULARIZATION

	Divergence method		Temporal Derivative method	
	RAW Data	Interpolated Data	RAW Data	Interpolated Data
C18	99,7	99,7	46,5	80,7
C22	31,7	89,5	48,2	30,9
C24	47,2	98,1	71,4	33,5
C30	85,0	78,9	61,0	37,2
C32	103,3	115,7	18,6	60,1
C36	100,5	112,4	36,5	66,2
C40	139,2	139,2	34,5	34,5
C46	123,2	123,19	55,1	58,8
C48	104,6	104,6	12,8	30,2
C50	117,2	117,2	81,2	70,3
C58	109,3	124,3	40,8	33,4
C62	114,5	121,9	45,6	45,6
C69	124,6	101,0	75,3	31,5
C74	93,7	93,7	27,1	27,1
C86	53,1	64,4	96,8	26,8
C100	103,3	115,7	60,1	18,6
C150	104,6	104,6	30,2	40,8
C158	102,6	102,6	52,9	16,3
C167	102,6	102,6	52,9	18,2
C170	93,5	93,5	64,1	22,3

Table 5.1.2.1. Relative Error Measures per subject-specific case reconstructing the inverse solutions by means of the Identity Matrix as the Regularization Matrix.

HESSIAN REGULARIZATION

	Divergence method		Temporal Derivative method	
	RAW Data	Interpolated Data	RAW Data	Interpolated Data
C18	111,5	103,1	46,5	0
C22	52,9	51,2	48,2	31,7
C24	47,2	67,9	31,9	61,9
C30	32,4	38,8	66,4	54,0
C32	77,7	112,6	60,1	60,1
C36	103,8	92,2	81,4	66,2
C40	126,3	116,3	117,6	34,5
C46	116,5	80,9	55,1	87,9
C48	46,0	35,1	12,8	40,8
C50	27,6	27,6	86,6	80,9
C58	118,5	83,8	109,2	109,2
C62	73,9	73,9	45,6	45,6
C69	36,0	36,0	31,2	75,3
C74	27,3	27,3	27,1	74,5
C86	39,9	56,6	96,8	54,8
C100	77,7	113,8	106,2	18,6
C150	46,0	35,1	12,8	40,8
C158	88,9	35,1	47,4	47,4
C167	88,9	35,1	47,4	102,8
C170	113,5	52,4	42,9	111,2

Table 5.1.2.2. Relative Error Measures per subject-specific case reconstructing the inverse solutions by means of the Hessian Matrix as the Regularization Matrix.

LAPLACIAN REGULARIZATION

	Divergence method		Temporal Derivative method	
	RAW Data	Interpolated Data	RAW Data	Interpolated Data
C18	86,5	80,7	46,5	84,4
C22	39,8	39,8	34,1	34,1
C24	57,4	51,3	78,8	31,9
C30	37,2	37,2	54,0	63,8
C32	91,6	91,6	41,2	60,1
C36	75,8	75,8	81,4	81,4
C40	129,3	66,9	117,6	34,5
C46	88,5	88,5	72,4	72,4
C48	12,8	40,8	78,4	74,9
C50	86,6	86,6	109,2	49,5
C58	40,8	40,8	66,3	40,8
C62	45,6	45,6	66,9	114,4
C69	76,9	75,3	107,3	124,6
C74	27,1	27,1	27,1	64,0
C86	26,8	26,8	65,9	92,5
C100	91,6	91,6	60,1	60,1
C150	40,8	40,8	68,3	40,8
C158	56,6	52,9	47,4	47,4
C167	52,9	52,9	102,8	47,4
C170	47,5	47,5	64,1	64,1

Table 5.1.2.3. Relative Error Measures per subject-specific case reconstructing the inverse solutions by means of the Laplacian Matrix as the Regularization Matrix.

GRADIENT REGULARIZATION

	Divergence method		Temporal Derivative method	
	RAW Data	Interpolated Data	RAW Data	Interpolated Data
C18	52,2	103,1	58,3	46,5
C22	31,7	73,4	48,2	40,3
C24	47,2	85,3	61,9	85,6
C30	38,8	64,2	61,0	91,1
C32	103,3	109,6	70,1	60,1
C36	100,5	97,6	70,0	86,9
C40	112,2	112,2	34,5	66,9
C46	51,7	120,5	83,8	72,4
C48	62,5	58,6	78,2	40,8
C50	34,8	34,8	86,6	45,3
C58	92,6	92,6	40,8	40,8
C62	86,9	86,9	45,6	45,6
C69	60,5	60,5	65,0	97,7
C74	34,5	36,1	27,1	27,1
C86	53,0	64,8	100,8	26,8
C100	48,3	109,6	77,7	43,2
C150	62,5	58,6	40,8	40,8
C158	65,6	16,4	47,4	102,8
C167	65,6	67,8	47,4	67,8
C170	78,7	78,7	63,2	55,5

Table 5.1.2.4. Relative Error Measures per subject-specific case reconstructing the inverse solutions by means of the Gradient Matrix as the Regularization Matrix.

5.1.3. Simulations. Visual comparison between Tikhonov Regularization and Hansen approach

Case C_46: RBBB morphology; DELAY = 80 ms

Pacing Site: # Node 73

RAW Data

IDENTITY REGULARIZATION

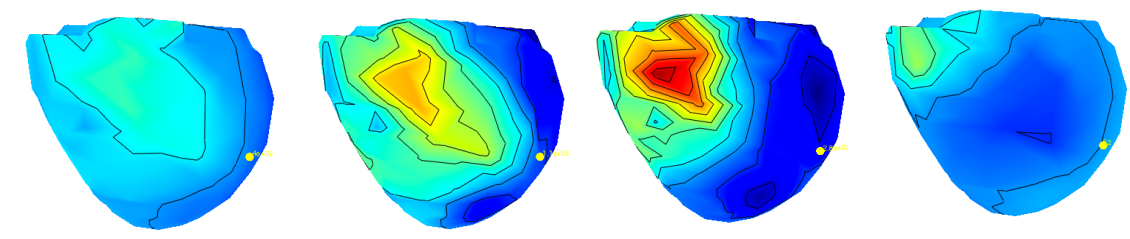

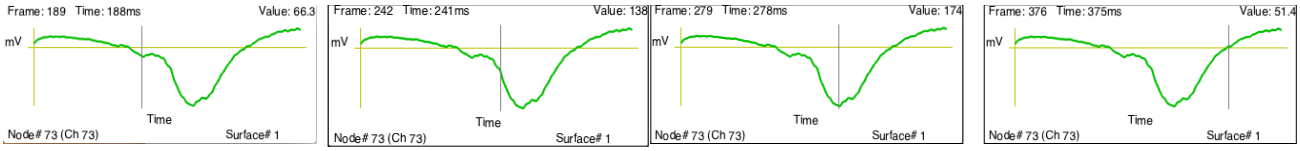

HANSEN REGULARIZATION

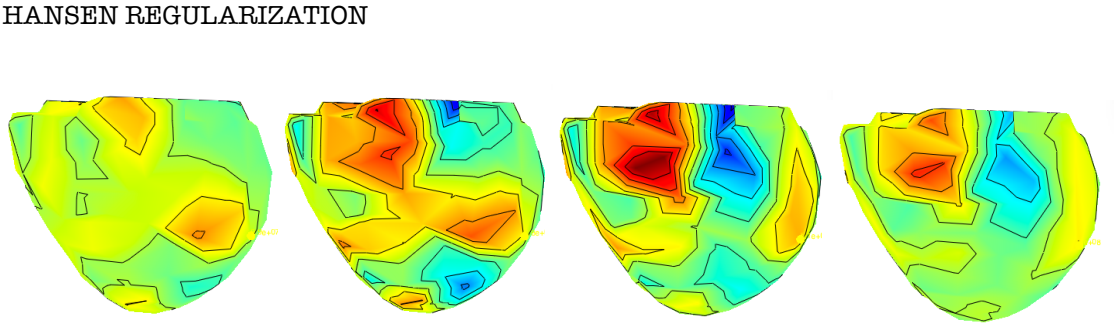

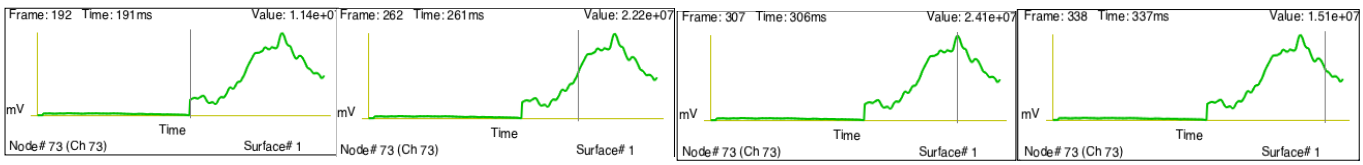

Case C_58: PACE (VT2 MATCH)

Pacing Site: # Node 68

RAW Data

IDENTITY REGULARIZATION

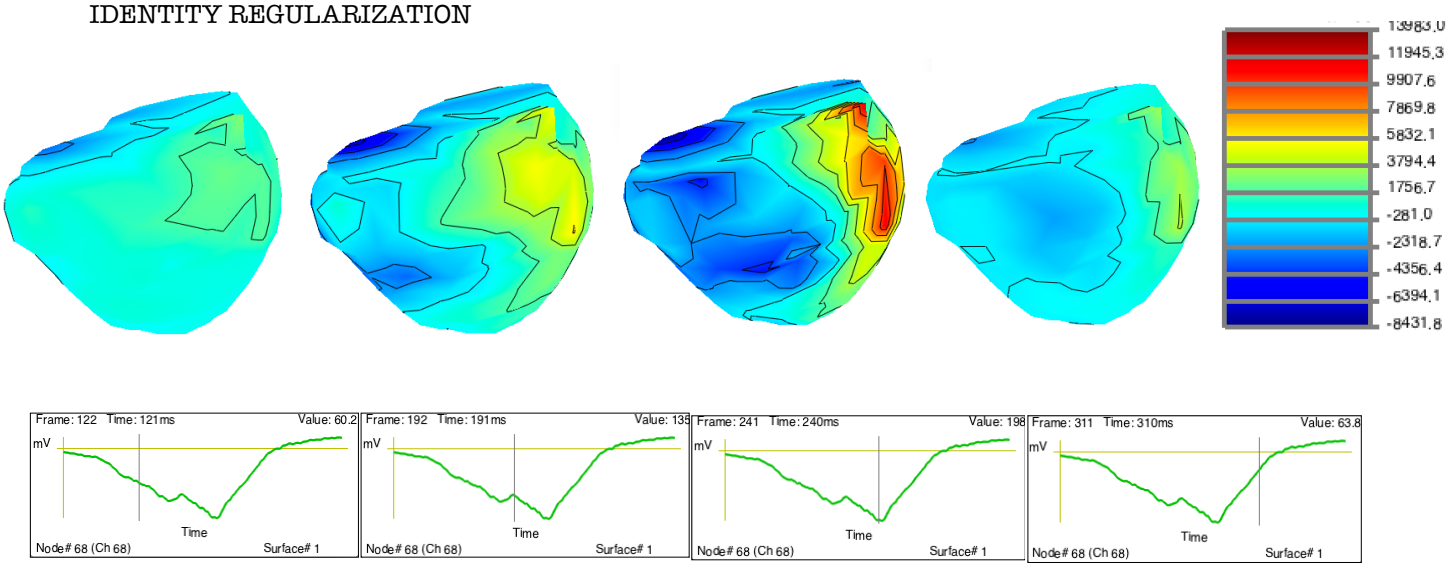

HANSEN REGULARIZATION

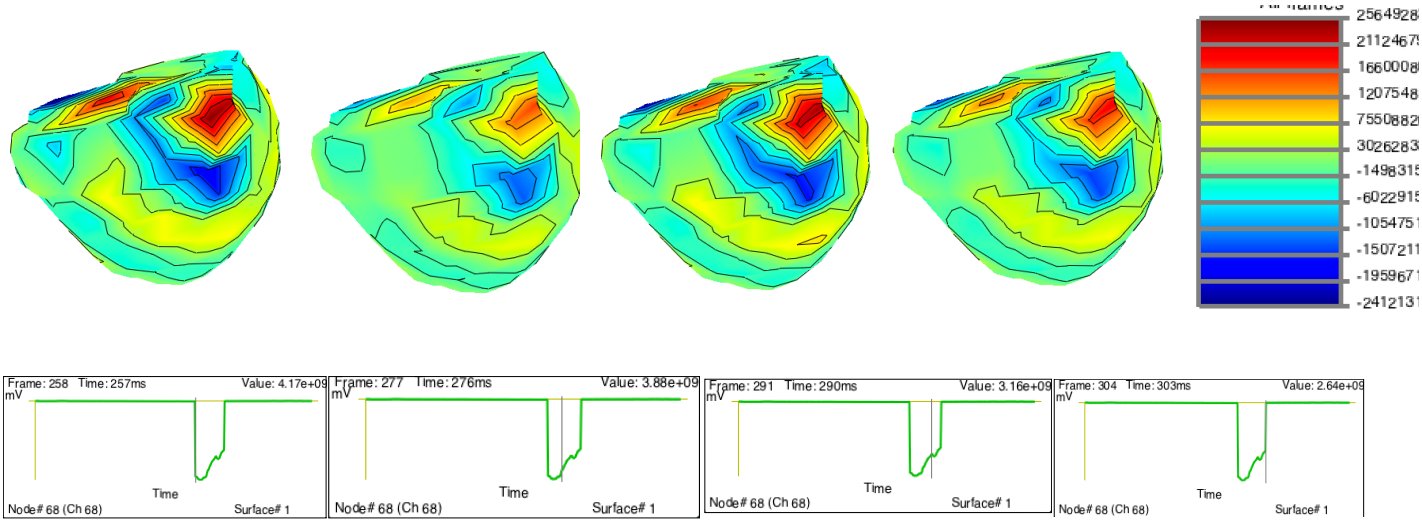

Case C_158: PACE 10/12 FOR VT2; DELAY = 80 ms

Pacing Site: # Node 172

RAW Data

IDENTITY REGULARIZATION

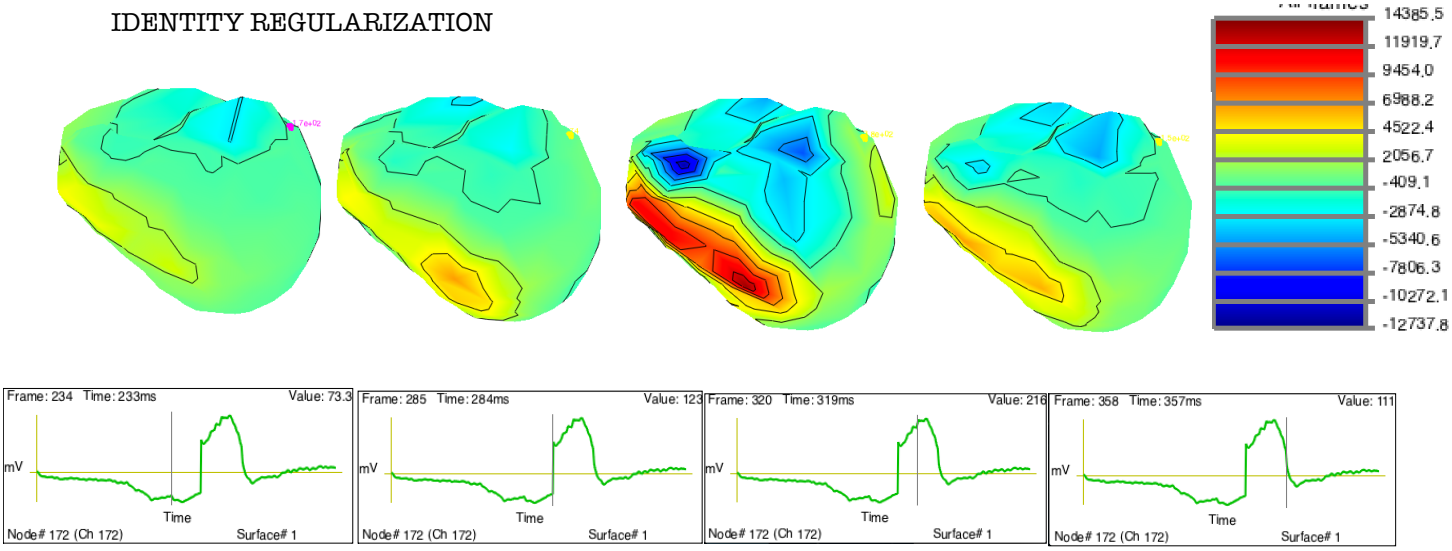

HANSEN REGULARIZATION

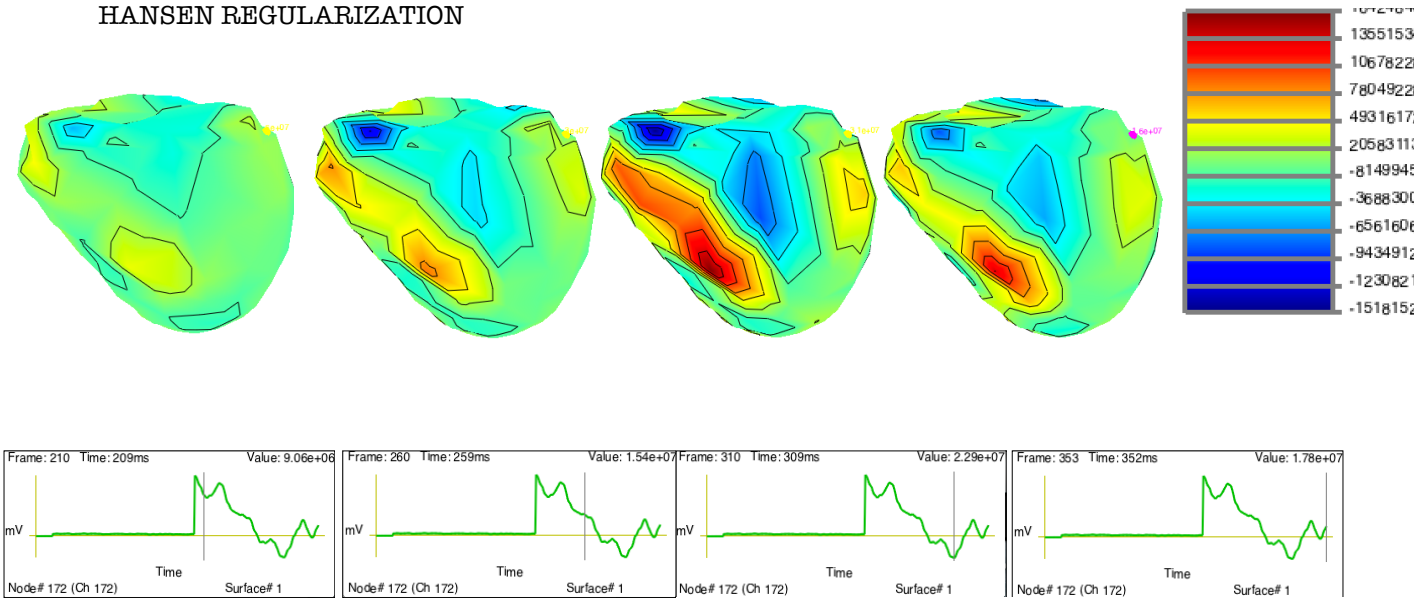

Case C_170: M1 C170 PACE; DELAY = 55 ms

Pacing Site: # Node 125

RAW Data

IDENTITY REGULARIZATION

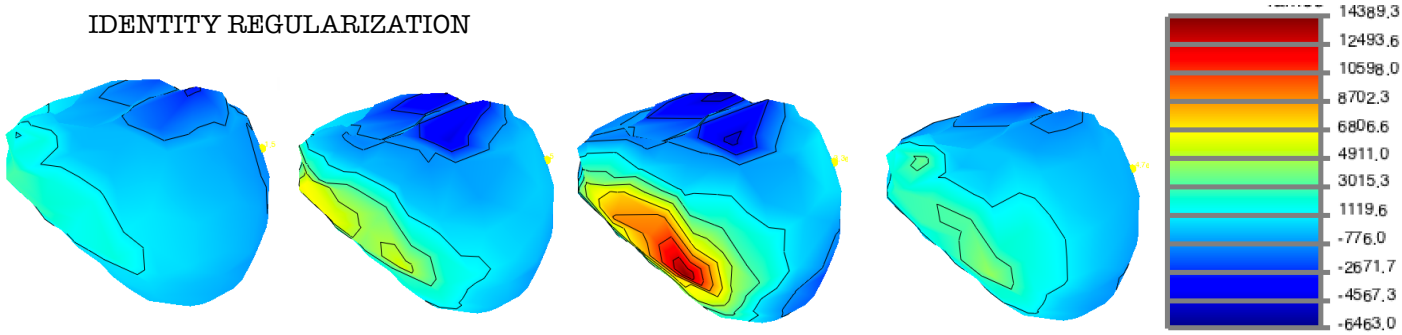

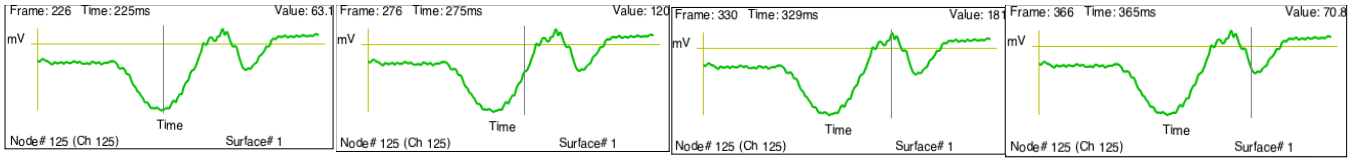

HANSEN REGULARIZATION

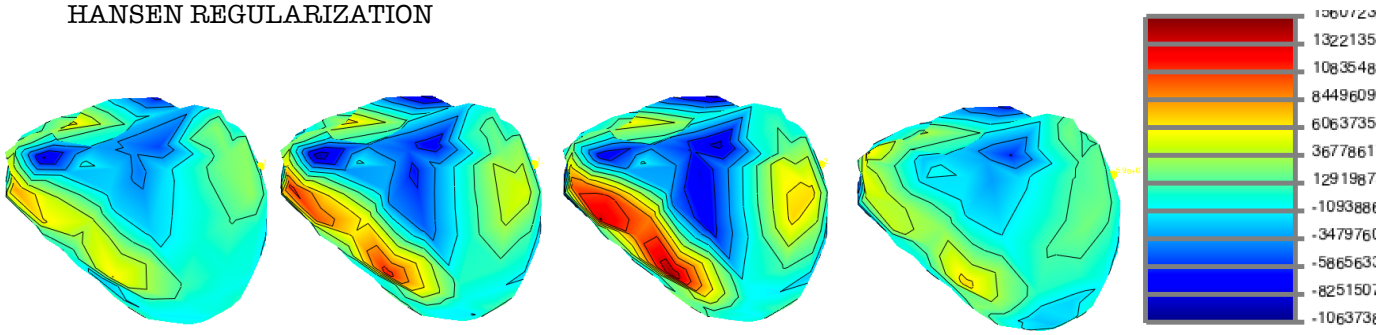

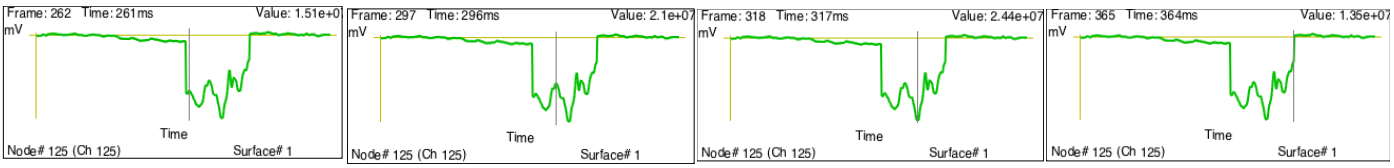

5.1.4. Pacing site localization. Relative errors per Hansen approach

HANSEN REGULARIZATION

	Divergence method		Temporal Derivative method	
	RAW Data	Interpolated Data	RAW Data	Interpolated Data
C18	99,7	99,7	95,3	46,5
C22	79,5	48,2	67,1	64,7
C24	57,4	31,9	30,3	71,4
C30	86,4	61,0	66,4	96,1
C32	103,3	60,1	87,5	106,2
C36	81,4	81,4	47,0	97,5
C40	117,6	117,6	117,6	110,3
C46	123,1	80,9	72,4	57,9
C48	109,3	104,6	78,2	12,8
C50	87,5	107,1	42,6	75,6
C58	66,8	109,2	109,2	69,0
C62	67,2	122,8	82,7	80,0
C69	107,3	109,3	107,3	124,6
C74	43,9	81,2	27,1	92,5
C86	48,6	66,5	67,1	69,3
C100	62,2	60,1	18,6	106,2
C150	57,8	57,8	78,7	46,5
C158	102,6	102,6	49,1	48,7
C167	102,6	102,8	47,4	84,2
C170	93,5	111,2	64,1	36,5

Table 5.1.4. Relative Error Measures per subject-specific case reconstructing the inverse solutions by the use of the Hansen approach.

5.1.5. Simulations. Visual comparison between Tikhonov regularization and the Dynamic Model

Case C_46: RBBB morphology; DELAY = 80 ms

Pacing Site: # Node 73

RAW Data

GRADIENT REGULARIZATION

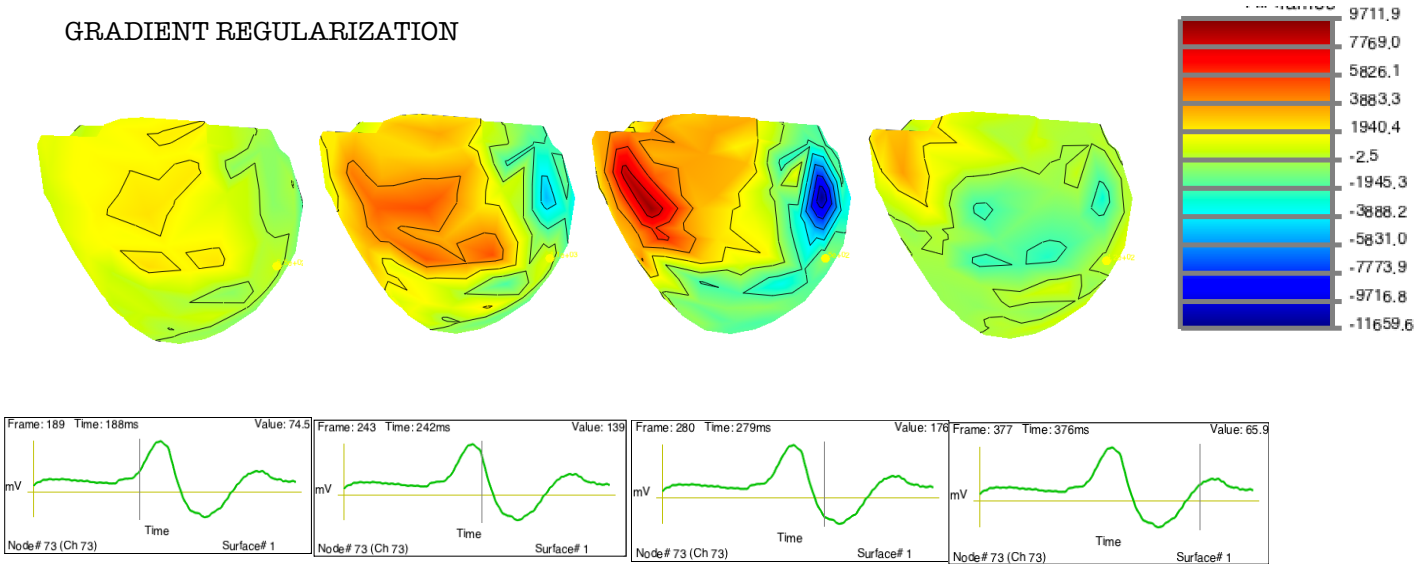

DYNAMIC MODEL

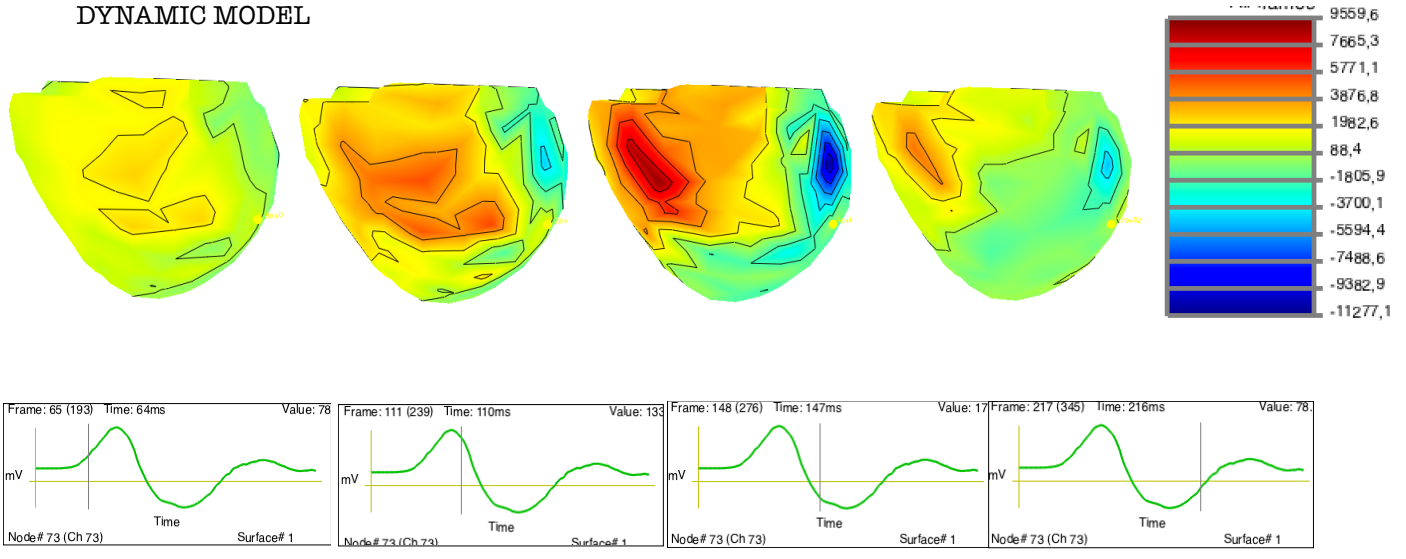

Case C_58: PACE (VT2 MATCH)

Pacing Site: # Node 68

RAW Data

GRADIENT REGULARIZATION

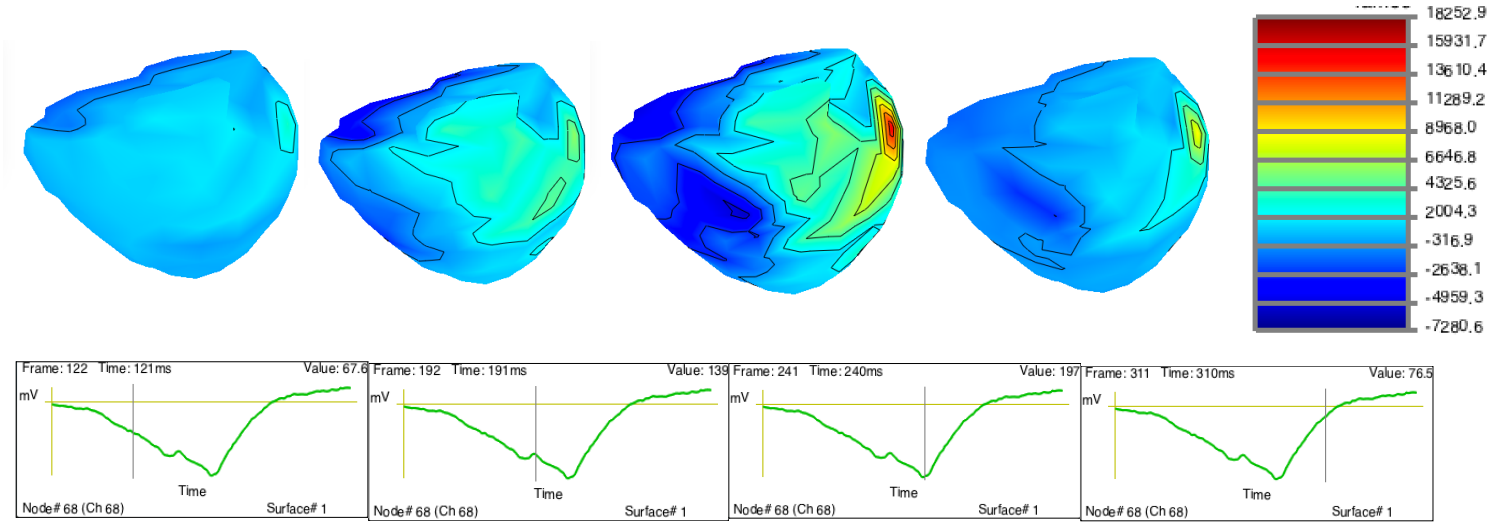

DYNAMIC MODEL

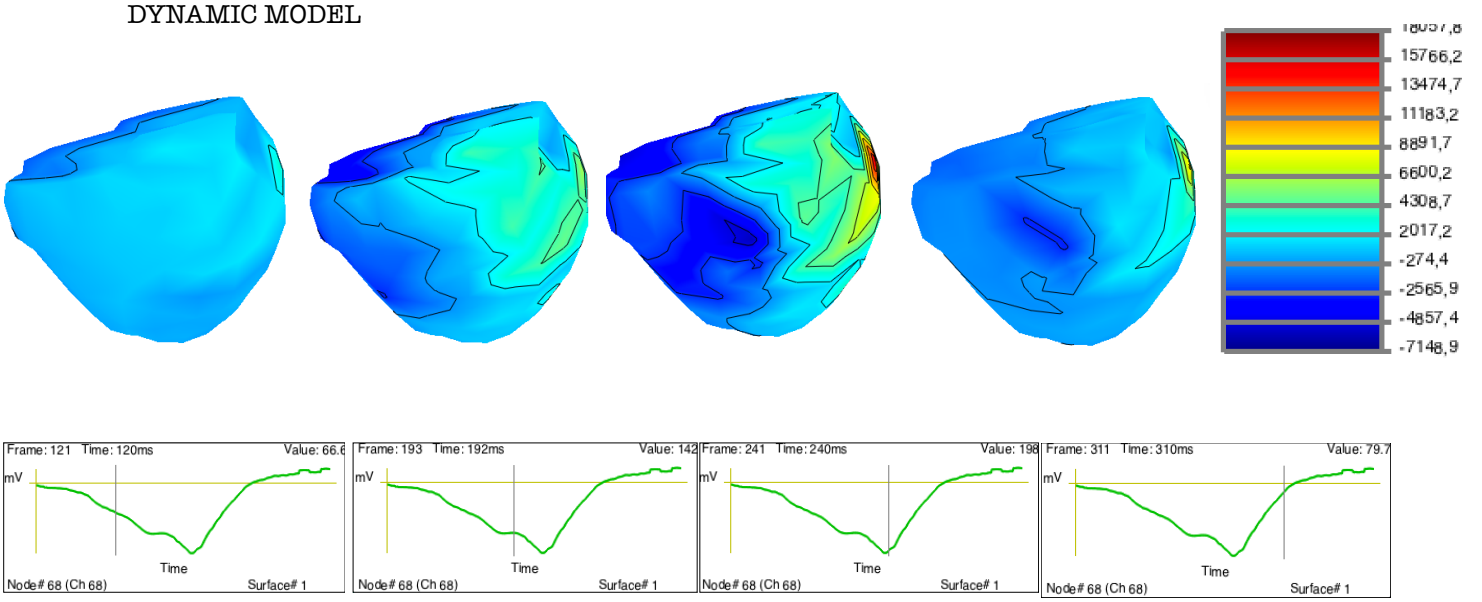

Case C_158: PACE 10/12 FOR VT2; DELAY = 80 ms

Pacing Site: # Node 172

RAW Data

GRADIENT REGULARIZATION

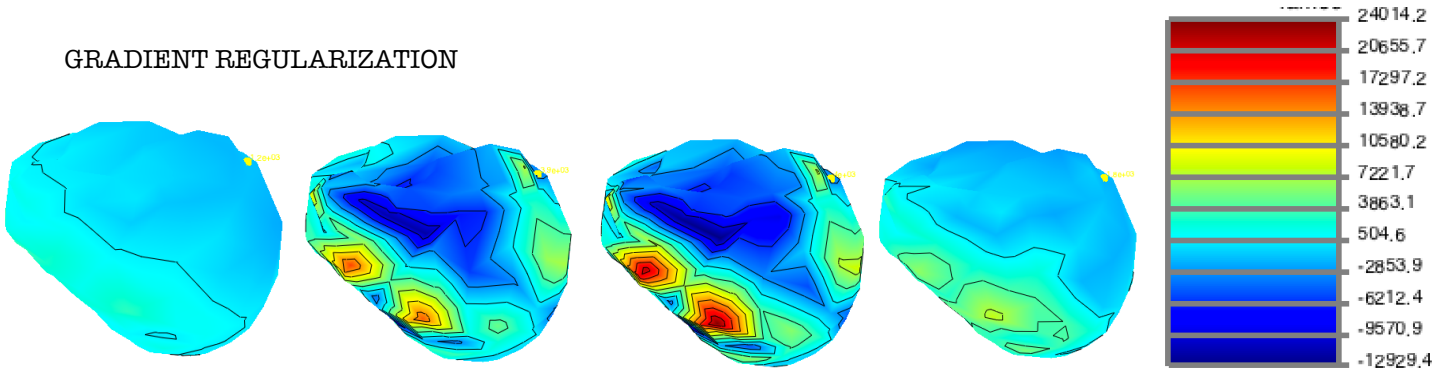

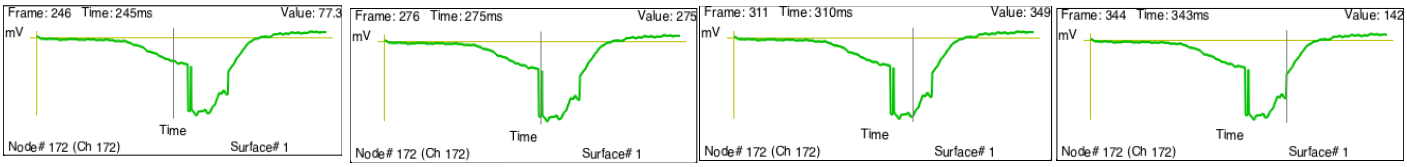

DYNAMIC MODEL

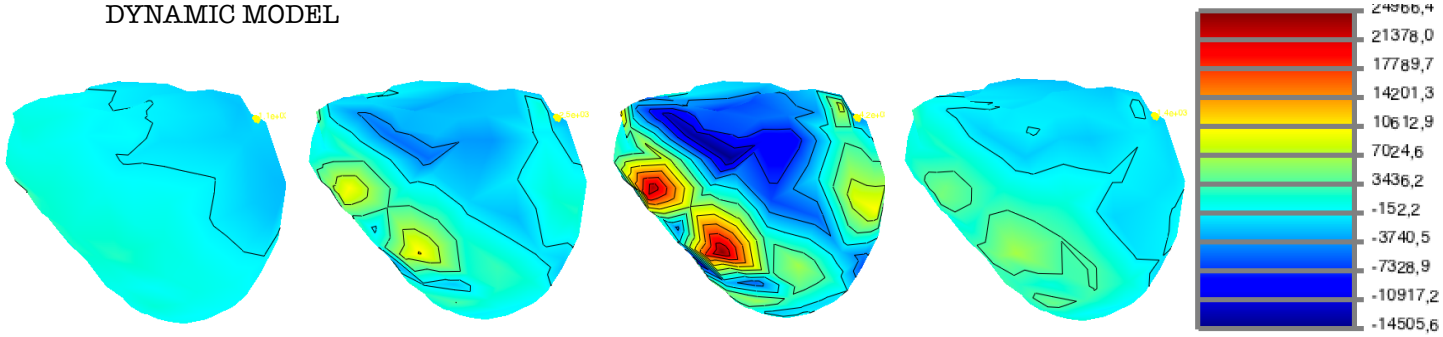

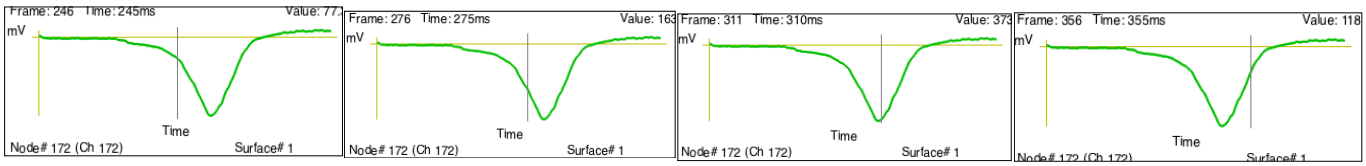

Case C_170: M1 C170 PACE; DELAY = 55 ms

Pacing Site: # Node 125

RAW Data

GRADIENT REGULARIZATION

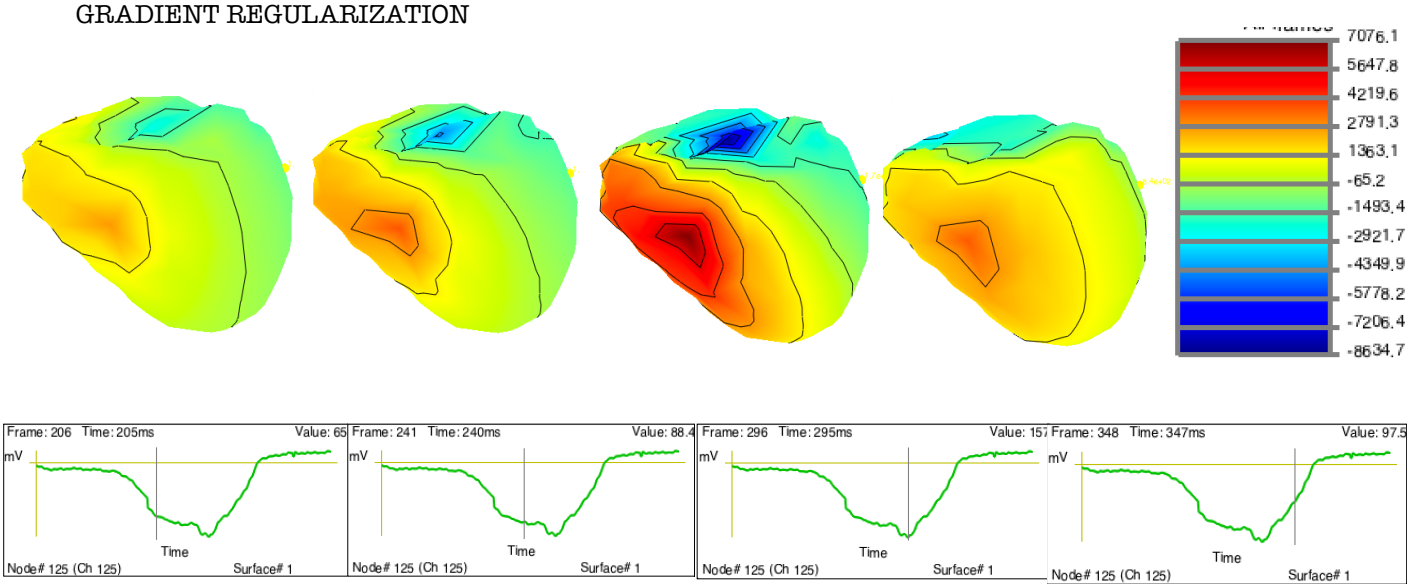

DYNAMIC MODEL

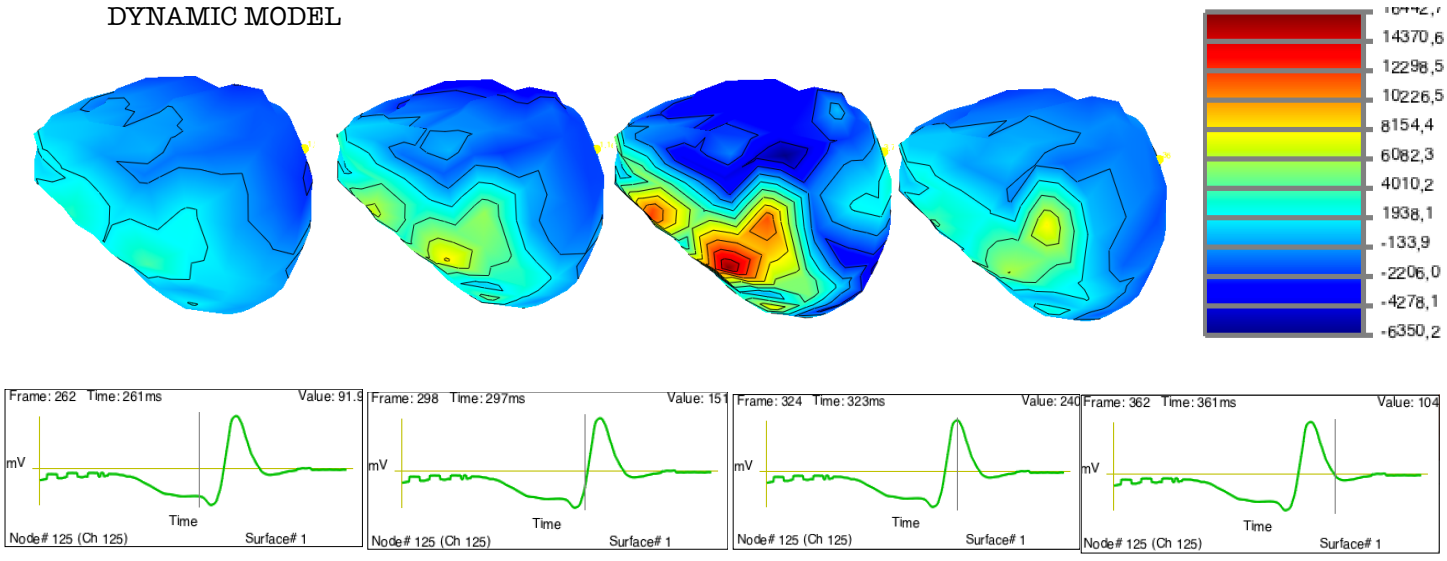

5.1.6. Pacing site localization. Relative errors per the Dynamic model on the Epicardial geometry

DYNAMIC MODEL
Epicardial Geometry

	Divergence method		Temporal Derivative method	
	RAW Data	Interpolated Data	RAW Data	Interpolated Data
C18	103,6	24,1	46,5	96,4
C22	31,7	73,4	48,2	39,8
C24	47,2	62,6	31,9	31,9
C30	38,8	37,2	85,1	66,4
C32	48,39	109,6	20,5	60,1
C36	100,5	97,6	41,4	66,2
C40	112,2	112,2	18,9	66,9
C46	80,9	51,7	72,4	90,3
C48	62,5	62,5	40,8	12,8
C50	34,8	34,8	117,2	117,2
C58	92,6	92,6	78,3	78,3
C62	86,9	86,9	30,5	66,9
C69	25,2	60,5	124,6	93,6
C74	95,5	19,2	55,5	74,1
C86	89,4	64,8	54,8	35,2
C100	48,3	109,6	20,5	60,1
C150	62,5	58,6	40,1	40,8
C158	65,6	67,8	50,4	52,9
C167	65,6	67,8	47,4	52,9
C170	78,7	78,7	47,57	16,5

Table 5.1.6. Relative Error Measures per subject-specific case reconstructing the inverse solutions by the use of the Dynamic Model in the Epicardial Geometry.

5.2. Reconstructed epicardial and endocardial potentials on the Ventricular Geometry

5.2.1. Simulations. Dynamic Model inverse solutions

Case C_46: RBBB morphology; DELAY = 80 ms

Pacing Site: # Node 124

RAW Data

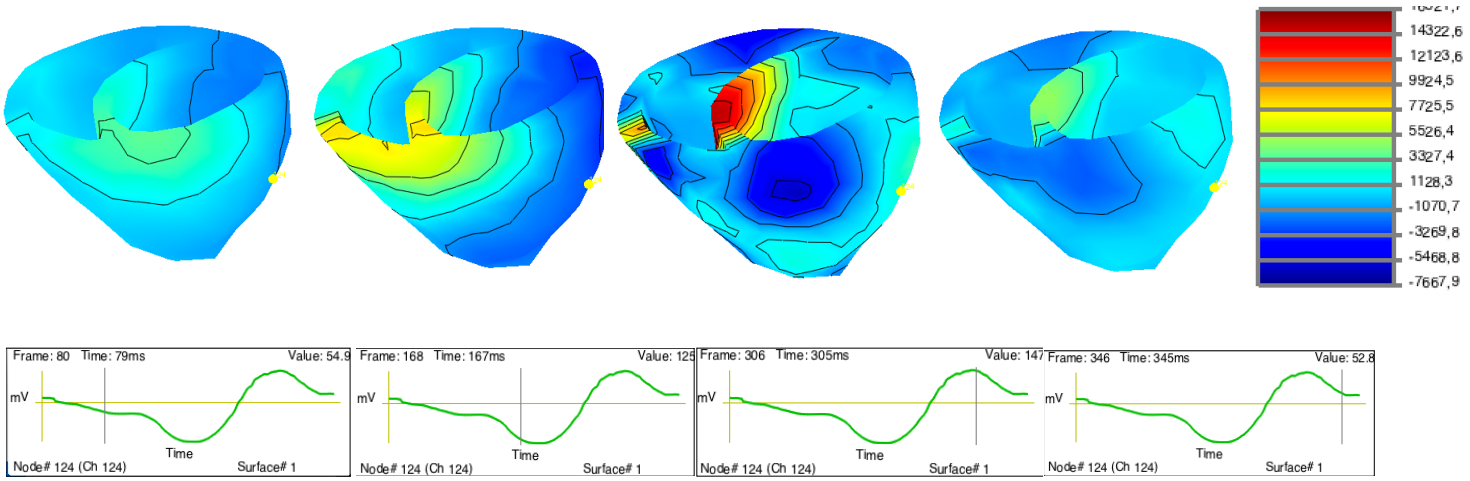

Case C_58: PACE (VT2 MATCH)

Pacing Site: # Node 51

RAW Data

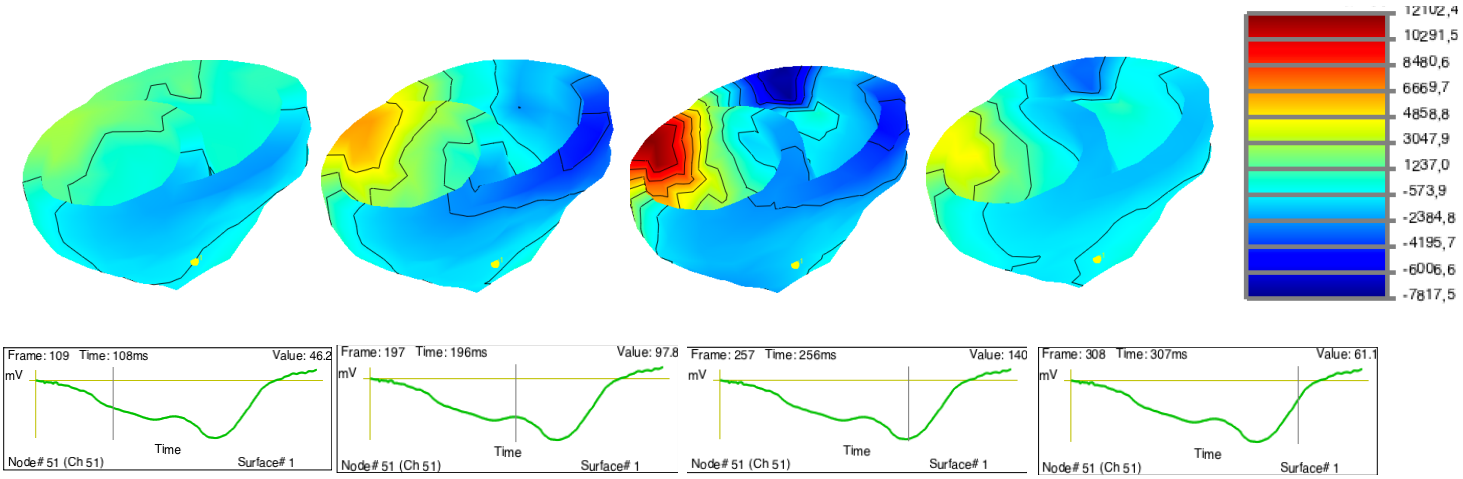

Case C_158: PACE 10/12 FOR VT2; DELAY = 80 ms

Pacing Site: # Node 219

RAW Data

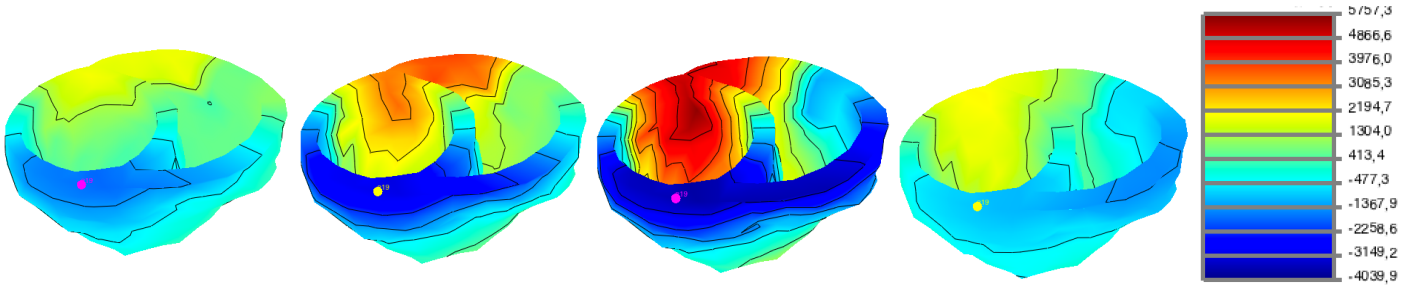

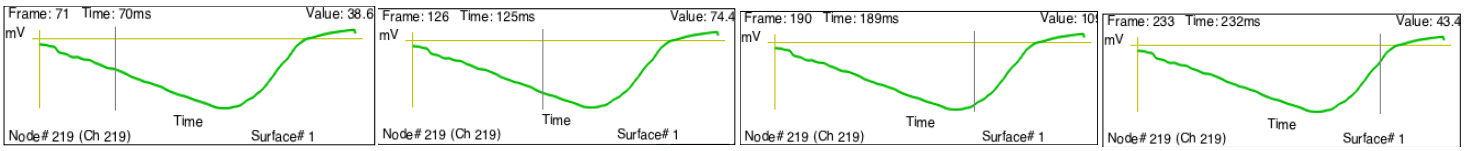

Case C_170: M1 C170 PACE; DELAY = 55 ms

Pacing Site: # Node 147

RAW Data

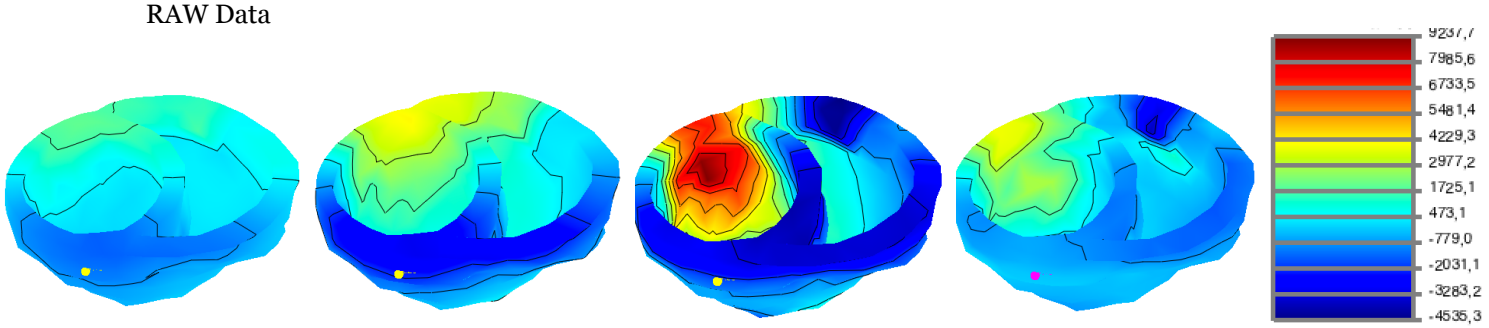

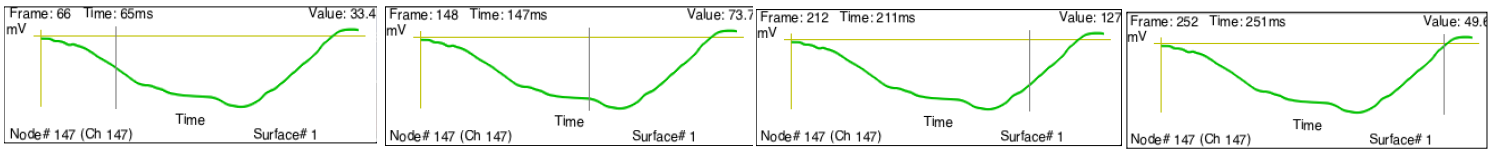

5.2.2. Pacing site localization. Relative errors per the Dynamic model on the Ventricular geometry

DYNAMIC MODEL
Ventricular Geometry

	Divergence method		Temporal Derivative method			
			Surface operators Dtan, Ltan		Volumetric operators cDf, cLf	
	RAW Data	Interp. Data	RAW Data	Interp. Data	RAW Data	Interp. Data
C18	88,5	87,0	72,5	83,4	93,3	74,9
C22	17,1	16,9	49,8	31,3	88,8	24,1
C24	39,3	62,6	103,6	39,3	84,1	34,8
C30	55,0	55,0	51,9	38,6	94,4	63,0
C32	54,6	106,9	46,3	35,2	66,7	42,6
C36	84,9	84,9	38,8	63,4	48,7	62,5
C40	86,6	87,8	49,4	82,7	60,6	82,7
C46	68,4	68,4	34,2	77,1	73,2	53,7
C48	18,4	18,4	61,5	68,7	96,2	68,0
C50	72,6	72,6	67,4	67,4	65,1	59,8
C58	62,6	23,2	55,6	79,9	61,4	66,1
C62	45,6	45,6	11,7	18,5	11,7	28,0
C69	78,4	84,9	30,8	59,6	37,6	28,6
C74	15,0	15,0	15,0	83,9	85,3	85,3
C86	79,5	10,3	40,1	100,8	51,1	87,9
C100	46,1	80,1	39,0	30,1	58,1	26,6
C150	18,4	18,4	66,6	71,4	68,2	74,6
C158	77,4	77,4	49,8	45,4	9,9	44,5
C167	55,7	71,2	64,0	48,9	41,7	41,7
C170	84,5	63,2	49,1	15,4	20,6	38,1

Table 5.2.2. Relative Error Measures per subject-specific case reconstructing the inverse solutions by the use of the Dynamic Model in the Ventricular Geometry.

5.3. Final comparison among all the Regularization methods

Comparison of average relative errors (mm) over the entire QRS of 20 heartbeat cases for 8 regularization and pacing site location methods.

- RAW Data

	Epicardial Geometry						Epicardial and Endocardial Geometry	
	Identity Reg.	**Hansen Reg.**	**Hessian Reg.**	**Lapl. Reg.**	**Grad. Reg.**	**DM**	**DM Dtan**	**DM cDf**
DV method	97,67	84,885	72,625	60,605	64,155	68,5445	57,43	57,43
TD method	50,58	67,785	58,66	69,49	60,42	53,6285	49,855	60,835

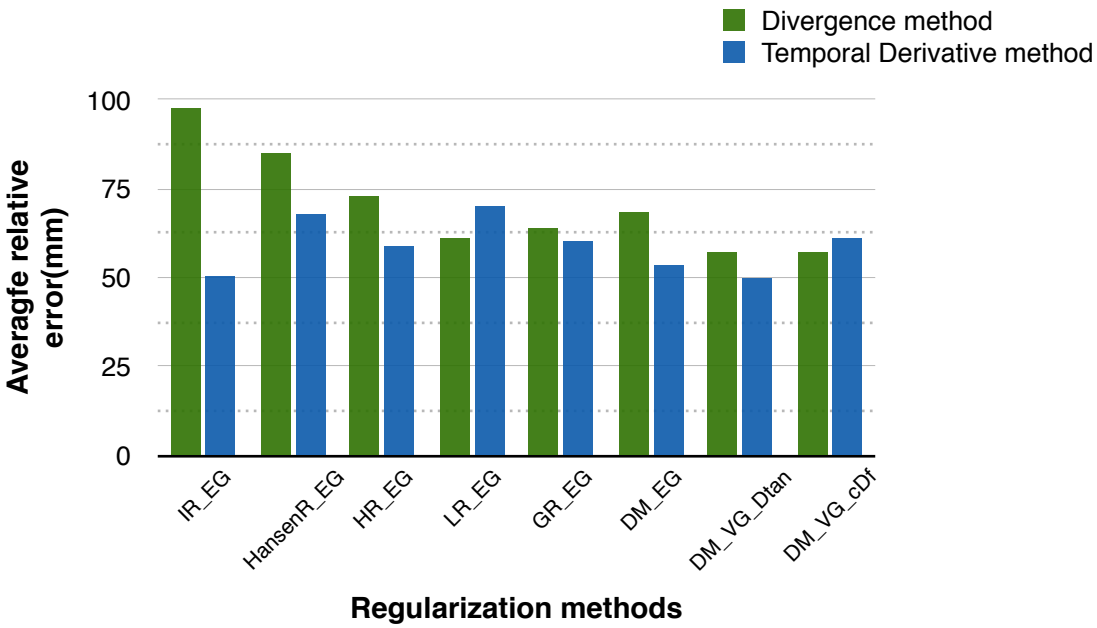

Figure 5.3.1. Average Relative Errors (mm) over 20 specific-subject cases for all the Regularization methods and Pacing Site localization algorithms over the RAW Data files.

- Interpolated Data

	Epicardial Geometry						Epicardial and Endocardial Geometry	
	Identity Reg.	**Hansen Reg.**	**Hessian Reg.**	**Lapl. Reg.**	**Grad. Reg.**	**DM**	**DM Dtan**	**DM cDf**
DV method	105,1395	85,8	63,74	58,025	76,565	68,61	57,49	57,49
TD method	39,15	74,825	59,91	64,155	59,2	60,965	57,05	54,375

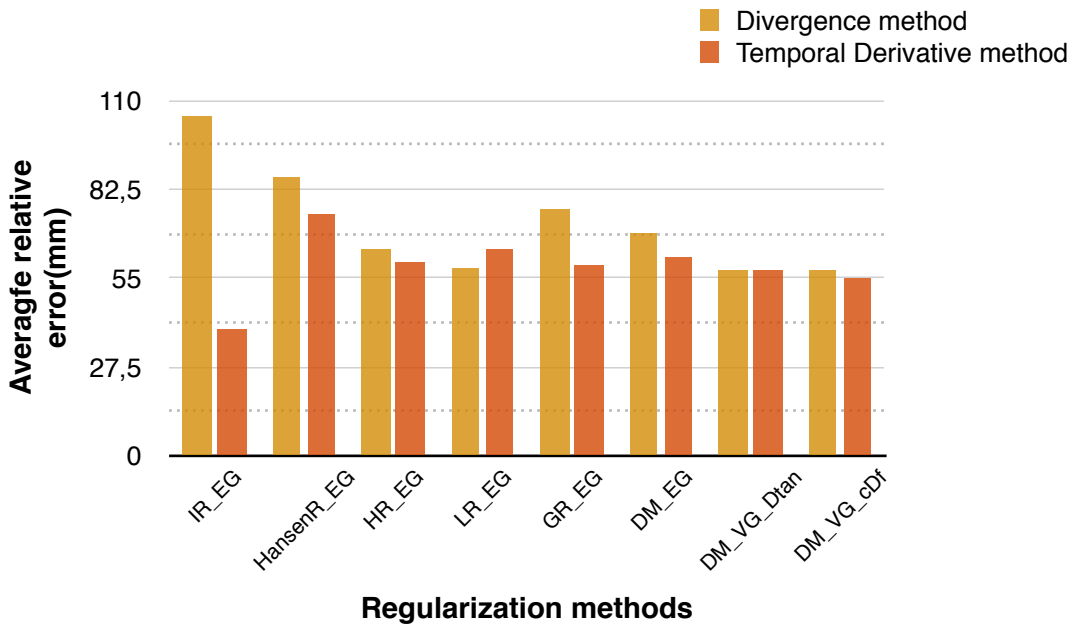

Figure 5.3.2. Average Relative Errors (mm) over 20 specific-subject cases for all the Regularization methods and Pacing Site localization algorithms over the Interpolated Data files.

The abbreviations of the regularization methods correspond to:

- ***IR_EG:*** *Tikhonov Regularization using Identity matrix on the Epicardial Geometry*
- ***HansenR_EG:*** *Hansen approach using Identity matrix on the Epicardial Geometry*
- ***HR_EG:*** *Tikhonov Regularization using Hessian matrix on the Epicardial Geometry*
- ***LR_EG:*** *Tikhonov Regularization using Laplacian matrix on the Epicardial Geometry*

- ***GR_EG:*** *Tikhonov Regularization using Gradient matrix on the Epicardial Geometry*
- ***DM_EG:*** *Dynamic modeling using Gradient matrix on the Epicardial Geometry*
- ***DM_VG_Dtan:*** *Dynamic modeling using Gradient matrix on the Ventricular Geometry. Temporal Derivative method computed by Surface Gradient and Laplacian matrices - Dtan and Ltan.*
- ***DM_VG_cDf:*** *Dynamic modeling using Gradient matrix on the Ventricular Geometry. Temporal Derivative method computed by Volumetric Gradient and Laplacian matrices - cDf and cLf.*

6. Conclusions and future development

This final section is aimed at analyzing the performance of the multiple regularization methods proposed in this project by means of visualization of the reconstructed heart potential distributions and validation of the obtained numerical measures.

The reconstructed heart potential distributions are the direct result from applying several regularization methods to a set of body surface potentials. For this reason, the first step of this analysis would be examining how these resulting inverse solutions behave along the heart surface.

Analysis of the performance of the Regularization methods in the simulations

The main issue when observing the simulations presented above is that the reconstructed heart potentials do not follow a clear propagation pathway along the heart -the electrical activation wavefront is slightly noticeable.

In overall, the results obtained by the Tikhonov regularization using the Identity matrix show activation patterns that are non-smooth over space and rapid over time. The Hessian regularization introduces local smoothness on these electrical wavefronts but still they spread too rapid to be realistic. When applying the Laplacian regularization this problematic is solved due to the degree of smoothness imposed, but at the same time the propagation pathway completely disappears. Finally, the Gradient regularization retrieve totally nonsense results: the electrical signal remains poor on a reduced area of the heart surface without showing any direction of propagation.

One possible reason that could explain these results provided by the Gradient regularization is that it has been enforced overmuch weight to the regularization term, losing this way enough signal information from the body surface measurements to reconstruct the potentials on the heart mesh.

This idea leads then to doubt if the selected regularization parameter is the correct one, which has been automatically chosen by computing the maximum curvature of the L_curve and that supposedly satisfies the regularization trade-off.

The resulting heart potentials retrieved by the Hansen approach are extremely large, non-linear and unstable, which could be possibly due to a lack of regularization.

By comparing both results provided by the Tikhonov regularization and the Dynamic model using the Gradient estimation as the type of regularization, it can be observed that they present the same visualization. However, the electrical signals in the pacing site node show that the results obtained by the Dynamic model are more continuous as a result of the temporal smoothness assumed in the model.

Ultimately in the simulations, the results presented in the epicardial and endocardial geometry by means of the Dynamic model provide a clearer smooth propagation of the electrical wavefront only along the top of the heart surface. A possible reason why these electrical wavefronts do not propagate along the apex of the heart surface could be that these results have been obtained from ECGs of patients with abnormal activations of the heart - Right Bundle Branch Block or Ventricular Tachycardia.

Despite the fact that for several cases in the simulations the detected pacing site matches the area where the heart first activates, the computed numerical distances between the ground-truth and the detected pacing sites over the entire set of cases are extremely large.

Since the reconstructed potential distributions do not follow a normal electrical activation pattern and the algorithms to detect the pacing site are computed over them, these relative errors could be either due to the performance of the detection algorithms or the performance of the regularization methods.

Even so, both the Divergence and the Temporal Derivative algorithms would be compared in performance over all the results per Regularization method used.

Overall comparison of the Relative Error Measure among all the Regularization methods

Broadly, there are three main characteristics that can be observed in the presented tables above:

- The results that have been obtained from interpolated data provide larger numerical errors when detecting the pacing site than the ones resulting from RAW data.
- Based on the results of the Dynamic model per the different geometries: epicardial and endocardial/epicardial, the detecting algorithms perform better when applied to results from the second one.
- The Regularization methods that provide lower numerical errors are the Tikhonov regularization by the use of the Identity matrix and the Dynamic model. Where the algorithm used to detect the pacing sites is the Temporal Derivative using Surface operators, Dtan and Ltan. It is worth noticing that these Regularization methods retrieve the results that present a clearer propagation of the electrical wavefront.

Final Conclusions

The main possible reasons that could have contributed to the obtention of these abnormal results are:

- The data that has been used to reconstruct the potential distributions on the heart has been extracted from patients with cardiac diseases such as RBBB, LBBB or VT. Therefore, the results would be expose to represent activation abnormalities or no electrical activation in certain regions of the heart - given possible scars on the heart tissue.
- Errors on the computation of the source and volumetric models would lead to ill-conditioned geometries of the heart and the torso. If this is the case, then the Hessian, Laplacian and Gradient estimations would also be ill-conditioned since they are computed over the heart mesh. Consequently the use of these estimations as the type of regularization imposed to reconstruct the potential distributions would not be the proper constraint to be regularized.
- The divergence algorithm's performance would be also biased if the geometries are ill-conditioned, given that the divergence is calculated through the Hessian estimation over the heart surface.

- Non-regular geometries composed by non-equally-distributed nodes along the surface would lead to a large triangulation that would provoke the obtention of abrupt and non-smooth potential distributions.
- The Forward matrix is ill-conditioned. By plotting the sensitivity map - i.e. the effect that every node in the torso has in the heart mesh - it has been observed that the weight distribution given by the Forward matrix along the heart mesh is ill-conditioned: the nodes placed on the top of the heart have extremely large weights whereas the nodes placed in the endocardium have absolutely no weight. This could be the reason why the resulting potential distributions obtained by the Dynamic model on the endocardial/epicardial geometry have a very strong propagation of the electrical wavefront along the top of the heart surface.

Bibliography

[1] Leif Sörnmo. Pablo Laguna. Bioelectrical Signal Processing in Cardiac and Neurological Applications. *Department of Electrical Engineering, Lund University Lund, Sweden. July 2005.*

[2] Heart diagram blood flow. *Wikipedia Commons.* https://commons.wikimedia.org

[3] Dr. Robert Droual. Chapter 13. The Cardiac Function. *Modesto Junior College. Pearson Education. http://droualb.faculty.mjc.edu/*

[4] Student Paramedics Blog. http://studentparamedics.tumblr.com/

[5] Rudy, Y. The electrocardiogram and its relationship to excitation of the heart. *Sperelakis, N. (Ed): Physiology and Pathophysiology of the Heart. 3rd edition, Kluwer Academic Publishers Group, chapter 11, pp 201–239, 1995.*

[6] The Electrocardiogram. The Cardiovascular System. *Austin Community College District.* http://www.austincc.edu/

[7] Sarah J. Canyon, Geoffrey P. Dobson. Protection against ventricular arrhythmias and cardiac death using adenosine and lidocaine during regional ischemia in the in vivo rat. *American Journal of Physiology. Heart and Circulatory Physiology. September 2004*

[8] A. van Oosterom. T.F. Oostendorp. Electric Volume Conduction in Bio-medicine. *Laboratory of Medical Physics and Biophysics Catholic University Nijmegen, Nijmegen. The Netherlands. April 2015.*

[9] Messinger-Rapport, B. J. Rudy, Y. Regularization of the inverse problem in electrocardiography: A model study. *Math Biosci 89:79–118, 1988.*

[10] Rudy, Y. Messinger-Rapport, B. J. The inverse solution in electrocardiography: Solutions in terms of epicardial potentials. *CRC Crit Rev Biomed Eng 16:215–268, 1988.*

[11] Gulrajani R. M., Savard P., Roberge F. A. The inverse problem in electrocardiography: Solutions in terms of equivalent sources. *CRC Crit Rev Biomed Eng 16:171–214, 1988.*

[12] Gulrajani, R. M. Models of the electrical activity of the heart and the computer simulation of the electrocardiogram. *CRC Crit Rev Biomed Eng 16:1–66, 1988.*

[13] Gulrajani R. M., Roberge F. A., Mailloux, G. E. The forward problem of electrocardiography. *Macfarlane, P. W. Lawrie, T. D. Veitch (Eds): Comprehensive Electrocardiology. Pergamon Press, Oxford, England, pp 197–236, 1989.*

[14] Gulrajani, R. M., Roberge, F. A., and Savard, P. The inverse problem of electrocardiography. *Macfarlane P. W., Lawrie T. D. Veitch (Eds): Comprehensive Electrocardiology. Pergamon Press, Oxford, England, pp 237–288, 1989.*

[15] Hor´aˇcek, B.M. The forward and inverse problem of electrocardiography. *Ghista, D.N. (Ed): 2nd Gauss Symposium: Medical Mathematics and Physics. Vieweg-Verlag, Wiesbaden,1995.*

[16] Greensite, F. The mathematical basis for imaging cardiac electrical function. *CRC Crit Rev Biomed Eng 22:347–399, 1994.*

[17] Comparison of BEM with FEM. *Copyright 2014. INTEGRATED Engineering Software, Canada.* https://www.integratedsoft.com

[18] Andrew J. PullanLeo K. ChengMartyn P. NashAlireza Ghodrati. Rob MacLeod. Dana Brooks. The Inverse Problem of Electrocardiography. *Bioengineering Institute, The University of Auckland, New Zealand. Cardiovascular Research and Training Institute, University of Utah, Salt Lake City, UT. Department of Electrical and Computer Engineering, Northeastern University, Boston, MA.*

[19] Dana H. Brooks, Robert S. MacLEOd. Electrical Imaging of the Heart. *IEEE SIGNAL PROCESSING MAGAZINE. January 1997.*

[20] Weisstein, Eric W. Identity Matrix. *From MathWorld, A Wolfram.* http://mathworld.wolfram.com/IdentityMatrix.html

[21] Jeff Jauregui. Math 660: Principal curvatures. *Union College, Department of Mathematics. October 2011.* http://www.math.union.edu/

[22] Gradient and Level Surfaces. *Department of Mathematics, Harvard University. Spring 2009.* http://www.math.harvard.edu/

[23] Burak Erem, Member, IEEE, Jaume Coll-Font, Ramon Martinez Orellana, Petr Š tovíček, and Dana H. Brooks, Senior Member, IEEE. Using Transmural Regularization and Dynamic Modeling for Noninvasive Cardiac Potential Imaging of Endocardial Pacing With Imprecise Thoracic Geometry. *IEEE TRANSACTIONS ON MEDICAL IMAGING, VOL. 33, NO. 3, March 2014.*

[24] Glyn A. Holton. Gradient and Gradient-Hessian Approximations. *Value-at-risk (VaR): Theory and Practice. January 2014.*

[25] P.C.Hansen. REGULARIZATION TOOLS. A Matlab Package for Analysis and Solution of Discrete Ill-Posed Problems. *Informatics and Mathematical Modelling Building 321, Technical University of Denmark DK-2800 Lyngby, Denmark. March 2008.* pch@imm.dtu.dk. http://www.imm.dtu.dk/~pch.

[26] Spline Interpolation. *Department of GeoSciences. The University of Edinburgh.* http://www.ed.ac.uk/

[27] SCIRun Software Documentation. *Center for Integrative Biomedical Computing. Scientific Computing and Imaging Institute. University of Utah.* http://www.sci.utah.edu/cibc-software/scirun.html

[28] Singular Value Decomposition (SVD) tutorial. *Massachusetts Institute of Technology.* http://web.mit.edu/

[29] Visualization of Singular Value Decomposition of a Symmetric Matrix. *Mathematics. Stack Exchange.* http://math.stackexchange.com/

[30] P. C. Hansen. The L-curve and its use in the numerical treatment of inverse problems. *Department of Mathematical Modelling, Technical University of Denmark, DK-2800 Lyngby, Denmark.*

[31] Tamara N. Fitzgerald, Dana H. Brooks, Member, IEEE, and John K. Triedman. Identification of Cardiac Rhythm Features by Mathematical Analysis of Vector Fields. *IEEE TRANSACTIONS ON BIOMEDICAL ENGINEERING, VOL. 52, NO. 1, January 2005.*